



Tomas Bata University in Zlín
Faculty of Technology

Doctoral Thesis

**Iron oxide nanoparticles and polymer composites on
thereof for magnetic hyperthermia**

**Nanočástice oxidu železa a kompozitní materiály na jejich bázi pro
magnetickou hypertermii**

Author: **M.Sc. Ilona S. Smolková**

Study programme: P2808 Chemistry and Materials Technology

2808V006 Technology of Macromolecular Substances

Supervisor: Doc. Ing. Natalia E. Kazantseva, Ph.D.

Opponents:

1. Prof. Takeshi Kitano, Ph.D.
2. Ing. Mária Omastová, Dr.Sc.
3. M.Sc. Irina Yu. Sapurina, Ph.D.

Zlín, July 2014

© Ilona S. Smolková

Vydala **Univerzita Tomáše Bati ve Zlíně** v edici **Doctoral Thesis**.

Publikace byla vydána v roce 2014

Klíčová slova: *polymerní kompozity, nanočástice oxidu železa, nanomagnetism, magnetická hypertermie.*

Key words: *polymer composites, iron oxide nanoparticles, nanomagnetism, magnetic hyperthermia.*

ABSTRACT

Magnetic hyperthermia is a progressive method of non-surgical tumour treatment which demonstrated its relevance in *in-vitro* and *in-vivo* studies; however, due to biological constraints on the amplitude ($\leq 15 \text{ kA}\cdot\text{m}^{-1}$) and frequency (100 kHz – 1 MHz) of AC magnetic field, magnetic materials with high value of specific loss power are required for clinical application in order to reach temperatures of 42 – 45 °C. Moreover the problem of uniform distribution and retention of magnetic material in the tumor has to be solved.

The present doctoral thesis deals with preparation of iron oxide nanoparticles and polymer composites on thereof with a complex of magnetic, AC magnetic field energy absorption and rheological properties for the application in magnetic hyperthermia, particularly for the arterial embolization hyperthermia.

Magnetic iron oxide nanoparticles were obtained by coprecipitation method in a controlled growth process leading to the formation of uniform and highly crystalline nanoparticles with repeatable magneto-structural properties. The material obtained represents a mixture of single-phase nanoparticles of magnetite and maghemite with nearly spherical shape. Though the size of nanoparticles corresponds to the single-domain state in the superparamagnetic regime, the material demonstrates ferromagnetic behavior due to strong magnetic interparticle interactions. Nanoparticles were annealed at 300 °C in air in order to ensure the stability of magnetic properties over time. The annealing of the particles does not change their size and shape, but transforms magnetite to maghemite. The dispersion of as-prepared and annealed nanoparticles in viscous glycerol medium shows the high heating rate in alternating magnetic field at moderate field amplitudes, the temperature increases from 37 °C to 45 °C in tens of seconds. The value of specific loss power is of 10 – 30 $\text{W}\cdot\text{g}^{-1}$ depending on nanoparticles concentration and field parameters. The feature of heat output is explained by the combined effect of magnetic interparticle interactions and the properties of the carrier medium. Ferromagnetic behavior of material accounts for the higher energy barrier for magnetization reversal leading to high magnetic losses. At the same time, low specific heat capacity of glycerol intensifies heat transfer in the magnetic dispersion. However, high viscosity of glycerol limits the specific loss power, since the Brown relaxation mechanism of AC magnetic field energy absorption is almost suppressed in this system.

In the current doctoral thesis the problem of magnetic nanoparticles delivery, uniform distribution and retention in the tumor is suggested to be solved by using a bi-functional polymer magnetic composite, combining the embolization ability and high heating efficiency in AC magnetic fields. To this end, maghemite nanoparticles based silicone composite was developed. The initial components of the composite are selected so that the material stays liquid during 20 minutes, providing the opportunity for transcatheter transportation and filling of the tumor vascular system.

After the induction period the viscosity increases rapidly and soft embolus is formed causing the occlusion of the tumour's blood vessels. The radiopaque property of composite required for the monitoring of its deposition is achieved by the addition of potassium iodide. Magnetic nanoparticles uniformly distributed in the composite provide its rapid heating under exposure to the AC magnetic field. The SLP value does not depend on nanoparticles concentration as solely Néel relaxation of magnetization accounts for heat losses in composite. The achieved value of specific loss power belongs to the highest possible for such type of material.

SOUHRN

Magnetická hypertermie je progresivní metoda neinvazivní léčby nádorů, která prokázala svoji užitečnost v *in-vitro* a *in-vivo* studiích; nicméně pro klinické aplikace jsou z důvodu biologických limitů amplitudy ($\leq 15 \text{ kA}\cdot\text{m}^{-1}$) a frekvence (100 kHz – 1 MHz) střídavého magnetického pole vyžadovány magnetické materiály s vysokými hodnotami specifického ztrátového výkonu, aby bylo možno dosáhnout teplot 42 – 45 °C. Pro klinické aplikace je také třeba vyřešit problém rovnoměrné distribuce a udržení magnetického materiálu v nádoru.

Tato disertační práce se zabývá přípravou nanočástic oxidu železa a polymerních kompozitů na jejich bázi, kombinujících magnetické a reologické vlastnosti a schopnost absorpce energie magnetického pole, pro aplikace v magnetické hypertermii, zejména pro arteriálně-embolizační hypertermii.

Magnetické nanočástice oxidu železa byly připraveny metodou koprecipitace za podmínek zajišťujících kontrolovanou nukleaci a růst částic, vedoucích ke vzniku uniformních a vysoce krystalických nanočástic a reprodukovatelnosti magnetostrukturních vlastností. Získaný materiál je směsí jednofázových nanočástic magnetitu a maghemitu s téměř kulovitým tvarem. Přestože rozměr nanočástic odpovídá jedno-doménovému stavu v superparamagnetickém režimu, materiál vykazuje feromagnetické chování vzhledem k silným magnetickým mezičásticovým interakcím. Nanočástice byly žíhány ve vzduchu při 300 °C, aby byla zajištěna stabilita magnetických vlastností v čase. Žíhání nezmění velikost ani tvar částic, způsobuje ale k transformaci magnetitu na maghemit. Disperze takto připravených a žíhaných nanočástic ve viskózním glycerolu vykazuje vysokou rychlost ohřevu ve střídavých magnetických polích při nízkých amplitudách, kdy se teplota zvýší z 37 °C na 45 °C za deset sekund. Hodnota měrného ztrátového výkonu je 10 – 30 $\text{W}\cdot\text{g}^{-1}$. Generování tepla nanočásticemi je způsobeno kombinovaným vlivem magnetických mezičásticových interakcí a vlastnostmi nosného média. Feromagnetické chování materiálu je odpovědné za vysokou energetickou bariéru relaxace magnetického momentu, vedoucí k vysokým energetickým ztrátám. Nízká měrná tepelná kapacita glycerolu současně přispívá k přenosu tepla v magnetické disperzi. Vysoká viskozita glycerolu ale zároveň omezuje měrný ztrátový výkon, protože je zde Brownův relaxační mechanismus pro absorpci střídavé magnetické energie téměř potlačen.

V této práci je navrženo řešení problematiky dopravy magnetických nanočástic do nádoru a jejich rovnoměrné distribuce a udržení v daném místě za pomoci bifunkčního polymerního magnetického kompozitu, kombinujícího schopnost embolizace a vysokou efektivitu ohřevu ve střídavých magnetických polích. Za tímto účelem byl vyvinut kompozit na silikonové bázi, obsahující nanočástice maghemitu. Výchozí složky kompozitu byly zvoleny tak, aby materiál zůstal tekutý po dobu 20 minut, umožňující dopravu a naplnění vaskulárního systému nádoru pomocí katetru. Po indukční periodě rapidně vzroste viskozita a vytvoří se měkký

embolus, který způsobí okluzi nádorových cév. Rentgen-kontrastních vlastností kompozitu požadovaných pro monitoring jeho depozice je dosaženo přidavkem jodidu draselného. Magnetické nanočástice rovnoměrně distribuované v kompozitu způsobují jeho rychlý ohřev při expozici střídavému magnetickému poli. Hodnota měrného ztrátového výkonu nezávisí na koncentraci nanočástic, protože tepelné ztráty v kompozitu jsou způsobeny výhradně Néelovou relaxací magnetického momentu. Dosažené hodnoty měrného ztrátového výkonu tak patří mezi nejvyšší pro daný typ materiálu.

CONTENTS

ABSTRACT.....	3
SOUHRN.....	5
CONTENTS.....	7
ACKNOWLEDGEMENTS	9
CHAPTER 1. STATE OF ART	10
1.1. Micromagnetism and nanoscale magnetism: What is the difference?	10
1.1.1. Micromagnetism	10
1.1.2. Nanoscale magnetism	16
1.2. Magnetic iron oxides.....	21
1.2.1 Crystal structure of magnetic iron oxides	21
1.2.2. Electronic processes in magnetic iron oxides	23
1.2.3. Magnetic properties of bulk iron oxides	24
1.2.4. Magnetic properties of iron oxide nanoparticles	26
1.2.5. Synthesis of iron oxide magnetic nanoparticles.....	26
1.2.6. Application of magnetic iron oxides in medicine	30
1.3. Hyperthermia: a promising approach of cancer treatment	32
1.3.1. Tumor selective effect of hyperthermia	32
1.3.2. Hyperthermia modalities.....	34
1.4. Magnetic hyperthermia.....	41
1.4.1. Mediator delivery methods	41
1.4.2. Requirements for mediator.....	42
1.4.3. Mechanisms of heat generation.....	44
1.4.4. Magnetic materials for thermotherapy	48
1.4.5. Progress in magnetic hyperthermia.....	48
1.5. Arterial embolization hyperthermia	55
AIMS OF WORK	58
CHAPTER 2. METODOLOGY	59
2.1. Synthesis of iron oxide nanoparticles and polymer composites on thereof.....	59
2.1.1.Synthesis of iron oxide nanoparticles by coprecipitation method	59
2.1.2. Synthesis of the magnetic polymer composite.....	60
2.2. Characterization of iron oxide nanoparticles and composites	62
2.2.1. Morphology.....	62
2.2.2. Chemical composition and crystal structure	64
2.2.3. Magnetic properties	71
2.2.4. Heating efficiency	75
2.2.5. Kinetics of polymer crosslinking	77
2.2.6. X-ray contrast measurements.....	77

CHAPTER 3. RESULTS AND DISCUSSION	78
3.1. Preparation of magnetic iron oxide nanoparticles for magnetic hyperthermia	78
3.1.1. Synthesis conditions effect on magneto-structural properties of nanoparticles and heating efficiency in AC magnetic fields.....	79
3.1.2. Influence of synthesis parameters on nucleation and growth of iron oxide nanoparticles in solution.....	86
3.1.3. Effect of post-treatment by annealing of iron oxide nanoparticles on their magneto-structural properties	91
3.1.4. Alternating magnetic field energy absorption in dispersion of iron oxide nanoparticles in viscous medium: Effect of interparticles interactions and properties of carrier medium	100
3.2. Maghemite based silicone composite for arterial embolization hyperthermia	104
3.2.1. Composite formation	105
3.2.2. Rheological study of composite formation: choice of embolic composition	106
3.2.3. Radiopaque property of composite	111
3.2.4. Heating efficiency of composite in AC magnetic field.....	112
CONCLUSIONS	115
FUTURE PROSPECTS	115
AUTHOR’S CURRICULUM VITAE	116
ABBREVIATIONS AND SYMBOLS	120
LIST OF FIGURES	123
LIST OF TABLES	128
REFERENCES	130

ACKNOWLEDGEMENTS

I am eternally grateful to my supervisor Assoc. Prof. Natalia E. Kazantseva. I would like to thank Natalia for her ceaseless encouragement and motivation. Due to her guidance and support this doctoral thesis was prepared. I am also grateful to my consultants Assoc. Prof. Petr Humpolíček and Dr. Robert Moučka for sharing of their experience and professional advises.

I would like to thank Prof. Petr Saha, Rector of Tomas Bata University in Zlin and Assoc. Prof. Vladimír Pavlínek, Director of the Centre of Polymer Systems for providing excellent facilities to perform the research activities.

I am also pleased to express my gratitude to the colleagues from Tomas Bata University in Zlin for their collaboration, especially to Dr. Vladimir Babayan, Dr. Harshida Parmar, Assoc. Prof. Jarmila Vilčáková, Assoc. Prof. Nabanita Saha, Ing. Miroslav Pastorek, Dr. Michal Sedlačík.

I am very thankful to Dr. Oldřich Schneeweiss and Dr. Naděžda Pizúrová from the Institute of Physics of Materials, Academy of Science of the Czech Republic in Brno for the Mössbauer spectroscopy and transmission electron microscopy of prepared samples and for valuable discussions.

I would like to thank Dr. Kira N. Makoveckaya from the Russian Research Centre for Radiology and Surgical Technologies in St. Petersburg, Russia for shearing of her experience in the polymer materials for medical applications and help with the part of composite preparation.

I would like to thank my husband Dr. Petr Smolka not only for his understanding and moral support, but also for help with experiments. Finely, I would like to thank my mother and father and whole my family for their love and support.

CHAPTER 1. STATE OF ART

1.1. Micromagnetism and nanoscale magnetism: What is the difference?

The issues of magnetism are broadly discussed in the literature. The most prominent works by Smit and Wijn [1], Chikazumi [2] and Coey [3] were used as a base for writing of the following section.

1.1.1. Micromagnetism

Magnetic properties of a material are associated with the presence of magnetic moments in some or in all the atoms arising due to the spin and orbital magnetic moments of electrons. These magnetic moments interact not just as a simple dipoles, but exhibit exchange interactions, i.e. a quantum mechanical phenomenon resulting in relative orientation of the spins of two electrons. The exchange interactions depend on the distance between magnetic ions and on their mutual geometrical arrangement and define the magnetic ordering in the material.

Atoms have a non-zero magnetic moment if their d - and f - electron shells are not filled completely. Electron has a charge and a spin with the corresponding magnetic moment (Bohr magneton, $\mu_B = 9.27 \cdot 10^{-24} \text{ J}\cdot\text{T}^{-1}$). Thus for atoms with unfilled d - and f - electron shells the spin and orbital moments of the electrons are not compensated. The magnetic moment in the atom is retained when the atom becomes an ion in the materials crystal structure. The magnetic behaviour of material is defined by the collective interactions between atomic moments and is determined by its response to the external magnetic field. If the material is placed in a magnetic field of strength, \mathbf{H} , then its magnetization (magnetic moment per unit volume), \mathbf{M} , is defined as:

$$\mathbf{M} = \chi \cdot \mathbf{H}, (1)$$

where χ is a magnetic susceptibility. The overall response of material to magnetic field, i.e. magnetic induction is defined as:

$$\mathbf{B} = \mu_0 (\mathbf{H} + \mathbf{M}), (2)$$

where μ_0 is the permeability of vacuum, $\mu_0 = 4\pi \cdot 10^{-7} \text{ H}\cdot\text{m}^{-1}$. By combining equations (1) and (2) one receives:

$$\mathbf{B} = \mu_0 (1 + \chi)\mathbf{H} = \mu_0 \mu\mathbf{H}, (3)$$

$$\mu = (1 + \chi), \quad (4)$$

where μ is magnetic permeability.

Non-magnetic materials, called diamagnets and paramagnets have the magnetic susceptibility values in the range of -10^{-7} to -10^{-5} and $10^{-5} - 10^{-1}$, respectively. Because there are no collective interactions of atomic moments in diamagnets and paramagnets they are not magnetically ordered.

Diamagnetic materials are composed of atoms which do not have the magnetic moments because all orbital shells are filled and there are no unpaired electrons. The magnetization is zero in the absence of an external magnetic field. When exposed to a magnetic field, the negative magnetization is produced due to non-cooperative behaviour of orbital electrons (Figure 1). The magnetic susceptibility for diamagnets is negative and temperature independent. Magnetic permeability, $\mu < 1$. Typical diamagnetic materials are Si, P, Zn, Cu, water, quartz, calcite.

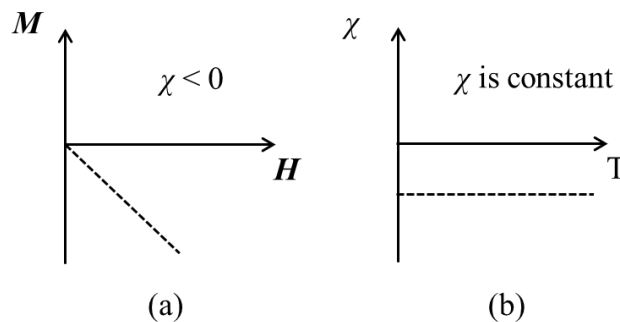


Figure 1. Properties of diamagnetic material: (a) dependence of magnetization on external magnetic field strength, (b) temperature dependence of magnetic susceptibility.

In paramagnetic materials some of the atoms or ions have a magnetic moment due to unpaired electrons in partially filled orbitals. However, these magnetic moments do not interact magnetically and are randomly oriented; as a result the magnetization of material is zero without an external field. When paramagnetic substance is subjected to the magnetic field a partial alignment of atomic magnetic moments in the direction of the field arises resulting in positive magnetization and positive magnetic susceptibility, $\mu > 1$ (Figure 2). The magnetic susceptibility of paramagnetic materials depends on the temperature according to Curie Law (the field aligns the magnetic moments but the elevating temperature randomizes them). The susceptibility is independent of the applied field at normal temperatures and in moderate fields. Iron bearing minerals (montmorillonite, pyrite, siderite, nontronite) are the examples of paramagnetic materials; they owe their properties to the presence of the iron atom with unpaired *d*- electrons. Other examples of paramagnetic substances are Al, Li, Na, K, Ti, O₂.

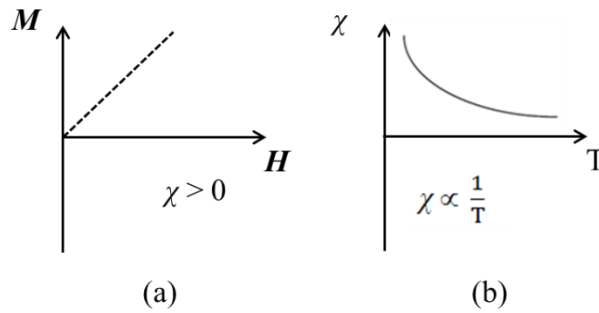


Figure 2. Properties of paramagnetic material: (a) dependence of magnetization on external magnetic field strength, (b) temperature dependence of magnetic susceptibility.

The materials where the long-range magnetic order exists below a critical Curie temperature are called magnetic and are subdivided into three groups: ferromagnets, antiferromagnets and ferrimagnets.

Ferromagnetic materials display very strong interactions between atomic moments produced by electronic exchange forces and resulting in parallel alignment of magnetic moments (Figure 3). Thus ferromagnetic material has a large net magnetization even in the absence of external magnetic field, which is called a spontaneous magnetization. Iron, nickel, cobalt and their alloys are typical ferromagnetic materials. The magnetic susceptibility values for ferromagnets are in the range of $1-10^5$.

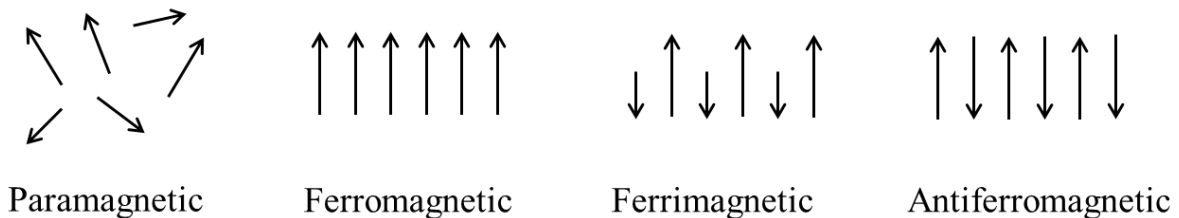


Figure 3. Alignment of individual atomic magnetic moments in different types of materials.

Ferrimagnetic materials have a more complex magnetic ordering due to the features of the crystal structure. In ionic compounds, such as magnetite, two magnetic sublattices exist separated by oxygen atoms. The exchange interaction is mediated by the oxygen anion and is called indirect or superexchange interaction [4]. This strong superexchange interaction results in an antiparallel alignment of the electrons spins between the two sublattices. As the magnetic moments of sublattices are not equal, the resulting net magnetic moment is nonzero (Figure 3).

Despite the fact that the exchange and superexchange interaction are very strong in ferromagnets and ferrimagnets, the thermal energy is able to overcome them and to randomize the magnetic moments. This temperature effect is taking place above a critical temperature, namely Curie temperature (T_C). Above the T_C a ferromagnet /

ferrimagnet is disordered and below it is ordered. At this characteristic temperature magnetic material undergoes transition from ferromagnetic to paramagnetic state, which is second order phase transition.

In antiferromagnetic materials two magnetic sublattices with antiparallel alignment of spins also exist, but the magnetic moments are equal (Figure 3). This results in a zero net magnetization. The magnetic susceptibility above the critical Néel temperature obeys the Curie Law for paramagnets but with a negative intercept indicating the negative exchange interactions. If the spins in the sublattices are not exactly antiparallel, but slightly canted, a small net magnetization arises. This phenomenon is called canted antiferromagnetism and hematite is an example of such type of material.

On the basis of the above description one can expect that ferromagnetic and ferrimagnetic materials have nonzero magnetization in the absence of the external magnetic field. However one more phenomenon of magnetic ordering should be taken into account. This is the dividing of magnetic material into magnetic domains, the areas in which the magnetic ordering is uniform (Figure 4). Usually bulk magnetic material consists of several magnetic domains, each domain has a spontaneous magnetization, but the directions of magnetization are oriented in the way to reduce the total magnetostatic energy and, as a result, the material has a zero magnetization.

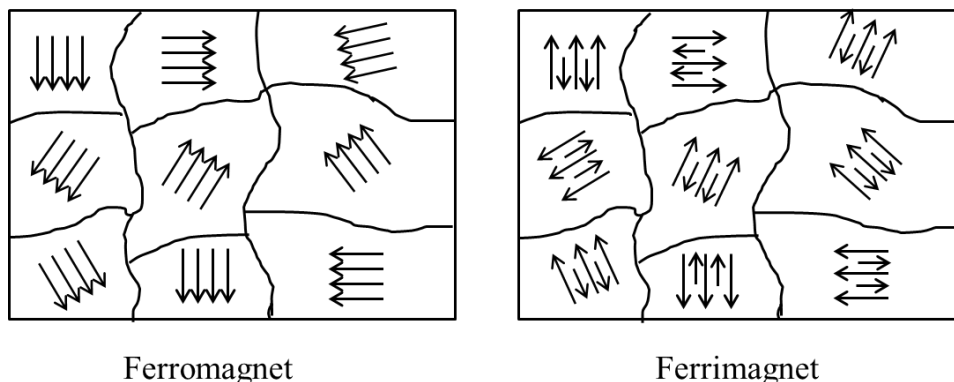


Figure 4. Schematic representation of domain structure in magnetic materials.

When the magnetically ordered material is exposed to the external magnetic field and the field strength is increased gradually the characteristic sigmoidal shape of the $M - H$ dependence is observed (Figure 5).

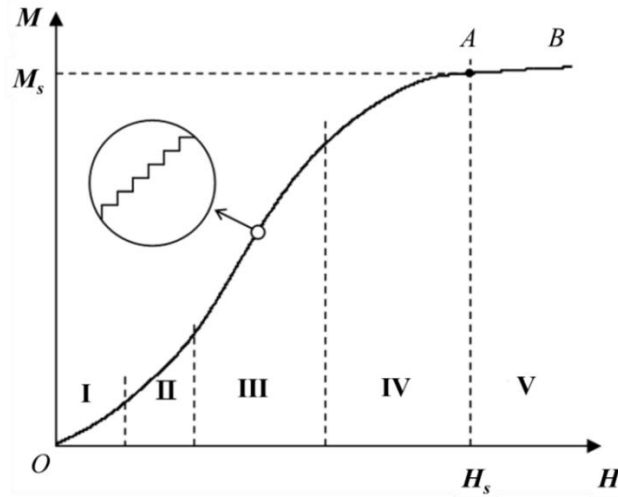


Figure 5. Initial magnetization curve.

When the external magnetic field is applied, the magnetic moments inside the single domains rotate in the direction of the field. The domains with the direction coinciding with the field start to grow and domains with M different from the field direction decrease. A possible lag of the magnetic moment rotation is associated with the presence of the easy and hard magnetic axis. In the direction along the easy magnetic axis, the magnetization of a crystal reaches saturation in a relatively lower magnetic field than in the direction along the hard magnetic axis. This phenomenon is called a magnetic crystalline anisotropy, which is characterized by the magnetic energy necessary to turn the magnetization vector from the easy magnetic axis to the hard magnetic axis. The value of this energy is determined by the magnetic anisotropy constants K_A , which depends on the crystal structure and the chemical composition of a magnetic material.

The curve OAB in figure 5 is called the initial magnetization curve. It is seen that the magnetization depends on the field strength in a complex way. Five different regions can be distinguished on the OAB curve (Figure 5):

- (1) Region I, of initial and reversal magnetization, where $M = \chi_a \cdot H$. Here the processes of domain wall displacement take place and the initial magnetic susceptibility, χ_a , is constant.
- (2) Region II, so called Rayleigh region is characterized by square dependence of M on H . In this region χ shows a linear dependence on H . The magnetization process is realized via domain walls displacement both reversible and irreversible.
- (3) Region III, with the highest susceptibility, χ_{max} , comprises the irreversible domain walls displacement. Magnetization here hops (Barkhausen effect) due to the lags of domain wall displacement when meeting the

inhomogeneities of the materials structure (impurities, microcracks, dislocations, etc.).

- (4) In the region IV the magnetization is approaching to saturation where the rotational processes of magnetic moments take place.
- (5) Region V, when the material is magnetized strongly enough (at saturation field H_s), the magnetization is called saturation magnetization, M_s , and it is uniform all over the whole volume of material (it is also possible to say that material represents one single domain).

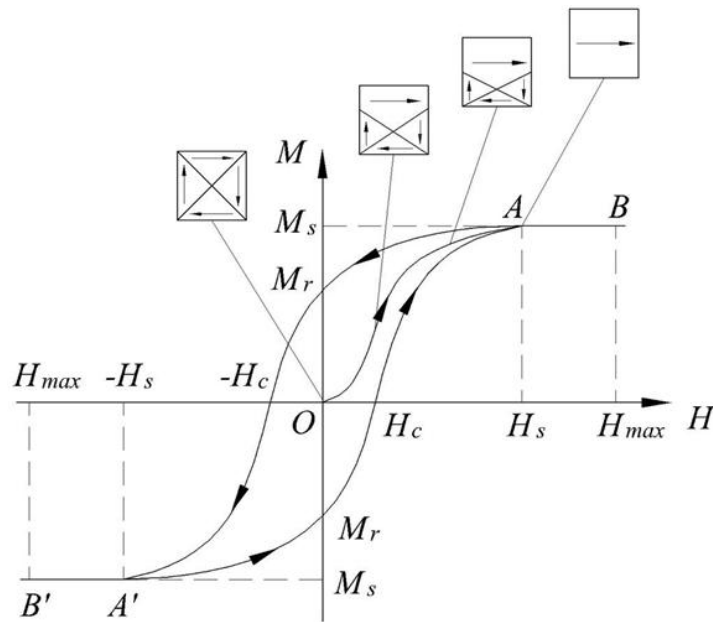


Figure 6. Initial magnetization curve and hysteresis loop for ordered magnetic material. Adapted from [5].

As the field decreases from H_s to zero, the material does not return to the state with $M = 0$, but has a remanent magnetization, M_r (Figure 6). M_r arises because the recovery of domain structure is also accompanied by the domain walls movement, which is hampered by the presence of inhomogeneities. The magnetization vanishes only under a certain opposite field, H_c . The field H_c is called the coercive field, or the coercive force. Under a cyclic variation of the field $H_{\max} \rightarrow 0 \rightarrow (-H_{\max}) \rightarrow 0 \rightarrow H_{\max}$, magnetization follows the closed loop $A \rightarrow M_r \rightarrow A' \rightarrow (-M_r) \rightarrow A$, called the hysteresis loop of magnetization. The area of the magnetic hysteresis loop is proportional to the energy loss in a material during one cycle of field change (hysteresis loss). This energy is spent on heating of a material. Depending on the shape of the hysteresis loop, magnetic materials are classified as magnetically soft (narrow loop) and magnetically hard (broad loop) materials. The shape of the magnetization curve for the bulk magnetic material is determined by the effective magnetic anisotropy, which comprises crystalline anisotropy, discussed above, and

anisotropy of inner and outer demagnetization factors. The anisotropy of inner demagnetization factors is associated with the structural inhomogeneity of the magnetic material. The anisotropy of outer demagnetization factors is associated with the anisotropy of the shape of a sample.

Thus, the basic macroscopic characteristics of a ferromagnet (extrinsic properties) are the parameters of the magnetic hysteresis loop (M_s , M_r , H_c , H_s , area of hysteresis loop, χ_a , χ_{\max}) which, in contrast to the spontaneous magnetization, are structurally sensitive parameters and can be varied in wide limits by thermal, thermomagnetic, mechanical, and other types of processing. The spontaneous magnetization and the Curie temperature are determined by the quantum exchange interactions and are the fundamental characteristics of a magnetic material (intrinsic properties).

If the ferromagnet/ferrimagnet is placed in an alternating (AC) magnetic field other types of losses may be added to hysteresis losses. When the frequency of an AC magnetic field (number of circles of remagnetization per time unit) is high, the lag of magnetic induction over the imposed field arises, leading to the so called lag losses. Additionally eddy current losses arise in conducting materials due to electric currents induced within the material by a AC magnetic field. The hysteresis loop area subsequently increases at high AC magnetic field frequencies. Dynamic magnetization processes will be faced in more details in section 1.4.3.

1.1.2. Nanoscale magnetism

The phenomenon of nanomagnetism comprises the magnetic properties of the objects that have at least one dimension in the nanoscopic range (from 1 to 100 nm). The occurrence of this separate research area of physics is due to the fact that nanoscopic materials possess different magnetic properties compared to the same materials in macroscopic dimensions [6]. This difference arises from the fact that magnetic nanomaterials present:

- (1) Dimensions comparable to characteristic length, such as the limiting size of magnetic domains and exchange interactions lengths.
- (2) Broken translation symmetry, resulting in areas in the crystal structure with reduced coordination number, i.e. with broken bonds and frustrations.
- (3) Higher portion of surface atoms.
- (4) Strong interactions with its neighbourhood. Thus, the properties of nanomaterials are usually derived from the ensembles of nanoobjects.
- (5) The presence of imperfections and defects becomes more relevant resulting in difficulty of reproducibility on properties of nanomaterials.

The main characteristic lengths which define the properties of the magnetic material are the exchange length, l_{ex} , and the domain wall width, δ_0 , defined as:

$$l_{ex} = \sqrt{\frac{2A}{\mu_0 M_S^2}}, \quad (5)$$

$$\delta_0 = \pi \sqrt{\frac{A}{K_A}}, \quad (6)$$

where A is the exchange stiffness constant, K_A is anisotropy constant. The domain wall is a narrow transition region at the boundary between magnetic domains, over which the magnetization changes from its value in one domain to that in the neighbouring domain. The magnitude of l_{ex} and δ_0 usually lies in the range of 1 - 10² nm, thus nano-objects have comparable dimensions.

When the size of a magnetic particle decreases above a critical value, D_{cr}^{SD} , the domain structure is no more profitable in terms of energy; the particle receives a configuration of a single magnetic domain (SD), where all magnetic moments are aligned along the same direction (Figure 7).

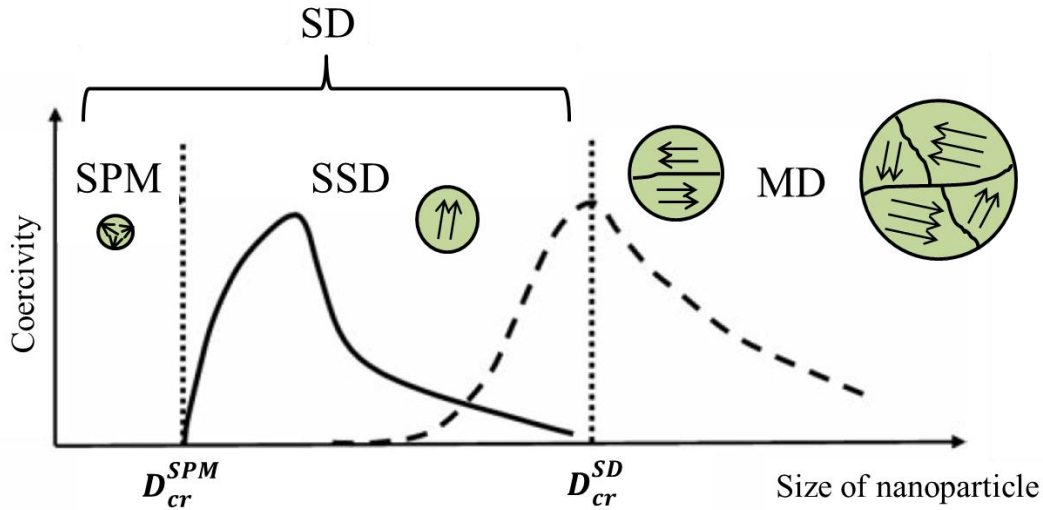


Figure 7. Schematic illustration of the size effect on the magnetic state of material and on its coercivity. Solid curve is coercivity dependence for non-interacting particles. Dashed line is coercivity for particles with coupling between them. Modified from [7].

The critical diameter for the transition from MD to SD configurations depends on the energy balance between the magnetostatic energy and the effective anisotropy energy [8]. SD size is strongly geometry-dependent, and even a small deviation from the spherical shape leads to the increased value of D_{cr}^{SD} [9].

The critical single domain diameter is given by:

$$D_{cr}^{SD} = \frac{72\sqrt{AK_A}}{\mu_0 M_S^2} . (7)$$

Unlike bulk magnetic materials, SD particles may exhibit unstable behaviour of the magnetization due to thermal agitation. The thermal instability of the magnetization occurs if the thermal energy $k_B T$ ($k_B = 1.38 \cdot 10^{-23} \text{ J}\cdot\text{K}^{-1}$ is Boltzmann constant and T is temperature) is sufficient to change the orientation of the magnetic moment of a particle.

Non-interacting SD particles can be either in a stable single domain (SSD) or in a superparamagnetic (SPM) state. In SSD nanoparticles (so called SD particles in ferromagnetic regime) the magnetic moment is pinned along the magnetic anisotropy axis as a result of magnetic anisotropy in nanoparticles. There are several contributions to the total anisotropy energy: (1) magnetocrystalline anisotropy, which is governed by the symmetry of the crystal lattice; (2) shape anisotropy, which is controlled by magnetostatic energy arising from demagnetizing fields; (3) anisotropy of imposed stress (induced magnetic anisotropy); (4) surface anisotropy related to the magnetically frustrated surface layer (5) anisotropy of collective state associated with interparticle magnetic interactions. Therefore, the magnetic moment cannot be reversed by thermal activation without overcoming an energy barrier:

$$\Delta E = K_A V, (8)$$

where K_A is the anisotropy constant that includes all contributions to the anisotropy, V is the particle volume.

When the size of nanoparticle further decreases the energy barrier ΔE also decreases and the thermal energy $k_B T$ is sufficient for randomized rotation of magnetic dipoles inside the particles in a short period of time. Such small particles do not have permanent magnetic moments in the absence of external magnetic field. This phenomenon is called superparamagnetism. For SPM particles the thermal energy is comparable with the magnetocrystalline energy. While the maximum SD size is determined by the energy balance, the SPM threshold depends also on the temperature and on the time scale of the measurement [10]:

$$D_{cr}^{SPM} = \sqrt[3]{\frac{6k_B T_B}{\pi K_A \ln(\frac{t_{meas}}{\tau_0})}}, (9)$$

where T_B is the blocking temperature, τ_0 is 10^{-12} – 10^{-9} s, and t_{meas} is the measurement time.

If the measuring time is greater than time of magnetization relaxation, the nanoparticles are considered to be in SPM regime; if, however, the measuring time is less than relaxation time, the nanoparticles are in a ferromagnetic/ferrimagnetic regime [11].

The atomic magnetic moments in SD particles have preferred orientations, easy axes, representing local energy minima. When SD nanoparticles are exposed to an

external magnetic field, the magnetic moments of the particles are forced to align with the external field. By interaction with an external magnetic field, the magnetization overcomes the energy barrier and changes its orientation within the particle. This decay phenomenon is called the Néel relaxation process with Néel relaxation time [12]:

$$\tau_N = \tau_0 \cdot \exp\left(\frac{K_A V}{k_B T}\right), \quad (10)$$

where τ_0 is pre-exponential factor, i.e. the expression of the anisotropy energy depending on many parameters, including temperature, gyromagnetic ratios, saturation magnetization, anisotropy constants, height of the energy barrier, etc. For sake of simplicity τ_0 is often considered to have values between 10^{-9} s and 10^{-11} s.

From Equation (10) it follows that the Néel relaxation time depends exponentially on the product of magnetic anisotropy constant and particle volume; hence, there exists a definite value of the particle size above which the material exhibits a stable ferromagnetic state.

In a fluid medium, relaxation of magnetic moment is also possible via free rotation of the whole particles, which is called the Brown relaxation. The time constant associated with this mechanism is the Brown relaxation time:

$$\tau_B = \tau_0 \frac{3\eta V_{hydr}}{k_B T}, \quad (11)$$

where η is the viscosity of the carrier fluid, V_{hydr} is the hydrodynamic volume of the particle.

Due to exponential relation in equation (10), the Néel relaxation time increases dramatically with the volume so that for larger particles the magnetization vector is practically blocked, and only the Brown mechanism remains effective (Figure 8) [13]. The relaxation time of this process is proportional to the viscosity of the carrier liquid and, if the particles are inserted into a viscous medium (for example tumour tissue) or fixed (to the cell), the Brown relaxation is suppressed [14, 15].

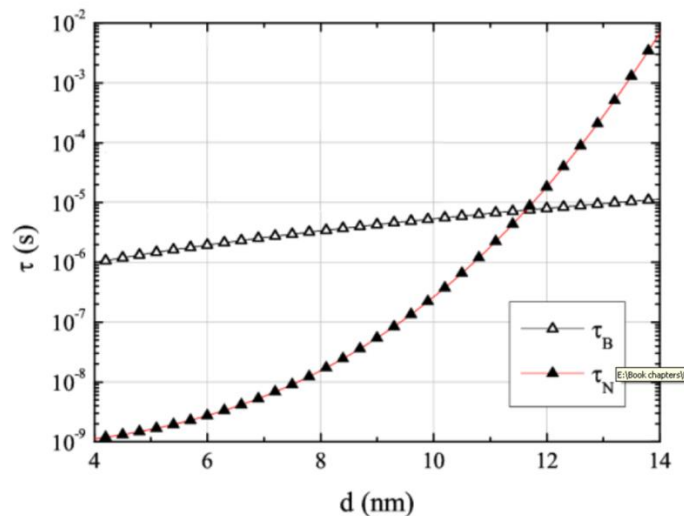


Figure 8. Calculated Néel and Brown relaxation times over a range of particle sizes for a water-based magnetite ferrofluid. Adapted from [13].

For magnetic nanoparticles with broad size distribution both Néel and Brown relaxation take place with an effective relaxation time expressed as:

$$\frac{1}{\tau} = \frac{1}{\tau_N} + \frac{1}{\tau_B}. \quad (12)$$

Figure 9 shows the comparison of magnetization curves for SSD and SPM nanoparticles. The magnetization curve for SSD nanoparticles displays the hysteresis, characteristic for ferromagnets. It is established that the coercivity is the highest for the particle with the diameter between D_{cr}^{SPM} and D_{cr}^{SD} [11].

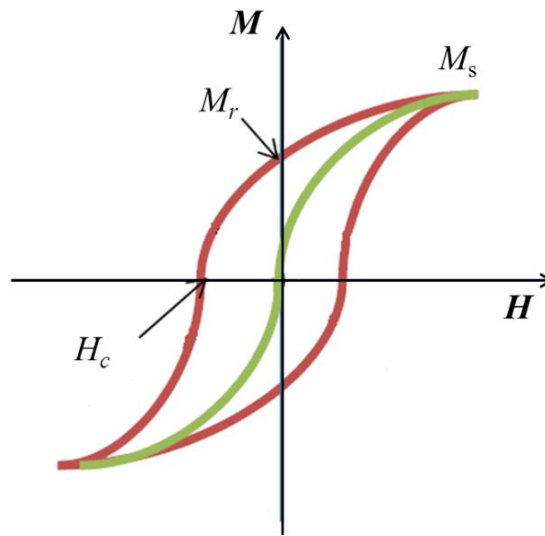


Figure 9. Magnetization curves of SD nanoparticles (red line) and of SPM nanoparticles (green line).

1.2. Magnetic iron oxides

Magnetic iron oxides have long generated technological and industrial interest because of their electrical and magnetic properties, combined with their overall characteristics of hardness, thermal stability and chemical resistance [16]. Nowadays nanomagnetic iron oxide materials are of great interest due to their specific properties linked to the nanometre size of the particles. They found a broad application in catalysis and medicine. They are used for enhancement of Computed Tomography (CT) and Magnetic Resonance Imaging (MRI) contrast, targeted drug delivery, magnetic cell sorting, as well as in a number of applications in cancer therapy, for example in Magnetic Hyperthermia (MH) [17-23]. All of these approaches require defined nanoparticles features together with high magnetization. As an example, small nanoparticles (≤ 10 nm) with short plasma half-lives will favour signal specificity in MRI, but large sizes (below 50 nm) with long plasma half-lives are necessary for accumulation in the tumor region and in MH [18, 19].

In this section the structure and properties of magnetic iron oxides both bulk and nanoscale are considered.

1.2.1. Crystal structure of magnetic iron oxides

Iron oxides consist of arrays of Fe ions and O^{2-} ions. As the anions are much larger than cations (the radius of the O^{2-} ion is 0.14 nm, whereas those of Fe^{3+} and Fe^{2+} are 0.065 and 0.082 nm, respectively), the arrangement of anions governs the crystal structure.

Magnetite

Magnetite has the structure of an inverse spinel with a face-centred cubic unit cell based on 32 O^{2-} ions which are regularly cubic close packed [24]. This unit cell belongs to the $Fd3m$ space group. The unit cell edge, a , has the value of 0.8393 – 0.8396 nm, depending on cation vacancies and impurities. There are eight formula units per unit cell. Iron cations occupy either tetrahedral (site A) or octahedral (site B) sites. Magnetite's unit cell formula can be written as $Fe_8^{3+} [Fe_8^{3+} Fe_8^{2+}] O_{32}^{2-}$ brackets denote the octahedral sites. Trivalent ions occupy both tetrahedral and octahedral sites, and divalent ions only octahedral (Figure 10).

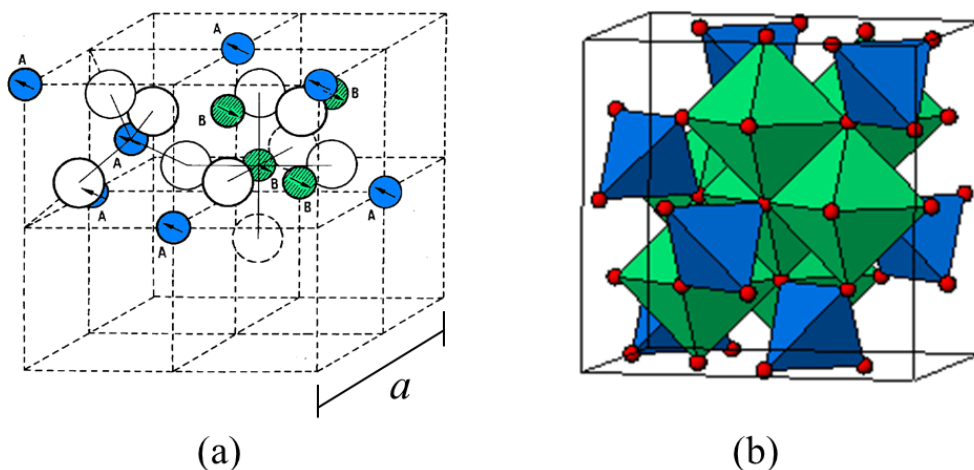


Figure 10. Magnetite crystal structure: (a) Magnetite unit cell. White atoms are oxygen, blue and green represent iron - different colours for tetrahedral and octahedral sites respectively; modified from [25]; (b) Iron polyhedra network (blue tetrahedra and green octahedra) in magnetite unit cell.

In the octahedral layer, the adjacent positions of Fe^{3+} and Fe^{2+} cations enables the electron hopping as a result of the overlap of the d -orbitals between iron atoms. Magnetite is usually non-stoichiometric due to the deficiency of iron cations. In stoichiometric magnetite the ratio of cations is $\text{Fe (II)} / \text{Fe (III)} = 0.5$.

Maghemite

Maghemite, $\gamma - \text{Fe}_2\text{O}_3$ has a structure similar to that of magnetite, but all or most iron ions are trivalent. Maghemite either can have a cubic unit cell with the lattice parameter $a = 0.83474$ nm and the space group $P4_332$, or it can have a stretched tetragonal structure with a space group $P4_12_12$ and unit cell dimensions: $a = 0.8347$ nm and $c = 2.501$ nm.

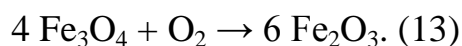
Maghemite unit cell contains 32 O^{2-} ions, $21\frac{1}{3}$ Fe (III) ions and $2\frac{1}{3}$ vacancies. Cations occupy all tetrahedral sites and the octahedral sites are occupied by the remaining cations (randomly distributed) and vacancies. The unit cell formula of maghemite can be written as: $\text{Fe}_8^{3+}[\text{Fe}_8^{3+} \square_{2.67}]\text{O}_{32}^{2-}$, where \square denotes vacancy.

Synthetic maghemite often displays superstructure which arise as a result of cation and vacancy ordering. The extent of vacancy ordering is related to the crystallite size and the nature of precursor and the amount of Fe (III) in the structure. The degree of vacancy ordering decreases with decreasing particle size, with no vacancy ordering in maghemite smaller than about 20 nm.

Oxidation of magnetite into maghemite

In the dry state magnetite is readily oxidized to maghemite by air. Ultrafine crystals of magnetite change to maghemite (over years) even at room temperature

[26]. At temperatures exceeding 300 °C the transformation proceeds further to hematite. Oxidation of magnetite involves a topotactic reaction in which the original crystal morphology is maintained throughout [24]. Initially a mixed phase with less Fe (II), more Fe (III) and more cation vacancies than has magnetite forms, which then further oxidizes. During this process the density of the material falls and the weight of the sample increases because oxygen is taken up:



The reaction proceeds via outward migration of cations towards the surface or crystal together with the creation of cation vacancies and the addition of oxygen atoms. Cations at the surface are oxidized and form a rim of maghemite.

It is now well established that when the size of magnetite crystallites decreases, their sensitivity to oxidation increases [27]. For magnetic iron oxide nanoparticles smaller than 8 nm the composition close to maghemite was reported. For nanoparticles bigger than 12 nm core-shell structure with a core of stoichiometric magnetite surrounded by an oxidized layer was proposed. For intermediate sizes (8–12 nm), the composition was found to be intermediate between those of magnetite and maghemite without a clear core-shell structure.

To take the oxidation process under control, the influence of post-synthesis heat treatment has been studied in a broad temperature range [24, 28]. At 200 – 250 °C crystals smaller than 300 nm transform via the mixed phase to maghemite which it then transforms to hematite at temperature above 500 °C. In small crystals the diffusion pathways are short and reaction rates are fast, so complete oxidation is achieved rapidly. In larger crystals the diffusion pathways are too long and the temperature must be raised above 500 °C to completely transform magnetite to maghemite. At ca. 220 °C the outer layer of initially formed maghemite blocks further conversion at this temperature. At higher temperatures (320 °C) hematite is nucleated in maghemite layer due to arising structural strains. Then a mixed phase of magnetite/maghemite under rim of maghemite forms a mixture of maghemite and hematite. And at temperature above 400 °C a remainder of magnetite transforms to hematite. At 500 °C macroscopic magnetite changes directly to hematite. The reduction of the edge length of cubic unit cell from 0.839 to 0.834 nm at 200 °C indicates the conversion of synthetic magnetite into maghemite.

1.2.2. Electronic processes in magnetic iron oxides

When electrical potential difference is applied to magnetite and maghemite samples they display semiconductor properties [29]. The electrical conductivity in solid material arises due to the motion of free charge carriers. Magnetite has a conductivity of $10^2 - 10^3 \Omega^{-1} \cdot \text{cm}^{-1}$ at 300 K. This high value of conductivity, close to that of metals, is explained by the electron hopping between Fe^{+2} cations (electron configuration $3d^6$), and Fe^{+3} (electron configuration $3d^5$) in octahedral sites. In non-stoichiometric magnetite a small contribution of conductivity via holes (vacancies)

is added. The conductivity of maghemite is mainly determined by the holes (vacancies). At temperature below 125 K, the so called Verwey temperature, the electron hopping between Fe^{2+} and Fe^{3+} ions in magnetite ceases, the electrical resistivity increases abruptly and the crystal structure transforms to a lower symmetry [2]. The ionic arrangement and crystal symmetry at temperature below Verwey temperature are not yet certain.

1.2.3. Magnetic properties of bulk iron oxides

The main type of magnetic interaction between Fe ions in magnetic iron oxides is the electrostatic exchange interactions (superexchange interactions). The exchange reactions proceed via the intervening of the O^{2-} ion. Unpaired $3d$ -electrons of Fe ions interact with electrons on $2p$ -orbitals of the O^{2-} ions (Figure 11), provided that cation and the ligand are close enough to permit coupling of their electrons.

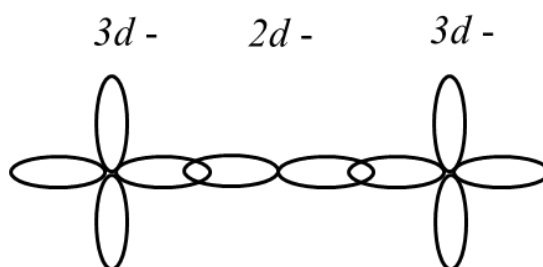


Figure 11. Schematic representation of the overlapping of $\text{Fe}^{2+} / \text{Fe}^{3+}$ cations and O^{2-} anion $3d$ - and $2d$ - orbitals.

The exchange constants depend on the Fe-O bond length and on the bond angle. The main characteristic lengths which define the magnetic properties of iron oxides are listed in table 1. The values are obtained by theoretical calculations for spherical non-interacting particles.

Table 1. Characteristic magnetic lengths for magnetite.

Length	Value reported in [3], nm	Value reported in [6], nm	Value reported in [20], nm
l_{ex}	4.9	-	-
δ_0	73	-	-
D_{cr}^{SD}	38	12	85
D_{cr}^{SPM}	13	4	25

Magnetite

Bulk magnetite is ferrimagnetic at room temperature, and has a Curie temperature of 850 K. The two different cation sites in the structure – tetrahedral occupied by Fe^{3+} and octahedral occupied by Fe^{3+} and Fe^{2+} - form the basis for two interpenetrating magnetic sublattices (Figure 12).

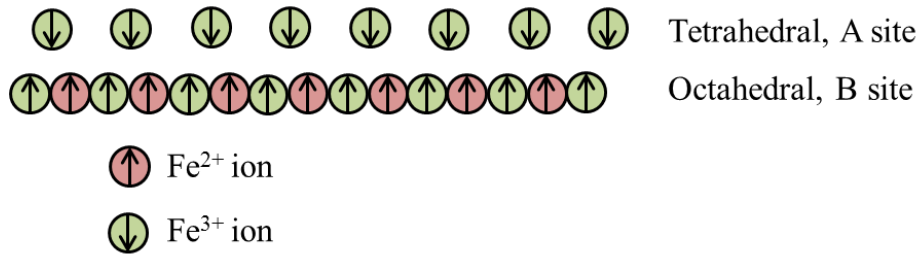


Figure 12. Schematic representation of ferrimagnetic ordering in magnetite.

Below the Curie temperature, the magnetic moments on the tetrahedral and octahedral sites are antiparallel and the magnitudes of the two types of magnetic moments are unequal; this causes ferrimagnetism. The Fe^{3+} ions negate each other, thus the overall magnetization occurs due to Fe^{2+} ions. Bulk magnetite is magnetically soft material, i.e. the magnetization is fully saturated in fields up to 1 kOe for any crystal direction. The saturation magnetization is 92-100 emu·g⁻¹ and coercivity is 200 – 400 Oe depending on the structural characteristics [24].

Maghemite

Bulk maghemite is ferrimagnetic at room temperature. Curie temperature is impossible to measure because maghemite transforms to hematite, $\alpha - \text{Fe}_2\text{O}_3$, at temperature above 800 K. The theoretically estimated Curie temperature is between 820-986 K [24]

The magnetic structure consists of two sublattices: tetrahedral with Fe^{3+} ions are octahedral with Fe^{3+} ions and vacancies (Figure 13).

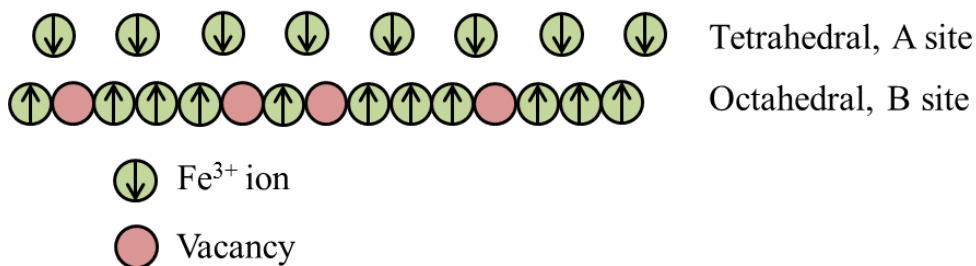


Figure 13. Schematic representation of ferrimagnetic ordering in maghemite.

The atomic moments within each sublattice are parallel, but those of the two sublattices are antiparallel and unequal in magnitude. Maghemite is also magnetically soft material with saturation magnetization is 60 – 82 emu·g⁻¹ [24].

1.2.4. Magnetic properties of iron oxide nanoparticles

With the change of the dimensions from micro- to nanoscale the quantum, electrostatic and magnetic behaviour of the materials dramatically changes. In the bulk magnetite and maghemite the microstructure determines their soft magnetic behaviour. As the length scales approach the size of domain wall width in nanocrystals the lateral confinements such as size and shape and inter-particle exchange effects dominate. Magnetite particles smaller than D_{cr}^{SPM} (see table 1) are SPM at room temperature. The critical diameters of SPM state for maghemite nanoparticles were not estimated theoretically. According to the reported experimental results, maghemite nanoparticles with dimensions less than 10 nm are SPM at room temperature [24]. The M_S value of magnetic iron oxide nanoparticles varies from 30 to 60 emu·g⁻¹, which is lower than for the bulk material. The lower values of M_S for iron oxide nanoparticles are primarily associated with a finite size effect caused by a strong disorder of spins on the surface [24, 30]. The thickness of this surface dead layer was estimated to be 1 nm. Moreover a linear dependence of M_S on particle size was reported [31]. The surface curvature and the disorder in crystal structure are larger for smaller nanoparticles, thus resulting in the reduction of M_S .

Magnetic nanoparticles have tendency to form aggregates due to the magnetic interparticle interactions. Generally, magnetic interactions include both the short-range exchange interaction (under the assumption that the interparticle distance is less than 1 nm) and the long-range anisotropic dipolar interaction. Results on the study of the effect of interparticle interaction on the magnetic properties of a system of nanoparticles are intensively discussed in the literature as they were found to strongly affect the magnetic behaviour of nanoparticles [14, 32]. The issues of interparticle interactions will be faced in section 1.4.3.

1.2.5. Synthesis of iron oxide magnetic nanoparticles

Of great importance is the elaboration of synthetic strategy that will result in the production of nano-sized materials with well-defined and repeatable physical and crystallo-chemical characteristics. Methods of producing iron oxide magnetic nanoparticles can be divided into two broad groups according to the nature of the process triggering the nanoparticles formation: physical methods, which utilize physical processes; and chemical methods, based on chemical transformations.

Physical methods of synthesis of iron oxide magnetic nanoparticles

Physical methods of obtaining iron oxide magnetic nanoparticles such as chemical vapour deposition, laser pyrolysis of organometallic precursors, electron beam lithography, plasmachemical synthesis are elaborated techniques but it is difficult to control the size of the particles and the repeatability of the results is low [33, 34] in nanometre range. The apparatus for such kind of synthesis is usually complicated and needs special skills to operate it.

Biomineralization process of magnetotactic bacteria

Biomineralization process of magnetotactic bacteria is an example of biological synthesis of iron oxide magnetic nanoparticles. These nanoparticles serve as a navigation device for spatial orientation. Bacterial magnetite nanoparticles, magnetosomes, are formed intracellularly by magnetotactic bacteria under very special microaerobic conditions (control of pH, temperature, oxygen content) [35]. The protocol for mass cultivation of magnetotactic bacteria in an automated oxygen-controlled fermenter is established for *Magnetospirillum gryphiswaldense*, *Magnetospirillum magneticum AMB-1* and *Magnetospirillum magnetotacticum MS-1* [36]. A production of 6.3 mg, 3.3 mg and 2.0 mg of magnetite per litre of cell culture per day was found for *Magnetospirillum gryphiswaldense*, *Magnetospirillum magneticum AMB-1* and *Magnetospirillum magnetotacticum MS-1*, respectively. Figure 14 represents the TEM image of *Magnetospirillum magneticum AMB-1*.

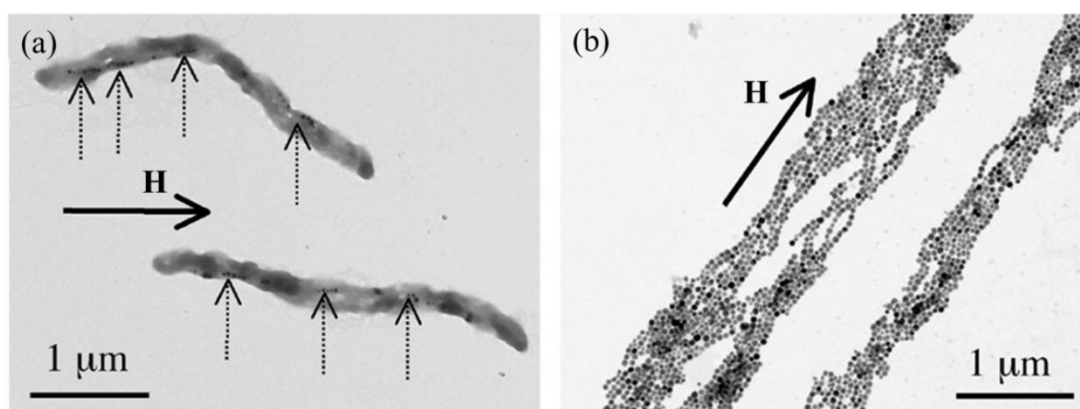


Figure 14. TEM image of (a) whole magnetotactic bacteria *Magnetospirillum magneticum AMB-1*, (b) extracted magnetosomes. The arrow denotes the external magnetic field direction. Adapted from [37].

Inside the bacteria 3 – 4 short chains of iron oxide nanoparticles, magnetosomes are located [37]. The particles in the chain are oriented so that easy magnetic axis are aligned along the chain directions, forming a permanent magnetic dipole. These chains can be separated from the bacteria. Iron oxide nanoparticles inside the magnetosomes are connected by biological membrane, composing from highly

specific and complex subset of proteins. By applying an external magnetic field the chains line up along the field direction inside the bacteria and in the separated magnetosomes (Figure 14). Two types of nanoparticles are observed in magnetosomes – ferromagnetic and SPM. Though magnetosomes possess certain advantages over the chemically synthesized nanoparticles, the application of biomineralization process is not widespread due to complicated synthesis and very low income of iron oxide nanoparticles. Moreover, there are concerns regarding biocompatibility of bacterial protein coating restricting their usage in medicine.

Chemical methods of synthesis of iron oxide magnetic nanoparticles

Obtaining of iron oxide magnetic nanoparticles by chemical reactions is simple, cheap and effective in terms of control over composition, size, shape and size distribution of nanoparticles. The mostly used chemical methods of synthesis of iron oxide nanoparticles can be generally divided in to four groups according to the initial reagents and reaction medium:

Precipitation of iron salts in solution

Solution chemistry offers many possibilities for “chemical manipulation” and allows to synthesize solids of diverse structure, composition and morphology [16]. The control over the synthesis requires a good understanding of the formation process of nanoparticles, i.e. how the ions go from the solution to the solid. This is a complex phenomenon from chemical and structural point of view because it involves a set of chemical reactions and experimental conditions (concentration, acidity, temperature, nature of the anions, etc.) which strongly influence on the properties of obtained nanoparticles. Precipitation is the result of a process of inorganic polycondensation involving the hydrolysis of metal ions in solution and the condensation of hydroxylated complexes. Hydrolysis, condensation and complexation reactions of cations in aqueous solutions are the phenomena involved in the formation of solid by precipitation [16].

To obtain magnetic iron oxide nanoparticles by precipitation of iron salts one can either take iron (II) salt, which is precipitated and further oxidized, or iron (II) and iron (III) salts coprecipitation can be performed [38-42]. Such approaches offer an opportunity to obtain biocompatible iron oxide nanoparticles from aqueous solutions of non-toxic initial reagents at temperatures not exceeding 100 °C. The main disadvantages of this method reported in the literature are the broad particle size distribution, multiphase composition, and poor colloidal stability [40, 42].

The coprecipitation is usually modified by the addition of the surface active substances to the reaction medium during or after the reaction, which cover the surface of nanoparticles providing colloidal stability and possibility to bind other molecules. Among these substances are dextran, carboxymethyldextran, sodium citrate, carboxylic acid functionalized ligands [43-46].

The coprecipitation reaction can be performed not in an aqueous medium, but in a mixture of different polyols, for example diethylene glycol, *N*-methyl-diethanolamine [47]. This method is called polyol process.

Synthesis of nanoparticles from emulsions

This group of methods is based on the principle of precipitation in highly constrained environment. For the synthesis of iron oxide nanoparticles either water-in-oil emulsions [48, 49], or oil-in-water emulsion [50] are utilized. The surfactant molecules form micelles (1–50 nm in diameter) which expose either hydrophilic part of surfactant to a polar solvent, or the hydrophobic part to a non-polar hydrocarbon solvent. The aqueous phase contains soluble iron salt and precipitation agent. These microdrops collide, coalesce, and break again. Conceptually, when microdrops with salts solution meet the microdrops with precipitation agent the solid phase is formed [51]. Particle size can be therefore controlled by varying the solutions concentration and the size of microdrops. The main disadvantage of these methods is the presence of surfactant coating on nanoparticles surface, which can not be easily removed. This surfactant coating reduces the biocompatibility of nanoparticles. Moreover, only small quantities of nanoparticles can be synthesized by this method.

Thermal decomposition of organometallic compounds

In this method organic iron (III) compounds are used as the initial components: iron pentacarbonyl, $\text{Fe}(\text{CO})_5$, in the presence of oleic acid [52-54], iron cupferron, $\text{Fe}(\text{Cup})_3 = \text{Fe}(\text{O}_2\text{N}_2\text{C}_6\text{H}_5)_3$ [55], iron acetylacetonate, $\text{Fe}(\text{acac})_3 = \text{C}_{15}\text{H}_{21}\text{FeO}_6$ [56], iron fatty acid salts (oleate, stearate) [57, 58]. Thermal decomposition of organometallic precursors proceeds in a high-boiling-point solvent and provides aggregation-free, monocrystalline and monodisperse nanoparticles in the size range of 4 - 50 nm [55-57, 59]. The monodispersity of nanoparticles arises due to the separation of the nucleation and growth events. For example the nucleation of iron oxide nanocrystals from iron (III) oleate complex occurs at 200-240 °C while the crystal growth proceeds at about 300 °C [58]. To obtain nanoparticles with sizes above 20 nm the so called seed-mediated growth is utilized. Small nanoparticles are mixed with the precursor material and treated at elevated temperatures. By varying the quantity of seeds it is possible to obtain nanoparticles with different sizes. However, this approach results in a high degree of disorder in crystal structure [60]. Large crystal lattice strains were demonstrated to occur in nanoparticles prepared by this method, which affect their magnetic properties. Furthermore, solvent exchange and purification are required for nanoparticles to be used in physiological media.

1.2.6. Application of magnetic iron oxides in medicine

Iron oxide magnetic nanoparticles have many potential applications in medicine due to their unique physical properties and biocompatibility. The small size of nanoparticles, which is smaller or comparable with the size of cells (10–100 μm), viruses (20–450 nm), proteins (5–50 nm), allows a closer interactions with these entities. A large surface volume is utilized for targeting nanoparticles to cells or to the drug molecules. The magnetic properties of nanoparticles effort the possibility to manipulate with them by the external magnetic field, to enhance the contrast of MRI and to transfer the energy of an external AC magnetic field into heat by means of losses in nanoparticles. Nowadays there are four main concepts of using magnetic iron oxide nanoparticles in medicine: magnetic separation, drug delivery, imaging and hyperthermia treatment [17–20, 22, 23, 61]. Each particular application requires defined properties of nanoparticles and high magnetization. For example, small SPM nanoparticles are preferred for cell labelling, drug delivery and MRI of liver and spleen, while larger SD ferromagnetic nanoparticles are needed for heat treatment of tumor and MRI of tumor.

The separation of cells from their native environment is theoretically possible by attaching the biocompatible iron oxide magnetic nanoparticles to these cells. For the targeting a chemical modification of the particles surface should be done, for example with antibodies, or hormones. Further cells separation is possible by applying a permanent magnet, to which the cells targeted with magnetic nanoparticles cells are attracted. A successful binding to red blood cells [62], lung cancer cells [63], urological cancer cells [64] was reported.

Functionalized iron oxide nanoparticles may serve as the cytotoxic drug carriers allowing to reduce the influence of drugs to healthy cells and to reduce the dosage. Nanoparticles with bonded drug molecules are injected, usually in the form of magnetic liquid, in the blood stream and are concentrated by means of an external magnetic field in the desired site. Then the drug is released by means of changes in physiological conditions, such as pH, temperature or by enzymatic activity [65]. Several *in-vivo* studies on animals model reported successful cytotoxic drug delivery and tumor remission [65–67]. The clinical trials demonstrated that the infusion of ferrofluids was well tolerated by patients, and successfully directed to the advanced sarcomas [68].

The SPM iron oxide magnetic nanoparticles are commonly used for the enhancement of MRI contrast. The contrast agent interacts with the hydrogen nuclei affecting their relaxation time. SPM iron oxide nanocrystals with large magnetic moments, of a few thousand μ_B , create a large heterogeneous magnetic field and dephase the protons magnetic moments. One type of iron oxide nanoparticles for imaging applications has been approved by the Food and Drug Administration agency of the United States and is available on the market. These are SPM nanoparticles “Feridex I.V.” produced by Advanced Magnetics Inc., utilized for the organ-specific targeting of liver lesions and subsequent imaging. An other commonly used MRI contrast agent Resovist[®] from Bayer Schering Pharma AG

consists of magnetite nanoparticles with 5 nm diameter and polydispersity index, $\sigma = 0.4$.

The current work is devoted to the design of the iron oxide magnetic nanoparticles and composites on thereof for application in hyperthermia cancer treatment. Thus the theoretical background, advantages and disadvantages of this method compared to other treatments, important achievements and problems to be overcome will be widely discussed in the following section.

Those diseases which medicine do not cure, the knife cures; those which knife cannot cure, fire cures; and those which fire cannot cure, are to be reckoned wholly incurable.

Hippocrates

1.3. Hyperthermia: a promising approach of cancer treatment

Treatment of malignant carcinomas is one of the most hot-bottom problems of the clinical medicine. Oncological diseases are on the second place after cardiovascular pathology [69]. In the most cases the only method providing long term survival rates of patients with tumours of different localization is the surgical operation. However by the moment of diagnostics of cancer the surgical removal of the tumor is possible only for 5-15 % of patients and the other 85-95 % should have only palliative cure by systemic chemo- and radio-therapy. Although these treatments have demonstrated encouraging response rates, symptom palliation and occasional down staging of tumours, their impact on survival is minor. Therefore, the enhancement of the existing non-invasive methods and the elaboration of new effective methods of cancer treatment are of high importance.

The use of increased temperatures in cancer treatment existed for many centuries. The oldest report was found in the Egyptian Edwin Smith surgical papyrus, dated around 3000 BC. Romans, Greeks, Indian physicians applied local and whole body heating. As a source of heat they used poultice of cotton wool, heated stones and vapour. In 1868 germane physician W. Bush concluded that fever induced by certain bacteria can cause tumor regression or cure cancer [70]. An American surgeon Coley also observed the same effect. He prepared a vaccine for injection at the tumor site containing streptococci, which is known as “Coley’s toxin” [71]. This toxin induced a fever (about 39 – 40 °C) and those patients who had the highest fever had the longest survival. Later the method of cancer treatment by elevated temperatures received a name “hyperthermia”.

A worldwide interest in hyperthermia was initiated by the first international congress on hyperthermic oncology in Washington in 1975 followed by a growing enthusiasm in this research area [72]. However some clinical results of randomized studies were disappointing, indicating the necessity in the improvement of heating techniques. Nowadays, the rationale for using hyperthermia in cancer therapy is well established. Hyperthermia being a physical treatment results in fewer side effects than chemo- or radio-therapy.

1.3.1. Tumor selective effect of hyperthermia

According to National Institute of Health, USA, Hyperthermia is defined as a type of cancer treatment in which body tissue is exposed to high temperatures (up to

41 °C), to damage and to kill cancer cells, and/or to make them more sensitive to the effects of radiation and cytotoxic drugs. However in the contemporary literature the temperature interval of 40 – 45 °C, in which the hyperthermic effects appears (cancer cells are damaged, while normal cells remain unaffected) is reported. A selective tumor cell killing effect of hyperthermia is related to a characteristic difference between normal and tumor physiology [72]. Generally it is considered that the growth of the blood vessel in the tumor cannot follow the tumor growth. Thus, the tumor becomes a no-developed. Indeed, the architecture of the vasculature in the solid tumours is chaotic, resulting in regions with hypoxia and low pH (acidic, due to anaerobic glycolysis), which is not found in normal tissues. In this condition hyperthermia sensitivity of tumor tissue is high. Meanwhile, most normal tissues stay undamaged after 1 hour treatment at temperatures of up to 44 °C.

If we consider the hyperthermic effect on the cell level it should be noted that there is no difference in hyperthermia sensitivity between a normal cell and cancer cell in every phase of cell growth [73]. The cell circle includes the mitotic phase (*M – phase*) during which the cell division proceeds and the interphase (*I – phase*) during which the cell prepares for division (Figure 15) [74]. There are so called checkpoints in *I – phase*, at which special proteins control the condition of the cell and if the damages are detected the cell repairs them, or starts the apoptosis, the process of programmed cell death. Therefore during the *I - phase* hyperthermia sensitivity is the highest, compared to a period of cell division, mitotic phase, *M – phase* [75]. When the normal cell reaches the fixed size the cell breeding stops, while cancer cell growth does not stop, i.e. the cell cycle repeats indefinitely. Accordingly, hyperthermia is considered to affect preferentially on cancer cells.

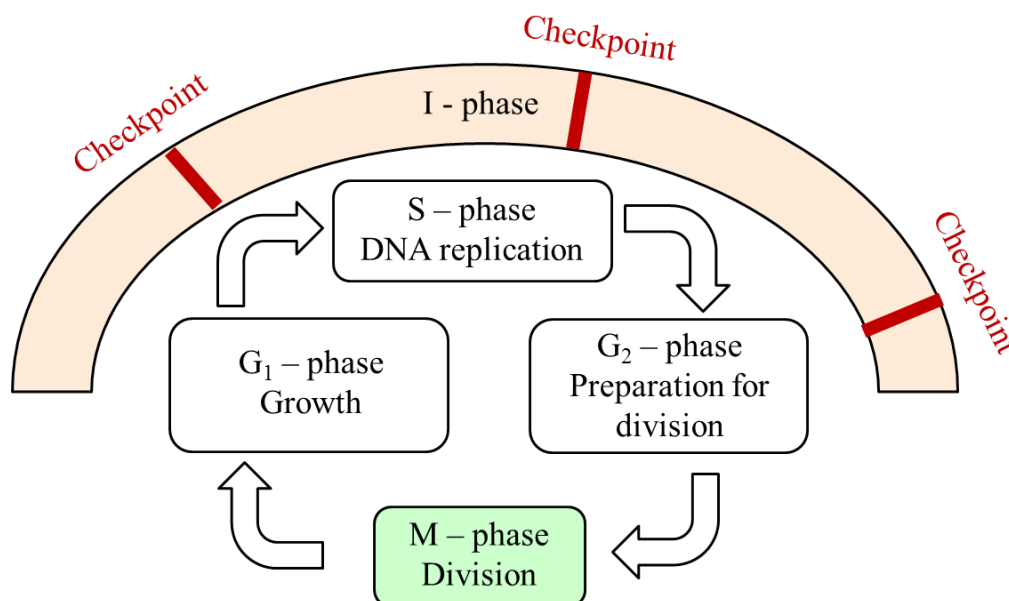


Figure 15. Cell cycle of a normal mammalian cell.

In spite of the large number of the reports on the cytotoxic effect of hyperthermia on the cancer cells the mechanisms of heat cytotoxicity on the cellular level are not well understood. It seems that the cytotoxicity is related to several phenomena, triggered by heat [75, 76]:

- (1) Deterioration of DNA synthesis and repair mechanism;
- (2) Inhibition of cell respiration;
- (3) Alteration in cytoskeleton and cell membranes;
- (4) Increase of the flux of cytotoxic oxygen free radicals.

Depending on the applied temperature, there are two possible mechanisms of cell death. Hyperthermic temperatures (40 – 45 °C) cause apoptosis, the process of programmed cell death. Temperatures above 45 °C result in thermal ablation and tumor necrosis. The advantage of hyperthermia over thermal ablation is that it triggers the progressive cell death with natural origin, while thermal ablation causes rapid cell death and necrosis of the tumor, as a result a large amount of cell decomposition products cause the systemic toxicity.

For the evaluation of treatment efficacy in clinical practice the complete response rate is usually used, it refers to the number of people (in percent), whose tumours responded to the treatment (shrieked or disappeared). The response rates varying from 0% to 40% (overall 13%) were reported on the use of hyperthermia alone, which is close to the response rates of chemo- and radio- therapy [72]. When hyperthermia was used in combination with radio-therapy or chemotherapy the response rates increased for tens of percent. In some patient groups, a substantial gain in overall survival was found.

Nowadays the experimental clinical studies of hyperthermia are performed all over the world, and it is well established that clinical outcome very much depends on the heating technique used.

1.3.2. Hyperthermia modalities

Three methods of hyperthermia treatment can be distinguished according to the focusing of heat: whole body hyperthermia, regional hyperthermia, and local hyperthermia.

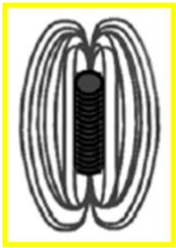
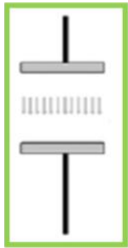

In the whole body hyperthermia the energy is introduced into the whole body. The heating is performed by placing the patient into hot water, air, wax; water perfused blankets or suites can be applied, or the patient is heated by radiofrequency exposure in an insulated chamber [77]. The temperature increase is usually limited to 41,8 – 42 °C because raising the body temperature above 42.5 °C causes coma and near death [78]. Whole body hyperthermia can be advantageous over regional or local hyperthermia for patients with widespread disease and micrometastases [77]. However, it is limited by the significant risk of fatal side-effects, i.e. death due to liver necrosis, severe vomiting, cardiovascular stress, etc.

Regional hyperthermia is applied by perfusion of a limb, organ or body cavity with heated fluids containing cytotoxic drugs [72, 77]. The temperature can be increased to 43 – 44 °C for duration of 2 – 4 hours. This type of treatment is costly and demanding and has a high risk of serious complications and death.

The aim of local hyperthermia is to increase mainly the tumor temperature [72]. Local hyperthermia can be applied by external or interstitial methods. The energy distribution in the tissue strongly depends on its thermal characteristics, inhomogeneous and blood flow. The reduced blood flow in the tumor tissue, compared with that in normal tissue is advantageous, since tumor tissue will heat more easily.

The device generating the energy for heating in medicine in form of electromagnetic waves with radio frequency (RF) is called applicator. According to the heating principle one can distinguish: dielectric and inductive hyperthermia and according to the type of the applied AC field (magnetic, electric or electromagnetic) the inductive, capacitive or microwave modalities are subdivided (Table 2).

Table 2. Classification of hyperthermia modalities according to heating principle and applied AC field.

Heating principle	Inductive	Dielectric	
Hyperthermia modality	Inductive	Capacitive	Microwave
Employed AC field	Magnetic	Electric	Electromagnetic
	50 kHz -1MHz	5 - 45 MHz	60-2400 MHz
			

Evaluation of heating efficiency

The rate at which the energy is absorbed by the human body when exposed to a RF electromagnetic field is characterized by specific absorption rate (SAR). This value is commonly used to measure power absorbed from mobile phones and during MRI scans. SAR is defined as the amount of energy absorbed in tissue during exposure to an electromagnetic radiation [73]:

$$SAR = \left(\frac{d}{dt} \right) \left(\frac{dW_{ab}}{dm} \right), \quad (14)$$

where W_{ab} is absorbed energy, m is mass of the tissue, t is time.

The rate of tissue temperature change when exposed to AC electromagnetic field is related to SAR as:

$$\frac{dT}{dt} = \frac{SAR + P_m - P_c - P_b}{C \cdot m}, \quad (15)$$

where T is tissue temperature, P_m is the metabolic heating rate, P_c is the rate of heat loss per unit volume due to thermal conduction, P_b is the rate of heat loss per unit volume due to the blood flow and C is the heat capacity of tissue. If a body is in a steady-state condition before the exposure, then:

$$P_m = P_c + P_b; \quad (16)$$

and during the initial period of exposure:

$$\frac{dT}{dt} = \frac{SAR}{C \cdot m}. \quad (17)$$

Thus, SAR can be determined from the calorimetric measurements of tissue temperature increase in time right after the beginning of the exposure. SAR is measured in Watts per kilogram of tissue ($W \cdot kg^{-1}$). In practice it is a challenging task to induce and sustain temperatures above the systemic temperature ($37^\circ C$) in a defined volume as the blood flow counteracts the temperature rise.

Dielectric heating

Dielectric heating is a type of heating generated in dielectric materials exposed to an AC electric field [73]. This phenomenon is related to the polarization in the dielectric material. In an electrostatic field the electrons in atoms are slightly shifted in the directions opposite to the electric field, E (Figure 16).

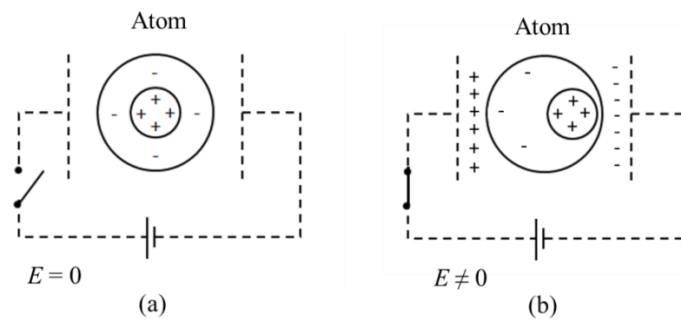


Figure 16. Polarization of atom: (a) atom in the absence of electric field; (b) formation of electric dipole in non-zero electric field.

Consequently, the atom forms a kind of electric dipole in external electrostatic field. For some substances (HCl, H₂O) the electric dipole is naturally formed without applying an electrostatic field. These molecules are called polar. In the case of a liquid including a permanent dipole, for example water, which is suddenly put in an electrostatic field the permanent dipole begins to move in the electric field direction. However this movement is interrupted by an intermolecular binding force and resists the thermal motion. In this case there is a time delay associated with the motion of the permanent dipole toward the electric field direction. If the electrostatic field is shut off it takes some time (relaxation time) until the polarization returns to zero.

Dielectric heating applicator that is driven by RF wave is called capacitive applicator. The frequency range used in this type of applicator is 5 – 45 MHz. The AC electric field is applied through a pair of electrodes placed on the opposite sides of the body (Figure 17 a). Based on electric fields produced between the parallel-opposed electrodes the heating can be performed locally or regionally. An example of commonly employed dielectric heating system is the Thermotron RF-8 (Yammamoto Vinyter Co. Ltd., Osaka, Japan), which is widely used in Japan (Figure 17 b).

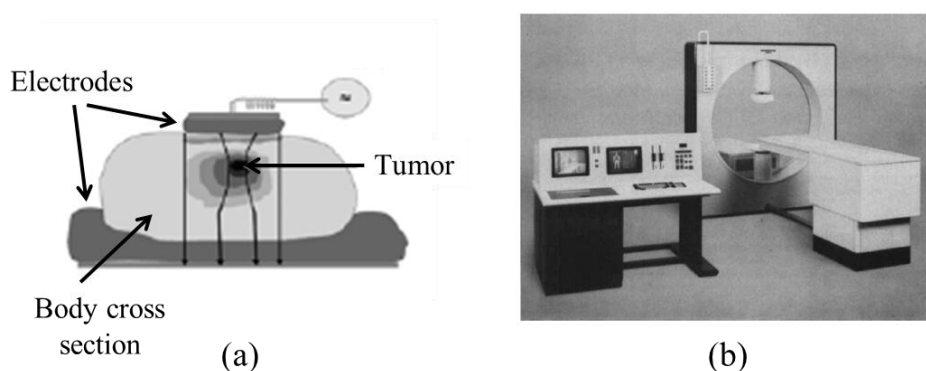


Figure 17. Capacitive applicator: (a) schematic representation; (b) Thermotron RF-8. Adapted from [76].

The major limiting factor for dielectric heating is that this method is non-tissue specific and causes heating in all the tissues into which the AC electrical field penetrates, i.e. prolonged elevation of tumor tissue temperature above 42°C can result in uncontrollable and destructive hot spots in healthy tissues. Moreover, an excessive heating of subcutaneous fat or head skull is noticed because an electric field becomes perpendicular to these high-impedance layers of human body.

To reduce the incidence of skin and fat burns the electrodes are coupled to the body surface by cooled (5 – 10 °C) water bags. Capacitive hyperthermia is usually combined with radiotherapy or chemotherapy due to the disappointing response rates obtained from hyperthermia alone [77].

The dielectric heating principle is utilized also in microwave hyperthermia in applicators operating at super-high-frequency or microwave frequency range (60 – 2400 MHz). These applicators are called antennas.

Microwaves heat the intracellular water molecules by dielectric loss effects [73]. Most of the tissues comprise water molecules which represent permanent dipoles. In the microwave band, the permanent dipole cannot follow the quick fluctuation of a high-frequency electric field and large dielectric loss arises generating heat. Generally, the higher the microwave frequency the better the ability to localize the deposition of electromagnetic energy, but this occurs at the cost of lower tissue penetration.

The system for microwave heating usually consists of several antennas surrounding the patient (Figure 18). Each antenna can generate radiation independently and of differing strength thus allowing better control of the field and high level of treatment tailoring.

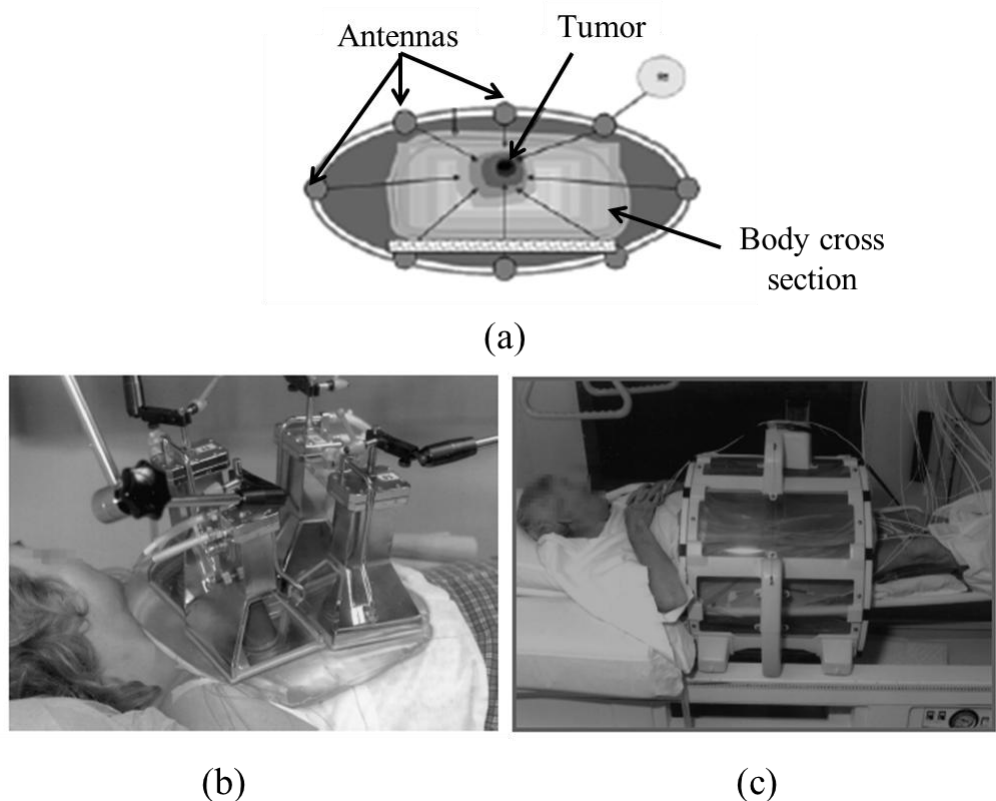


Figure 18. Microwave applicator: (a) schematic representation; (b) custom-built Lucite Cone waveguide applicator; (c) commercially available BSD – 2000 system (BSD Medical Corporation, Salt Lake City, Utah). Adapted from [72, 76].

Microwave hyperthermia appears to offer no advantage over capacitive hyperthermia. Although microwave heating is safe, it has few side effects and has produced some encouraging response rates, the technique is greatly limited by its poor tissue penetration and poor tumor targeting. These limitations suggest that microwave hyperthermia better suits to the treatment of small superficial tumours.

Inductive heating

Inductive heating utilizes an AC magnetic field with frequencies in the range of 0.005 – 1 MHz (Figure 19). It is based on Joule’s heat arising when eddy currents flow in a resistor. When the coil is wound around the cylindrical conductor and an AC magnetic flux is applied an electromotive force is produced and the current flows in the vortex state.

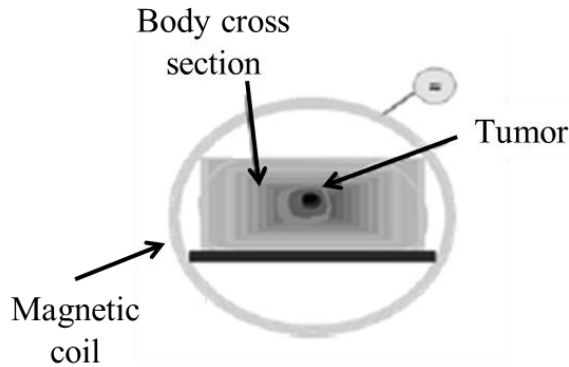


Figure 19. Schematic representation of inductive heating applicator. Adapted from [76].

Inductive heating has the advantage of being able to heat a human body without generating a hot spot in the fat layers as they are of high insulation. Moreover, biomembranes composed of lipids and proteins with high insulation or high impedance are also transparent for the magnetic field. Therefore, the eddy current is generated on the inside of the insulation material if conductive tissues there exist.

Localization of inductive heating is possible due to the difference in distribution of absorbed electromagnetic energy in normal and tumor tissues with different electrical conductivity. Recent *in-vivo* study of electrical conductivity of normal and tumor tissues at different frequencies of AC magnetic field proved that tumor (rat colon cancer cell line) has higher conductivity than normal liver tissue at all measured frequencies [79] (Table 3).

Table 3. Comparison of normal tissue and tumor conductivity at different frequencies of AC magnetic field.

Frequency of AC magnetic field	Conductivity, $\text{mS}\cdot\text{cm}^{-1}$	
	Normal tissue	Tumor tissue
10 Hz	1.26 ± 0.15	2.69 ± 0.91
1 MHz	4.61 ± 0.42	5.23 ± 0.82

The higher conductivity of tumor apparently results from the inner regions of necrosis. As the cell membranes are composed of lipids, which serve as capacitors between intra- and extracellular electrolyte, thus when the cells die by the

mechanism of necrosis, eventual rupture of the cell membrane occurs and the impedance between intra- and extracellular space for these cells decreases, since the membrane loses its insulating property. Therefore, an increase in conductivity in tissues with necrosis is expected. However, the differences in conductivities of healthy and tumour tissues are insufficient for selective heating by AC magnetic field. To achieve deep and proper focusing of the field energy the method based on the heating of magnetic materials incorporated into the tumor tissue under AC magnetic field was proposed.

According to [80], since 2000 the first prototype of an inductive heating system for clinical therapy was set up at the Charité Medical School, Campus Virchow Klinikum, Clinic of Radiation Oncology in Berlin. The applicator consists of a ferrite-core with an adjustable vertical aperture of 30 – 45 cm, generating an AC magnetic field of 100 kHz frequency and adjustable amplitude up to $15 \text{ kA}\cdot\text{m}^{-1}$. A sketch of the system is represented in figure 20.



Figure 20. Sketch of the first prototype of inductive heating system (MFH Hyperthermie systeme GmbH, Berlin, Germany). Adapted from [80].

In this system in order to localize the inductive heating and to increase the efficiency a special magnetic material is embedded into the tumor. Magnetic materials generating heat under exposure to an AC magnetic field is utilized in magnetic hyperthermia, as will be discussed in the next section.

1.4. Magnetic hyperthermia

Magnetic hyperthermia (MH) is the experimental modality of local hyperthermia treatment, it involves the incorporation of a magnetic material, so called mediator, directly into the tumor tissue followed by exposure to an AC magnetic field of sufficient strength and frequency to cause the mediators heating. For this purpose the patient is placed into the coil where an AC magnetic field is generated. The field penetrates skin and fat layers without causing undesired heat in healthy tissues and only the mediator inside the tumor absorbs the energy of the field and transfers it into heat. Thus it is possible to achieve high temperature, to localize the heating in the tumor, to reduce the treatment time, and to minimize the side-effects. Among all hyperthermia modalities MH has the best potential to selectively target the tumor.

The concept of MH was first described by Gilchrist et al. in 1957 [81]. They demonstrated in *in-vivo* experiments the lymphatic uptake of microscopic (20-100 nm) maghemite particles and the temperature increase of about 4.5 °C per minute after applying the AC magnetic field of 1.2 MHz frequency and amplitude of 200 – 240 Oe. Since 1960s there have been a numerous publications describing a variety of experiments with different magnetic materials, different applied fields and different methods of mediator delivery.

In order to eliminate the negative effects of the AC magnetic field in form of eddy currents which may cause pain and damage in the body, the frequency and the amplitude of the field should be sufficiently low. According to the induction law the heating power is proportional to the square of $(H \cdot f \cdot D)$, where H is the AC magnetic field amplitude, f is the frequency and D is the induced current loop diameter. In experimental investigations on volunteers Brezovich et al. found that test persons were able to “withstand the treatment for more than one hour without major discomfort” if $H \cdot f = 4,85 \times 10^8 \text{ (A} \cdot \text{m}^{-1} \cdot \text{s}^{-1})$ for a loop diameter of about 30 cm [82]. For a smaller diameter of the exposed body region and in dependence on the seriousness of the illness this critical product may be exceeded. Currently accepted limits for the AC magnetic field in MH are the following: frequency, $0.05 \leq f \leq 1.5 \text{ MHz}$; and amplitude, $H \leq 15 \text{ kA} \cdot \text{m}^{-1}$.

Nowadays, the MH developed into several pathways according to the method of mediator delivery to the tumor.

1.4.1. Mediator delivery methods

The magnetic mediator, usually in the form of magnetic fluid (magnetic fluid hyperthermia) or composite material, consisting of magnetic nanoparticles is deposited within or adjacent to the tumor in one of four ways [21, 83]:

- (1) Arterial injection: the fluid carrying the magnetic particles is injected in the arterial supply of the tumor. This fluid may be able to form gels entrapping magnetic particles *in-situ* [84], often causing the stop of the

tumor blood supply. The modality of treatment of hepatic malignancies based on this conception is called arterial embolization hyperthermia (AEH).

- (2) Direct injection: the magnetic fluid is injected directly into the tumor. The particles will be located in the tumor tissue and the most of them in the interstitial space and a minor part in blood vessels or intracellularly [80]. Tumor specific antibodies targeted to the nanoparticles surface will favour the enhancement of nanoparticles retention in the tumor.
- (3) Surgical implantation: ferromagnetic seeds are implanted during the surgery into the tumor in interstitial implant hyperthermia. The size of the seeds is of the order of a few millimetres and different alloys are utilized to set the desired Curie temperature to prevent the overheating and reduce the need of invasive thermometry. Interstitial implant hyperthermia is applied for the treatment of brain tumours [85].
- (4) Active targeting: nanoparticles are either targeted by a tumor specific antibodies (antibody targeting) providing a selective binding to the tumor cells [86], or the particles enrichment in the tumor region is achieved by an external magnetic field gradient (magnetic targeting). Up to now, both described methods of active targeting are not able to provide a sufficiently high absorber concentration in the tumor for hyperthermia. The efficiency of delivery has to be increased.

1.4.2. Requirements for mediator

Generally, two classes of magnetic materials are suggested for the MH: magnetic fluids and polymer / gel magnetic composites. Magnetic fluids are heterogeneous systems consisting of stabilized colloidal nano-sized magnetic particles dispersed in dielectric liquid. Polymer magnetic composites consist of low-viscosity media (liquid silicone, polysaccharides, lipiodol, agar etc.) filled with nanoparticles.

Mediator for MH should fulfil a number of requirements:

- (1) Biocompatibility
- (2) Possibility to be delivered to the tumor
- (3) Homogeneous distribution of magnetic phase in the tumor
- (4) Long enough retention in the tumor
- (5) High heating rate

The issue of biocompatibility is usually solved by coating of magnetic nanoparticles by biocompatible coatings (dextran, polyethyleneglycol, polyvinylalcohol, aminosilane, citric acid) and distributing them in biocompatible

liquids (saline, lipiodol) or polymer matrixes (silicone, polyurethane, polyvinyl alcohol, polysaccharides, etc.).

The necessity of selective tumor delivery requires additional properties of mediator, which are defined by the delivery method. For example for the direct intra-arterial injection of the mediator, it should be viscous enough to flow through catheter. In the case of AEH, where the mediator also serves as the embolization material, its viscosity should stay low for the time needed for administration to the desired blood vessel and rapidly increase after a defined time providing effective embolization.

The retention of the magnetic mediator in the tumor tissue can be accomplished by either antibody targeting, application of an external magnetic field or embolization of tumour vascular system.

The heating efficiency of mediator is characterized by the specific loss powder (SLP). SLP is defined as the rate at which the electromagnetic energy is dissipated by a unit mass of a magnetic material [17] and can be experimentally determined by [44, 83, 87]:

$$SLP = \frac{1}{m} \frac{dT}{dt} \cdot C, \quad (18)$$

where C is the heat capacity of mediator, m is the mass of the magnetic component in mediator. SLP is measured in Watts per gram of magnetic material ($\text{W}\cdot\text{g}^{-1}$), or Watts per gram of magnetic elements in the material, for example ($\text{W}\cdot\text{g}_{\text{Fe}}^{-1}$). SLP is sometimes also denoted as specific heating power (SHP). According to Rosensweig [88], the magnetization of non-interacting SD particles linearly responds to the magnetic field (Linear response theory). Thus, the SLP can be expressed in terms of the imaginary part of magnetic susceptibility, χ'' , of nanoparticles, frequency, H , and amplitude, f , of AC magnetic field:

$$SLP = \pi\mu_0\chi''f\frac{H^2}{\rho}, \quad (19)$$

where $\chi'' = (\mu'' - 1)$, μ'' is the imaginary part of the complex permeability or magnetic losses, and ρ is the mass density of the magnetic material. However the experimental results showed the linear response theory may be inadequate for real systems of nanoparticles [89] mainly due to the interparticle interactions. Unfortunately, up today there is no satisfactory model describing the behaviour of magnetic nanoparticles systems in AC magnetic field.

However, in any case the SLP strongly depends and can be controlled by both the AC magnetic field parameters and the magnetic properties of materials, precisely by the magnetic loss value. As there are very strict limits on the frequency ($0.05 \leq f \leq 1.5$ MHz) and the amplitude ($H \leq 15$ $\text{kA}\cdot\text{m}^{-1}$) of applied magnetic field in MH [82] the only way to control the SLP is to optimize the properties of the magnetic material.

1.4.3. Mechanisms of heat generation

The heating ability of the mediator is determined by the magnetic nanoparticles which absorb the energy of AC magnetic field and converts it into heat and by the heat capacity of the carrier medium. The Joule heating by eddy currents is not considered for magnetic nanoparticles, as they usually have high electrical resistivity and their small size limits the eddy currents [90]. Generally, when the material is exposed to the external magnetic field the atomic magnetic moments are forced to align in the field direction. The degree of alignment depends on the field magnitude and on the properties of the material. When the polarity of the external magnetic field changes, the direction of magnetic moments changes to the opposite. If the external magnetic field is time varying then, from some frequency, the magnetic moment lags to orient to the field direction. And if the amplitude of the AC magnetic field is high enough to force the oscillation of magnetic moment then open hysteresis loops arise due to this lag.

Hysteresis losses in MD and SD nanoparticles

Physical phenomena leading to hysteresis in magnetic nanoparticles in AC magnetic fields differ depending on the magneto-structural properties of nanoparticles [23, 32]. In large particles consisting of more than one magnetic domain hysteresis in AC magnetic field arises due to domain wall motion and depends in a complicated manner on the type and configuration of wall pinning centres given by particle structure. In SD nanoparticles the reversal of the magnetization occurs via coherent rotation of all magnetic moments within the particle. If the anisotropy energy of the particle is higher than the energy of the field then the magnetization reversal is inhibited and hysteresis is observed.

Hysteresis for both MD and SD nanoparticles provides energy losses and subsequent heat. It was established that small SD nanoparticles generate significantly more heat and have higher SLP than large MD nanoparticles, as the surface anisotropy contributes much to the effective anisotropy of SD nanoparticles [91, 92]. For magnetite nanocrystals the coercivity and remanent magnetization were found to decrease with increasing particle size, d , according to an empirically established $d^{-0.6}$ power law [93]. Since, on the other hand, magnetite particles below D_{cr}^{SPM} become SPM, a maximum of hysteresis losses may be expected for single domain iron oxide particles with a particle size in the range between D_{cr}^{SPM} and D_{cr}^{SD} .

The heat generated by a system of magnetic nanoparticles which magnetization curves display hysteresis is equal to the area enclosed in the hysteresis loop:

$$W_{heat} = \mathbf{H} \cdot d\mathbf{M}. \quad (20)$$

The maximum heat generated by a magnetic material is generated in the AC magnetic field of sufficient frequency and amplitude, providing the hysteresis loop of height equal to $2 M_s$ and of width equal to $2\mu_0 H_c$. The maximum generated heat in this case is:

$$W_{heat}^{max} = 4M_s\mu_0H_c. \quad (21)$$

However due to the patient safety constraints, the frequency and amplitude AC magnetic field which are applied in MH do not provide the major hysteresis loop and the maximum heat is not attainable.

Magnetic losses in SPM nanoparticles

Special cases are the SPM nanoparticles, which by definition have zero coercivity, zero remanent magnetization, high saturation magnetization and do not interact with each other. Available thermal energy, $k_B T$, is sufficient to overcome the energy barrier, ΔE , enabling the magnetic moment to spontaneously rotate, via non-coherent rotation, without exhibiting hysteresis losses. Based on this knowledge one can expect that there is no heat generated from the work performed by the magnetic field on SPM nanoparticles. However in the experimental study the possibility of heat generation by SPM nanoparticles above a defined frequency called the blocking frequency was proposed [94]. Below the blocking frequency, a sample is SPM, but above it, hysteresis is observed. To explain this phenomenon characteristic relaxation times for spontaneous or thermally driven magnetization reversal should be referred (see section 1.1.2.). If the effective relaxation time of the system of SPM nanoparticles is shorter than the measurement time, then the magnetic moments spontaneously reverse and the total magnetic moment is zero. If the measurement time is shorter than the relaxation time, then during the measurement the magnetic relaxation is blocked because the AC magnetic field changes too fast. At the blocking frequency the experimental time equals to effective relaxation time. Maximum heat dissipation by relaxation mechanisms takes place at the optimum frequency, f , [95] when the effective relaxation time is:

$$\tau = \frac{1}{2\pi f}. \quad (28)$$

Eggeman et al. concluded that for a 9–10 nm iron oxide particle, the blocking frequency is 300 – 400 kHz, above which the magnetization lags from the field direction and hysteretic loss mechanism is activated [94]. The magnetic interactions between the individual particles were assumed to lower the blocking frequency compared to that for a single particles. The onset of hysteresis in the commercially available ferrofluid FluidmagDX by Chemicell (water-based ferrofluid of maghemite nanoparticles with size of 9.5 ± 4 nm stabilized with dextran, gathered in aggregates) was observed at 2 kHz.

Generally, it is advised to use frequency of several hundred kHz in combination with low field amplitude, few $\text{kA}\cdot\text{m}^{-1}$, for SPM particles and frequency of a few hundred kHz with high field amplitude, a few tens of $\text{kA}\cdot\text{m}^{-1}$, for ferromagnetic single domain particles [14]. In ideal case the AC magnetic field parameters should be adjusted to the particular type of nanoparticles or vice versa.

Effect of particle size distribution on heat generation

The magnetic nanoparticles for application in MH usually exhibit the variation of physical and magnetic properties, i.e. the variation of particle size, shape and anisotropy. The polydispersity of chemically synthesized magnetic nanoparticles is usually in the range of 10 – 30%. The effect of the polydispersity on the magnetic properties of nanoparticles and heat generation in AC magnetic field is an open question [32]. Theoretical calculations based on linear response theory revealed that the size distribution of nanoparticles reduces the heat generation [88, 96]. This is true for non-interacting nanoparticles. However strong interparticle interactions may moderate this effect, because the reversal of magnetic moment in nanoparticle produces a local field, which can be large enough to reverse the neighbouring nanoparticles. Therefore, nanoparticles, which are optimized for the particular AC magnetic field will drive other particles in a system to produce more heat [32].

Effect of interparticle interactions on heat generation

Interparticle interactions as it was already mentioned also have a large influence of the magnetic properties of nanoparticles and subsequently on the heat generation in AC magnetic field. Two types of magnetic interactions are described in the literature: long range dipole-dipole interactions and exchange interactions arising if the distance between the nanoparticles is not longer than 1nm. Dipole-dipole interactions are believed to be weak for SPM nanoparticles due to their small sizes and low value of magnetic moment. Controversial effects of interparticle interactions on heat generation are reported in literature. For commercial iron oxide nanoparticles FluidmagDX by Chemicell with the size corresponding to SPM state (9.5 ± 4 nm), which are assembled into aggregates of 48 – 90 nm, the heating effect increased with the increase of nanoparticles concentration in dispersion and subsequently with increase of interparticle interactions [94]. This effect can be explained by the hindering of the reversal of magnetic moment when single crystals form aggregates. Therefore, the reversal in individual nanoparticle can not occur independently. Individual magnetic moments in the aggregate of nanoparticles move cooperatively, leading to an increase of relaxation time and thus increase of hysteresis [32]. Meanwhile, in the same study no heating was demonstrated for single core iron oxide nanoparticles with average size of 10 nm prepared by thermal decomposition method regardless of the concentration of particles [94]. Another experimental study of Urtizbera et al. demonstrated that dipolar interactions led to a decrease of SLP of ferrofluid of non agglomerated nanoparticles 11 nm in diameter as the ferrofluid concentration was decreased [95]. The authors report SLP values of $0.38 - 0.89 \text{ W}\cdot\text{g}^{-1}$, i.e. $5 \text{ }^\circ\text{C}$ temperature increase (minimum required for hyperthermia) is reached within 127 – 236 minutes. This heating rate is very slow, and the ferrofluids of these nanoparticles are not suited for hyperthermia.

Carrier medium properties: effects on heat generation

Properties of the carrier medium, i.e. heat capacity and viscosity, also influence the heat generation. The specific heat capacity of the carrier medium has an impact on the rate of heating. One can expect that the same nanoparticles provide more rapid heating in glycerol medium, with specific heat capacity, $c_i = 2,43 \text{ J}\cdot\text{g}^{-1}\cdot\text{K}^{-1}$, compared to water with $c_i = 4,18 \text{ J}\cdot\text{g}^{-1}\cdot\text{K}^{-1}$. The specific heat capacities of living tissues differ, for example: $3.36 \text{ J}\cdot\text{g}^{-1}\cdot\text{K}^{-1}$ for soft tissues, $2.3 \text{ J}\cdot\text{g}^{-1}\cdot\text{K}^{-1}$ for subcutaneous fat, $3.6 - 3.7 \text{ J}\cdot\text{g}^{-1}\cdot\text{K}^{-1}$ for blood. As the SLP value is normalized to heat capacity (Equation 18), therefore the effect of heat capacity is taken into account. However, the viscosity of the medium is not considered when calculating SLP, though it is known to influence much on the relaxation phenomena of SD nanoparticles and thus on their heating effect. As the Brown relaxation time is proportional to the viscosity of the carrier medium and is suppressed in a viscous medium [14, 15], only Néel relaxation of magnetization accounts for heat generation at high viscosities. It was established theoretically for the model single core maghemite nanoparticles with polydispersity, $\sigma = 0.3$, displaying surface anisotropy that losses caused by the particles rotation make important contribution to the full magnetic response and heat ability in an AC magnetic field [15]. The particles size dependence of SLP at 500 kHz and $7.96 \text{ kA}\cdot\text{m}^{-1}$ under variation of fluid viscosity was established (Figure 21).

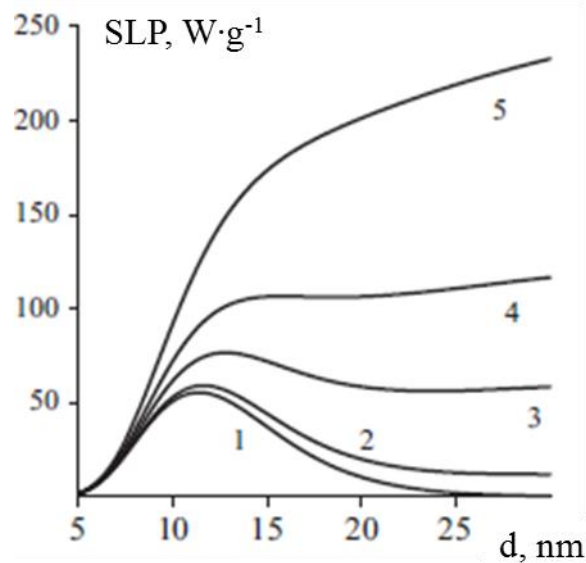


Figure 21. Particle size dependence of SLP at 500 kHz $7.96 \text{ kA}\cdot\text{m}^{-1}$ in a model single core maghemite nanoparticles under variation of the carrier medium viscosity: (1) $\eta = 1 \text{ Pa}\cdot\text{s}$, (2) $0.01 \text{ Pa}\cdot\text{s}$, (3) $0.002 \text{ Pa}\cdot\text{s}$, (4) $0.001 \text{ Pa}\cdot\text{s}$, (5) $0.0005 \text{ Pa}\cdot\text{s}$. Adapted from [15].

As it is seen from the figure 21, when the viscosity of the medium is higher than $0.01 \text{ Pa}\cdot\text{s}$ the maximum attainable SLP of magnetic nanoparticles is about $50 \text{ W}\cdot\text{g}^{-1}$.

To sum up, the heat generation strongly depends on the collective properties of an ensemble of magnetic nanoparticles (particles size and shape, magnetic anisotropy, size distribution, interparticle interactions), parameters of the AC magnetic field and the properties of the carrier medium.

1.4.4. Magnetic materials for thermotherapy

Different nanomagnetic materials were investigated for application in MH with a view of their heating potential and/or targeting capabilities. Among these materials are iron oxide nanoparticles (magnetite and maghemite), iron-palladium, iron-platinum, cobalt, nickel, cobalt ferrite, manganese-zinc ferrite, copper-nickel, ferromagnetic perovskites, gadolinium-, calcium-, and lanthanum complexes, and ferrimagnetic $\text{SrFe}_{12}\text{O}_{19}/\gamma\text{-Fe}_2\text{O}_3$ composites [83, 97-101]. Composite materials with a defined Curie temperature just above the therapeutic temperatures were proposed, for example Mn-Zn-Fe, Co-Gd-Zn and Zn-Gd-Fe composites [102, 103]. These materials provide the control over the temperature increase preventing the overheating.

Iron oxide nanoparticles exhibit a medium heating efficiency with minimal control of *in-vivo* temperature evolution during MH in comparison with other magnetic materials [97]. However the majority of both experimental and commercially available magnetic nanoparticles designed for MH are iron oxide nanoparticles rather than other mentioned materials (examples can be seen on the web pages of the most eminent companies in MH: www.magforce.de and www.sennewald.de) [83]. Several reasons account for application of magnetic iron oxides [104]. Foremost iron oxide nanoparticles are biocompatible, as was proved via various methods and no considerable toxicity was found [105], whereas other magnetic particles have shown considerable toxicity in the same dosage [106, 107]. Iron oxide nanoparticles have high magnetization, possess better chemical stability against oxidation than metal nanoparticles. In addition, the integrative therapeutic and diagnostic (i.e. theragnostic) capacity of iron oxide nanoparticles is of crucial importance in medicine in order to reduce side effects in patients [108].

1.4.5. Progress in magnetic hyperthermia

Since first *in-vivo* investigations of the application of magnetic materials for tumor treatment by Gilchrist et al. dated back to 1957 [81], there have been numerous studies published describing a variety of schemes using different types of magnetic materials, different field strength and frequencies, and different methods of encapsulation and delivery of the particles. Many efforts have been devoted in the last 30 years to the development of inductive heating applicators, to the improvement of magnetic mediator heating efficiency and tumor targeting ability and to the application of MH in clinical medicine.

Applicator development

There are several commercial inductive heating applicators available, for example *Magnetherm* by nanoTherics, *DM100 series* by nB NanoScale Biomagnetics and *MFG-1000* by Implementa Hebe AB [13]. However many research team utilize a home-made AC magnetic field generators [44, 45, 109]. Among these some home-made devices were patented. For example, *Magnetic Alternating Current Hyperthermia* (MACH) by Resonant Circuits Ltd., London, United Kingdom, which is very compact and highly configurable. Its hand-held 2 cm coil with 6 windings, cooled by water allows for miniaturization and even catheterization of the applicator. The MACH generates the AC magnetic field of $12 \text{ kA}\cdot\text{m}^{-1}$ at a frequency of 1.05 MHz.

The first inductive heating applicator for humans, *Nanoactivator*[®] was developed by Jordan and his colleagues and commercialized by MagForce Nanotechnologies AG, Berlin, Germany. Apparently its prototype was the device MFH Hyperthermie systeme GmbH, depicted on figure 20. *Nanoactivator*[®] comprises a resonant circuit at a ferrite yoke that generates a homogeneous AC magnetic field of up to $15 \text{ kA}\cdot\text{m}^{-1}$ at frequency of 100 kHz. At the same time, the machine allows for real time patient temperature measurements to ensure that neither the upper limit of the therapeutic temperature threshold is exceeded, thus preventing thermal ablation, nor the lower, ineffective limit is crossed. The aperture is adjustable in order to get a constant field at treatment site. The tumors of up to 5 cm in all parts of the body can be in principle treated. The applicator is complemented with a ferrofluid, NanoTherm[®], or MFL AS magnetic fluid, containing SPM magnetite and maghemite nanoparticles, 15 nm size, coated with aminosilane and dispersed in water. The total iron concentration in magnetic fluid is $112 \text{ mg}_{\text{Fe}}\cdot\text{ml}^{-1}$. The treatment planning software, *NanoPlan*[®], calculates the temperature distribution from nanoparticles distribution density, their SLP and perfusion at the tumor area derived on the base of series of comprehensive MRI scans.

Magnetic material development

The heating efficiency of the mediator is evaluated by SLP or SHP. The effectiveness of tissue heating is characterized by SAR (see section 1.3.2. and 1.4.2.). Direct comparison between SLP values of iron oxide nanoparticles prepared by different research groups is rather complicated because SLP is not the intrinsic property of the material but depends also on AC magnetic field amplitude (H) and frequency (f) and on the properties of the carrier medium. Recently, a parameter enabling the comparison was introduced. It is an intrinsic loss power (ILP) defined as SLP normalized to $H^2\cdot f$ [110]. The ILP magnitude is expressed in $\text{nHm}^2\cdot\text{kg}^{-1}$ units. For calculation of ILP the SLP value should be taken in $\text{W}\cdot\text{kg}^{-1}$, field amplitude in $\text{kA}\cdot\text{m}^{-1}$ and field frequency in kHz. The application of ILP implies that the imaginary part of complex magnetic susceptibility of magnetic nanoparticles, χ'' , is frequency-independent in the range of frequencies of hyperthermia treatment

(10 kHz – 1 MHz) [88]. The later definition is rather questionable. There are theoretical and experimental data that χ'' of magnetic nanocomposites is a function of frequency in the range of hyperthermia treatment [111-114]. However, nowadays it is the only method for comparison of materials heating efficiency. For evaluation of heating efficiency the ILP value should be considered together with the SLP value, as low SLP measured at weak AC magnetic field and low frequency may give high ILP. Table 4 represents the highest reported values of SLP and ILP of iron oxide nanoparticles prepared by different methods by different research groups.

Heating effect of nanoparticles is determined by a complex of interrelated magneto-structural properties: size, shape, size distribution, magnetization, coercivity and interparticle interactions (See section 1.4.3.). For magnetosomes nanocrystals the dominant effect on the heating efficiency has their arrangement in the magnetic chains, which increases effective magnetic anisotropy and accounts for the abnormal heating effect. Iron oxide nanocubes obtained by thermal decomposition of iron (III) acetylacetonate are an example of surface anisotropy effect [109]. Nanoparticles obtained by precipitation of iron salts are usually gathered into aggregates, for example multicore nanoparticles of 30 – 160 nm hydrodynamic volume consisting of small iron oxide nanocrystals of 10 – 14 nm, thus interparticle interactions favour the heat generation [43, 47]. In the case of a single core nanoparticles without interparticle interactions having narrow size distribution, the size effect dominates and if the size of the particles is optimized to the field parameters high losses can be achieved [44, 115].

As can be seen from the table 4, ILP is not good parameter for comparison because for the same nanoparticles Nanomag-D-spio by Micromod GmbH the ILP obtained by different authors differ considerably as the SLP was measured in different fields. All high values of SLP of the order of 1 – 2 kW·g⁻¹ were obtained at high field amplitudes, strongly exceeding the allowed limit of 15 kA·m⁻¹ (see section 1.4.2.). The SLP values decrease considerably when the materials are subjected to the AC magnetic fields of lower amplitude [89, 109]. Moreover, all the highest reported values of SLP were obtained on water dispersions of nanoparticles. The viscosity of water at temperatures of 20 – 50 °C is in the range of 0.001 – 0.0005 Pa·s, and both Néel and Brown relaxation mechanisms account for heat generation. Therefore for practical application of MH there is a need for the development of iron oxide magnetic nanoparticles with high heat losses in allowed AC magnetic fields and in viscous mediums.

Table 4. Examples of experimental SLP data and corresponding ILP values of iron oxides nanoparticles at different AC magnetic fields.

Nanoparticles	d , nm	H , kHz	f , kA·m ⁻¹	SLP, W·g ⁻¹	ILP, nHm ² ·kg ⁻¹	Ref.
Magnetosomes from magnetotactic bacteria	38	410	10	960	23.42	[35]
Iron oxide nanocubes obtained by organic method	19	520	29	2452	5.61	[109]
Multicore nanoparticles prepared by polyol process, citrate-stabilized	30 (10)	520	29	1500	4.6	[47]
Size sorted multicore nanoparticles prepared by coprecipitation method, carboxymethyl-dextran-stabilized	82 (14)	400	10	332	8.3	[43]
Multicore nanoparticles prepared by coprecipitation method, tiopronin-stabilized	135 (9)	1050	12	1179	6.1	[45]
Size-sorted single core nanoparticles prepared by coprecipitation method, with citrate coating	16	700	24.8	1650	3.83	[44]
Iron oxide nanoparticles obtained by organic method	16	373	14	140	1.91	[115]
Nanomag-D-spio by Micromod GmbH, multicore nanoparticles, dextran-stabilized	100(10-12)	900	5.66	90	3.12	[110]
		150	94	162	0.1	[89]
BNF-Starch by Micromod GmbH, multicore nanoparticles, starch-stabilized	100(15-20)	150	94	537	0.4	[89]

d is average particle diameter, for multicore nanoparticles hydrodynamic radius and in brackets the size of the nanocrystals forming the aggregate.

In-vivo studies and clinical trials

The era of *in-vivo* studies on animal models of MH was initiated by Gordon et al., who injected dextran coated SPM iron oxide nanoparticles intravenously into Sprague-Dawley rats and confirmed the creation of local heating *in-vivo* [116]. In a similar study Hergt et al. injected dextran-coated magnetite into the tail vein of Sprague-Dawley rats and treated with AC magnetic field of 450 kHz (unknown amplitude)[117]. Tumor shrinkage and tissue necrosis were observed. Matsuoka et al. reported the *in-vivo* efficiency of MH with magnetic cationic liposomes for hamster osteosarcoma [118]. Magnetic cationic liposomes representing the SPM magnetite particles of 10 nm in diameter, coated by a lipid membrane were injected directly into the osteosarcoma. Then the animals were subjected to the AC magnetic field of 118 kHz and unknown amplitude. The authors report the tumor heating above 42 °C and the complete regression was observed in all animals of the treated group (Figure 22).

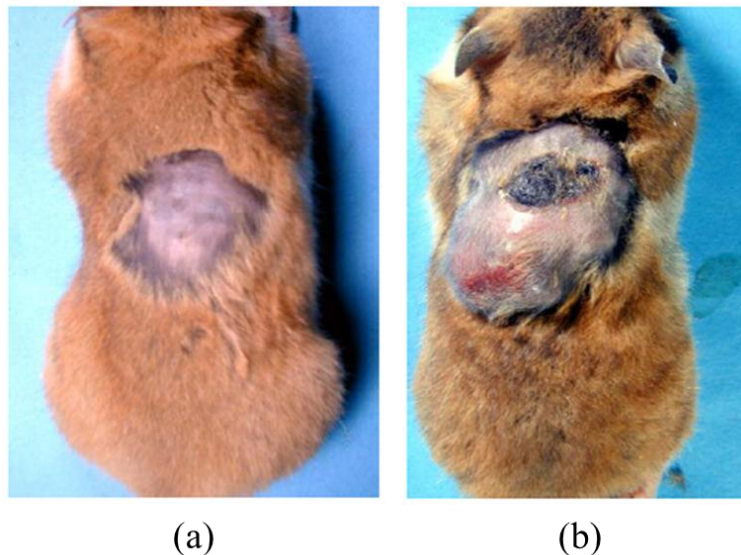


Figure 22. Photographs of hamsters bearing osteosarcoma at 20 day of the study [118]: (a) treated by MH with magnetic cationic liposomes, (b) control group, untreated hamster.

The first-ever clinical studies of therapeutic MH were started by the research group of Jordan [80]. They built the inductive heating system, *Nanoactivator*[®], utilizing a ferrofluid *NanoTherm*[®] and developed the treatment planning software trade-marked as *NanoPlan*[®]. Concentration of ferrofluid and the temperature distribution were evaluated on the base of series comprehensive MRI scans of the injection sites.

In 2007 and 2011 Jordan's group reported the results of the clinical study of MH in human patients [119, 120]. The studies involved the treatment of patients with recurrent glioblastoma multiforme, the most common and deadly type of brain cancer, via a combination of fractionated external beam radiotherapy and several

sessions of thermotherapy. The magnetic fluid of aminosilane coated iron oxide nanoparticles was injected into multiple sites throughout each tumour. Each tumour was injected with 0.1 – 0.7 ml of ferro-fluid per ml of tumour and then exposed to AC magnetic field of 3.8 – 13.5 kA·m⁻¹ at 100 kHz. The temperature was measured by intracranial thermometry catheter. The study demonstrated that this form of thermotherapy using magnetic nanoparticles could be safely applied to the treatment of brain tumours and that hyperthermic temperatures could be achieved (Figure 23). Magnetic fluid could be precisely deposited within the targeted area and the deposition was stable over several weeks, thus offering the possibility of repeated heat treatment without repeated application of the mediator.

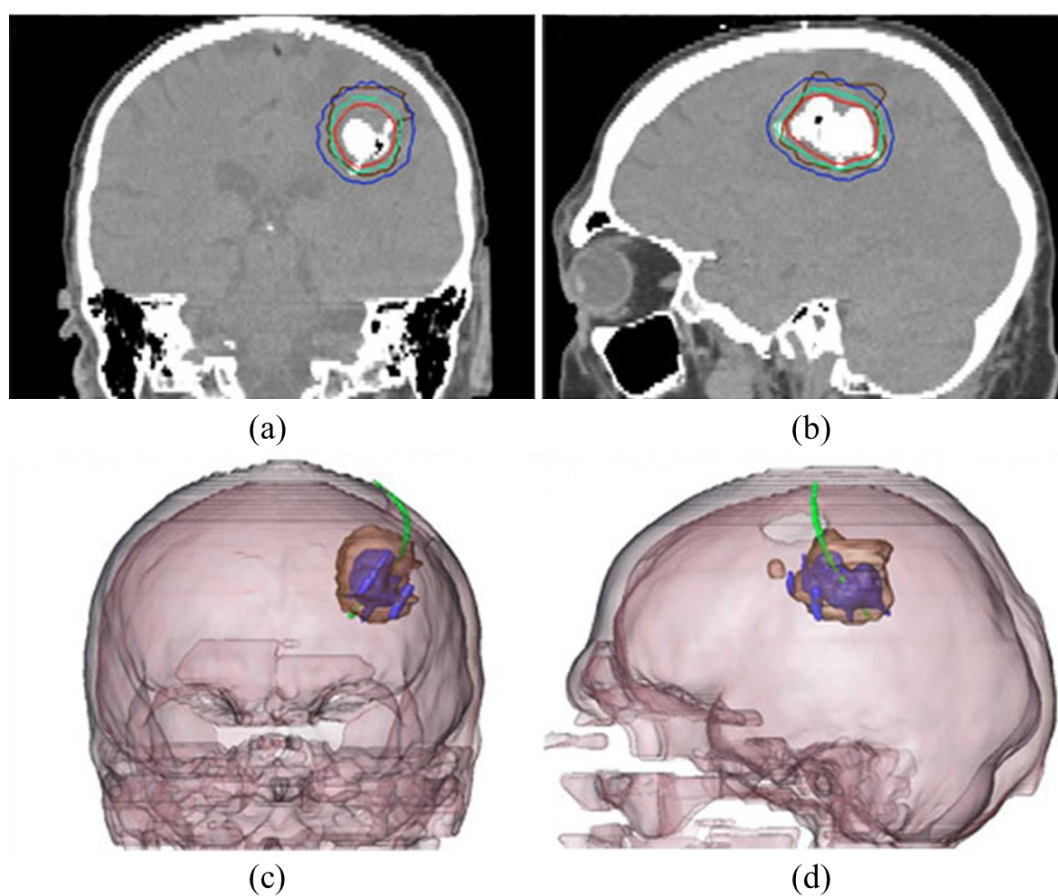


Figure 23. (a,b) CT images showing magnetic nanoparticle deposition as hyperdense areas. Isothermal lines indicate calculated treatment temperatures between 40 °C (blue line) and 50 °C (red line). The brown line represents the tumor area; (c,d) 3-D reconstruction of fused MRI and CT showing the tumor (brown region), magnetic fluid (blue region) and thermometry catheter (green line). Adapted from [120].

Promising clinical outcomes were observed, the therapy was well tolerated by patients and the overall increase of survival from 6.2 month for radio- and chemotherapy treatments to 13.4 month for MH combined with radiotherapy were

reported. This methodology received European regulatory approval for brain tumors treatment throughout European Union.

Group of Johannsen utilized *Nanoactivator*[®] for clinical studies of the treatment of prostate cancer [121, 122]. The magnetite nanoparticles, 15 nm size with aminosilane-like coating were installed in the tumor under transrectal ultrasound and fluoroscopy guidance. The AC magnetic field of $2.5 - 15 \text{ kA}\cdot\text{m}^{-1}$ at 100 kHz was applied. The interprostatic measured temperatures were 40.1 °C. The difficulties in achieving a homogeneous heat distribution due to the different thermal conductivities of the prostate surrounding tissues as well as a temporal impairing of patients quality of life and local discomfort observed for field intensities over $4 - 5 \text{ kA}\cdot\text{m}^{-1}$ were reported.

Recently the first clinical studies of application of MH for the treatment of metastatic bone tumours were reported by Matsumine et al. [123]. Cylindrical-coil AC magnetic field generator working at a frequency of 1.5 MHz inside which the affected limb can be inserted was used. “Bare” magnetite nanoparticles and calcium phosphate cement, a biocompatible bone substitute, were implanted during the surgical intervention. The reduction of tumor and visible new bone formation took place in 32 % patients, 64% showed no progressive lesions for more than three months and just 4% presented had poor response to the treatment. These results are comparable to those obtained with a combined treatment of radiotherapy and surgical intervention, thus suggesting the effectiveness of MH in this particular study.

Rather long period of gestation from first *in-vivo* studies to eventual clinical application reflects the considerable technological and regulatory difficulties to be overcome in any attempt to develop a clinically acceptable and effective MH therapy. It is not merely enough to develop magnetic particles that heat upon exposure to a tolerable AC magnetic field, although that is clearly an important task. It is also important to know how to appropriately administer the mediator to the desired tumor tissue, to retain it long enough in the tissue. MH is the most promising among all hyperthermia modalities for cancer treatment. However the heating of the tumor is based on the interplay between series of very complex physical and physiological phenomena. The existing challenges to be overcome are:

- (1) Design of a magnetic nanoparticles which possess effective tumor heating,
- (2) Development of a mediator on the base of magnetic nanoparticles which can be delivered and retained in the tumor long enough for thermal treatment and provide a homogeneous nanoparticles distribution.

1.5. Arterial embolization hyperthermia

AEH is the type of MH treatment when the artery supplying blood to the tumor is used for delivering the mediator. The mediator often causes the cease of tumor blood supply; therefore AEH usually involves the combined effect of hyperthermia and arterial occlusion. AEH seems to be the most suitable for the treatment of parenchymal organs malignancies, due to the nature of their blood supply, which is implemented mostly by the hepatic arterial system. For example, blood supply of the liver tumor is implemented by hepatic arterial system; therefore the material infused into the hepatic arterial system will be preferentially delivered to the liver tumor [21, 124].

The embolization method is usually used in oncological practice for the treatment of tumours of parenchymal organs [69], it is the basis for the currently used methods of internal radiation therapy, hepatic arterial chemotherapy and transarterial chemoembolization [21]. The embolization method is based on the intraorganic arterial occlusion causing ischemic necrosis of the tumor, limiting the ingress of viable cancer cells, as well as their debris (decomposition products) in the bloodstream, decreasing the probability of metastases and lowering the intoxication of the organism. For patients with locally advanced and generalized forms of neoplastic diseases such way is very often the only one possibility to prolong their life and to improve their state. In some cases the embolization treatment results in a decrease of tumor volume, allowing to perform the surgical operation.

AEH is so far an experimental cancer treatment method. In AEH the effect of arterial occlusion is combined with hyperthermic effect therefore enhancing the effectiveness of temperature distribution in tumor and providing the possibility for repeated hyperthermia treatments.

Several *in-vivo* studies explored the AEH. Matsuki et al. demonstrated the possibility to reach the therapeutic temperature of 43 °C in the dog kidney embolized with 200 µm capsules containing 50 µm metal flakes (iron, phosphorus, chromium and carbon) under exposure to AC magnetic field of 7 kA·m⁻¹ at 200 kHz [125]. However, no information about subcutaneous and skin temperature was provided, nor the post-treatment survival was considered.

Yu et al. reported the AEH study on rabbit hepatic tumours when the heating was performed by As₂O₃ nanoparticles 40 nm in diameter [124]. The nanoparticles were dispersed in Lipiodol, an iodine addition product of ethylesters of fatty acids obtained from poppy seed oil. Lipiodol is usually utilized for chemoembolization of hepatic carcinomas due to its selective and prolonged retention within the tumor [126]. The dispersion of nanoparticles was injected into the artery and the animals were subjected to AC magnetic field of 80 kHz frequency and 5 – 10 kA·m⁻¹ amplitude. The therapeutic temperatures were achieved in the tumor. However due to higher concentration of nanoparticles at the tumor rim lead to higher temperatures compared to the core temperature. The tumor growth inhibition and improvement of survival time was demonstrated.

Mitsumori et al. tested AEH with dextran coated magnetite multicore particles, 75 nm in diameter consisting of 7 nm cores, suspended in lipiodol on rabbits with implanted hepatic carcinomas under exposure to $21.6 \text{ kA}\cdot\text{m}^{-1}$ magnetic field alternating at 100 kHz [127]. The tumor temperature increase of $0.6 - 1.4 \text{ }^\circ\text{C}\cdot\text{min}^{-1}$ was recorded.

Moroz et al. demonstrated the similar heating rate ($0.5 - 1.0 \text{ }^\circ\text{C}\cdot\text{min}^{-1}$) with maghemite particles of 100 – 200 nm in diameter suspended in Lipiodol exposed to AC magnetic field of $30 \text{ kA}\cdot\text{m}^{-1}$ and 53 kHz on rabbits with hepatic carcinoma [128]. Studies on small animals involving tumor models demonstrated the achievement of therapeutic temperatures. However the particle distribution and toxicity issues are not well discussed. The applied AC magnetic fields in most of studies excide the tolerated limit established for MH.

Le Renard et al. investigated the use of *in situ* implant formation of organogel formulations, consisting polymers and magnetic nanoparticles diluted in organic solvents *in-vivo* on human cancer tumours xenografted in mice [84]. After injection of the formulation the organic solvent diffuses into tissues and water triggers precipitation of polymer, which entraps the magnetic nanoparticles. The polymer matrix prevents the phagocytosis and distant migration of iron oxide nanoparticles. The authors used poly(ethylene-vinyl alcohol) diluted in dimethylsulfoxide and magnetic microparticles consisting of SPM iron oxide nanoparticles in silica matrix. The SLP of the order of $18 \text{ W}\cdot\text{g}^{-1}$ was reported for these microparticles at $9.66 \text{ kA}\cdot\text{m}^{-1}$ and 144 kHz. The effective embolization of vascularized and necrotizing tumours was demonstrated; however, very high toxicity of the organogel formulations puts into question their practical application.

J. A. Mosso et al. proposed a ferrosilicone preparation composing of poly(dimethylsiloxane), stannous octolate to catalyse the vulcanization, silicone fluid as plasticizer and carbonyl iron filler [129]. The composition is injected in a liquid form through catheters and held in desired place in blood vessels by an external magnetic field until vulcanization occurs. The authors demonstrated selective occlusion of dog renal vascular beds and peripheral arteries. The main drawbacks of proposed embolization material are the necessity to use a strong magnetic field and the high toxicity of the catalyst.

According to our knowledge AEH was trialled in humans only in Russian Research Centre for Radiology and Surgical Technologies in St. Petersburg. Granov et al. developed a ferrocomposite for embolization, on the base of silicone elastomer comprising the carbonyl iron and the method of its application for the treatment of parenchymal organs [130-132]. Ferrocomposite does not require external magnetic field to be held in the blood vessels. It is permitted by the Russian Ministry of Health for the treatment of the tumours of parenchymal organs. The presence of magnetic particles in the embolization material enables the conductance of repeated hyperthermia treatment by RF electromagnetic fields. Clinical trials on 12 patients with liver and renal cancer revealed significant tumor volume reduction, prolonged survival and general enhancement of patients filing. Though the composition

obtained demonstrated safe embolization ability, it's heating efficiency is low. The hyperthermic temperatures are reached only in 30 minutes for composites with 10 wt. % of carbonyl iron under exposure to 27 MHz frequency electromagnetic field with 3 – 80 W power. Moreover the application of such high frequency electromagnetic fields may cause undesired side effect in the form of heating of subcutaneous fat.

Despite these encouraging results, the method of AEH needs further improvement. The main limitations to be overcome are the absence of magnetic material providing effective heating at AC magnetic field of mild amplitudes, which decrease the probability of fat and skin burns by eddy currents; and the inhomogeneity of magnetic nanoparticles distribution in the tumor, leading to regions with insufficient heating and overheating. The *in-situ* formulations comprising the SD iron oxide nanoparticles should be able to overcome these shortcomings.

AIM AND OBJECTIVES OF WORK

The aim of the work is elaboration of polymer magnetic composite to be used in AEH.

The aim of the work will be accomplished by:

1. Synthesis of magnetic iron oxides nanoparticles with the set of magneto-structural properties providing high heating rate in AC magnetic fields allowed for application in MH.
2. Development of polymer magnetic composite on the base of nanoparticles obtained with rheological properties allowing delivery and retention of mediator in the tumor vessels, high heating rate in AC magnetic field at moderate amplitudes, and radiopaque property to control the distribution of material in blood vessels.

CHAPTER 2. METODOLOGY

2.1. Synthesis of iron oxide nanoparticles and polymer composites on thereof

Of particular importance for MH is the preparation of magnetic mediator consisting of magnetic nanoparticles and the carrier medium. As it was pointed out in section 1.4.3., the magnetization process of an ensemble of magnetic nanoparticles in external magnetic field is governed by a complex interplay between several parameters: (1) magneto-structural properties of nanoparticles (morphology, magnetization saturation, coercivity, magnetic anisotropy, *etc*), (2) experimental conditions (amplitude and frequency of AC magnetic field), (3) particles concentration (dosage), and (4) properties of carrier medium (viscosity and heat capacity).

2.1.1. Synthesis of iron oxide nanoparticles by coprecipitation method

It has been established theoretically that iron oxide nanoparticles in the SD state provide maximum heating effect [13, 96]. Among chemical synthesis methods existing for the preparation of iron oxide nanoparticles coprecipitation method seem to be the most suitable. In this method iron (II) and iron (III) salts solutions (iron source) react with alkali solution (precipitating agent). The initial reagents are non-toxic, it is possible to obtain large amount of nanoparticles at eco-friendly conditions and at temperatures not exceeding 100 °C. Coprecipitation method allows to obtain iron oxide nanoparticles without surfactant overlayer affecting on their magnetic properties and biocompatibility. Moreover, coprecipitation method is believed to resemble the formation of magnetite nanoparticles by magnetotactic bacteria whose magneto-structural properties favor to the high SLP value [133].

In the current study ferrous and ferric chlorides were used as iron source and ammonium hydroxide as precipitating agent. In the typical synthesis 300 ml of 0.38 M ammonium hydroxide solution was mixed with a 30 ml of ferrous chloride tetrahydrate and ferric chloride hexahydrate solution with a molar ratio of Fe (II) / Fe (III) = 0.0125 / 0.025 = 0.5, i.e. equal to that of stoichiometric magnetite. The reaction was performed in a round-bottom flask, equipped with a condenser, mechanical stirrer, dropping funnel and thermometer (Figure 24).

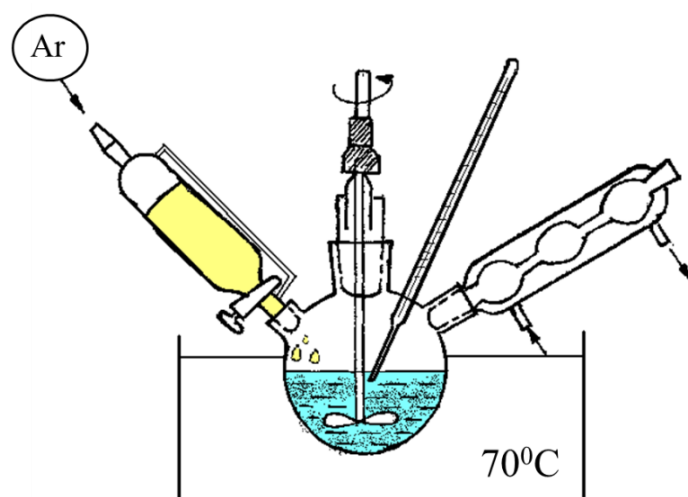


Figure 24. Schematic representation of the setting for the iron oxide nanoparticles synthesis.

The reaction was performed in an argon atmosphere to prevent the oxidation of Fe^{2+} ions and to keep the Fe (II) / Fe (III) molar ratio constant. The temperature of the reaction mixture was maintained at $70\text{ }^{\circ}\text{C}$ by means of water bath. The stirring speed was 700 rpm. During the synthesis either ammonium hydroxide solution was added dropwise ($2\text{ ml}\cdot\text{min}^{-1}$) to ferrous and ferric chloride solution, or the salts solution was added to the base solution ($0.2\text{ ml}\cdot\text{min}^{-1}$). The black powder of iron oxide nanoparticles formed in the reactions was separated by a permanent magnet, washed with distilled water to neutral pH and dried in air at room temperature. The synthesis of all samples was carried out at least 10 times in order to verify the reproducibility of structural and magnetic properties of nanoparticles.

To analyse the growth dynamics of magnetite from a solution, the structural and magnetic properties of reaction intermediates were studied. To this end, the reaction was stopped at different stages of the synthesis, and the reaction products were separated with the help of a permanent magnet and dried in air.

The post treatment of nanoparticles involved the annealing at $300\text{ }^{\circ}\text{C}$ in air for several hours. The annealing caused full or part oxidation of magnetite nanoparticles to maghemite.

2.1.2. Synthesis of the magnetic polymer composite

In the current study the magnetic polymer composite for the application in AEH was developed. It combines the ability for effective embolization and attaining of hyperthermic temperatures.

The choice of the embolization agent depends on the patient's structural feature and lesion to be treated; however, in any case, it should meet the following requirements: non-toxicity, non- antigenicity, stability to lysis and radiopaque property [69, 134]. Moreover, at the step of delivery, the material should be of low viscosity to pass through angiographic catheters and fill in not only the main artery

but also periphery arteries and small blood vessels. Then, the material should cause the stop of blood flow, for example, due to the rapid increase of material's viscosity.

The very promising materials for embolization are silicone elastomers, their viscosity and the curing rate can be set by their composition. The silicone rubbers are biocompatible and do not display adhesion to living tissues; they are soft materials and do not injure the bloodstream [135]. Meanwhile silicone densely adjoins to walls of blood vessels, reducing the probability of the blood flow recovery. The low specific heat capacity of silicon elastomer of $1.05 - 1.30 \text{ J}\cdot\text{g}^{-1}\cdot\text{K}^{-1}$ is also advantageous, because it favours the distribution of heat generated by incorporated magnetic nanoparticles [136]. There are several silicon compositions proposed for the embolization of brain vessels [137], vessels of parenchymal organs [138] and silicon composite materials tested in small animals on tumor models [129, 139, 140]. To attain the hyperthermic temperatures the silicone elastomers should be filled with the magnetic material effectively absorbing the energy of external AC magnetic field and transforming it into heat.

In the current study a bi-functional magnetic composite, combining the embolization ability and high heating efficiency in AC magnetic fields was prepared. The silicone elastomer was used as a matrix of the composite. It was prepared analogously to the one described in patent [141] by the hydrosilylation reaction of silicones with vinyl- and hydro-side groups, which is commonly applied for manufacturing of silicone rubbers [142]. As a magnetic phase of composite the maghemite nanoparticles with high heating potential developed in the current study were used.

For the preparation of silicone magnetic composite poly(dimethylsiloxane-co-methylvinylsiloxane), maghemite nanoparticles and catalyst containing chloroplatinic acid were mixed in the vessel A (Figure 25). Another mixture containing poly(dimethylsiloxane-co-methylhydrosiloxane) and poly(dimethylsiloxane) was prepared in the separate flask, vessel B. Then the contents of the vessels were mixed and the hydrosilylation reaction started leading to polymer crosslinking. The main characteristics of the initial reagents of silicone elastomer are:

- Poly(dimethylsiloxane-co-methylvinylsiloxane) of viscosity of 2.6 Pa·s at 25 °C, 0.1 – 0.4 wt. % of vinyl- groups;
- Poly(dimethylsiloxane-co-methylhydrosiloxane) of viscosity of 0.65 Pa·s at 25 °C, 0.55 wt. % of hydro- groups;
- Poly(dimethylsiloxane), of viscosity 0.03 Pa·s at 25 °C;
- Chloroplatinic acid dissolved in poly(dimethylsiloxane) at concentration of 37.77 wt.% of platinum.

For sake of simplicity the following abbreviations for the initial components of composite are utilized: PVS for poly(dimethylsiloxane-co-methylvinylsiloxane);

PHS for poly(dimethylsiloxane-co-methylhydrosiloxane); PDMS for poly(dimethylsiloxane) and CAT for catalyst in the form of chloroplatinic acid dissolved in poly(dimethylsiloxane).

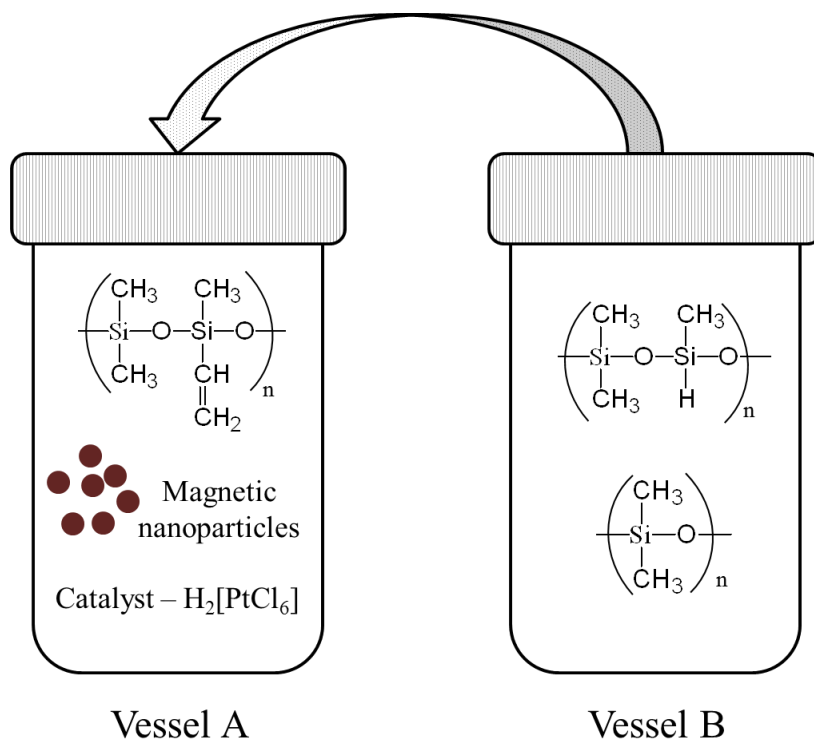


Figure 25. Schematic representation of magnetic polymer composite preparation.

2.2. Characterization of iron oxide nanoparticles and composites

The characterization of properties of nano-sized materials is rather a complicated task due to the lack of instruments allowing to observe the materials on the nanometre level. Usually the group characteristics are determined rather than properties of a single nanoparticle in an ensemble. For nanomaterials the short range forces have a significant impact on their properties, while on the macroscopic level they do not play a significant role. In the current study the characterization of both nanoscale materials and macroscopic polymer composites was conducted by using the methods briefly described above.

2.2.1. Morphology

As it was stated before the particle size, shape and size distribution determine the properties of magnetic nanoparticles in the large extent. The analysis of the nanoparticles morphology is usually performed by means of transmission electron microscopy (TEM) and scanning electron microscopy (SEM) [143, 144].

Transmission Electron Microscopy

In TEM a beam of electrons with energy of 50 – 200 keV are transmitted through an ultra-thin sample specimen and interact with the specimen. Electrons deflected by the atoms of the specimen and passed through the specimen enter the lens system. In this lens system the image is formed and focused onto an imaging device, such as fluorescent screen, on a layer of photographic film, or to sensor such as a charge-coupled camera. The resolution of TEM is down to 0.1 nm, which corresponds to the $1,5 \cdot 10^6$ times magnification. This enables to examine fine details, even as small as a single columns of atoms, which is tens of thousands times smaller than the smallest resolvable object in a light microscope. To study the morphology of micro- and nano- species (microcrystals, viruses, macromolecules, nanoparticles) they are deposited in the form of diluted suspensions onto support grids or films.

The crystal structure of the single nanoparticles can be determined by Fourier transformation of HRTEM images and the comparison of the obtained results with the database. The Fourier transformation is usually done by the software.

Scanning Electron Microscopy

In SEM a very thin electron beam (1-10 nm) with the energy of 0.2 – 40 keV, focused by condenser lenses, scans in a raster fashion over a rectangular area of the sample surface. The energy exchange between the electron beam and the sample results in the reflection of high-energy electrons by elastic scattering, emission of secondary electrons by inelastic scattering and the emission of electromagnetic radiation, each of which can be detected by specialized detectors. Electronic amplifiers of various types are used to intensify the signals, which are displayed as variations in brightness on a computer monitor. For imaging in the SEM, samples must be electrically conductive, at least at the surface, and electrically grounded to prevent the accumulation of electrostatic charge at the surface. Nonconductive samples are usually coated with an ultrathin layer of electrically conducting material (gold, gold/palladium alloy, platinum, etc.). Although SEM usually provides lower magnification than TEM, it provides a 3D image and information about microtopography of nanoparticles ensemble, whereas TEM provides a 2D image.

The average size of the nanocrystals can be also determined from the XRD data by means of using Scherrer equation, as will be discussed in the next section.

In the current study the following equipment was used to investigate the morphology of prepared nanoparticles:

- (1) High Resolution Scanning Electron Microscope, ZEISS Gemini Supra,
- (2) Transmission Electron Microscope, Philips CM12, with a wolfram cathode and 120 kV electron beam,

- (3) High Resolution Transmission Electron Microscope, JEOL JEM - 2100F, with a 200 kV field emission.

The statistical analysis of the average particle size was carried out on several HRSEM, TEM and HRTEM images with different magnification to detect both small and large nanoparticles with the help of Digital Micrograph Gatan software. For each sample, 200 particles were counted at least. The fast Fourier transformation of HRTEM images were performed with the Digital Micrograph Gatan software and the particular iron oxide was defined on with the Inorganic Crystal Structure Database (ICSD) database.

2.2.2. Chemical composition and crystal structure

Purity of a substance is of particular importance for the application in medicine. The determination of chemical composition and crystal structure for iron oxide nanoparticles is usually done by X-Ray diffraction (XRD) spectroscopy.

X-Ray diffraction spectroscopy

Generally, XRD involves interaction of electromagnetic radiation with a wavelength (λ) of around 0.1 nm, with the atoms in the solid. As the distances between the atoms in a crystal structure are comparable with the wavelength of the radiation, crystals can diffract the X-Rays. In certain directions (angles of incidence, θ) the elastically scattered rays interfere constructively, thus leading to enhanced intensity. These angles, θ , the wave length of the rays, and the lattice spacing (d_{hkl}) are related by the Bragg equation:

$$n\lambda = 2d_{hkl}\sin\theta. (29)$$

The XRD pattern of a powdered phase is a plot of the observed diffraction intensity against the Bragg angle, θ . Depending on the interference conditions each atom plane produces a series of n reflections. From these patterns the interplanar spacings (d_{hkl} values) can be calculated using the Bragg equation. Each compound has its own characteristic set of d_{hkl} values and intensities which can be used for identification. X-Ray diffractogram provides three parameters, namely line (angle) position, width and intensity from which the nature of the material, its quantity (in a mixture), its unit cell parameters and its crystallinity (crystal size and order) can be deduced. Typical XRD patterns of the magnetic iron oxides are shown in figure 26.

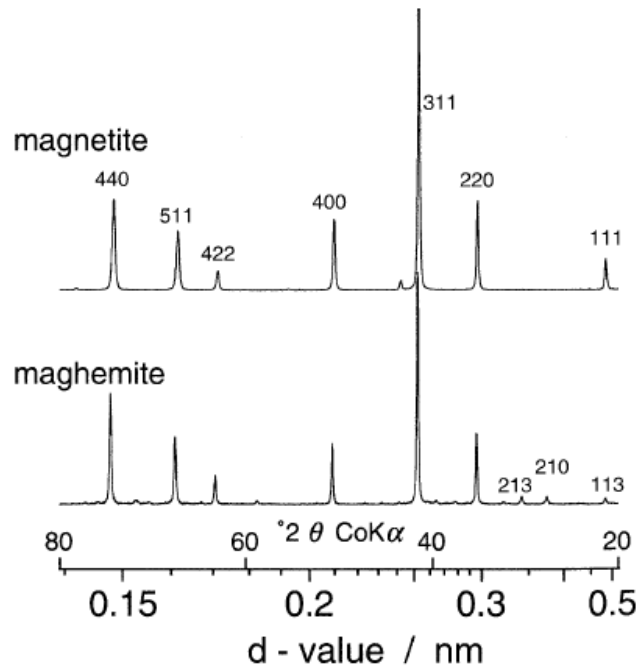


Figure 26. X-ray powder diffractograms of bulk magnetic iron oxides: magnetite and maghemite. Adapted from [24].

As it is seen from figure 26, the diffraction patterns for magnetite and maghemite are very similar, which makes difficult to distinguish between them. The small particle size causes the broadening of the reflection. Therefore, Rietveld refinement analysis is performed in order to estimate the relative quantities of magnetite and maghemite.

The average crystallite size can be determined from the line width analysis (the most intense peak (311)) of XRD data using Scherrer equation [145]:

$$d_{XRD} = \frac{K\lambda}{b \cos \theta}, \quad (22)$$

where λ is the wavelength of the X-ray radiation, b is the line width at half-peak intensity and K is a shape factor, for example for magnetite it is 0.89.

In the current study the XRD spectroscopy was done by:

- (1) X'Pert PRO X-Ray diffractometer with monochromatic $\text{CoK}\alpha$ radiation at $\lambda = 0.179026$ nm equipped with an X'Celerator detector
- (2) PANalytical X-Ray powder diffractometer with $\text{CuK}\alpha$ radiation at $\lambda = 1.541874$ nm equipped with a PIXcel RTMS detector.

The XRD data were analysed by Rietveld refinement technique using the Fullprof program.

Energy Dispersive X-ray Fluorescence spectroscopy

Energy Dispersive X-Ray Fluorescence (EDXRF) spectroscopy is an analytical technique for the elemental analysis of a sample. It relies on the unique energy levels of the emission of photons (X-ray) ejected from the atoms [144]. When an incident electron or photon, such as X-ray, strikes an unexcited atom, the electron from the inner shell of the atom is ejected leaving a hole or electron vacancy (Figure 27). An electron from the outer shell fills the hole by lowering its energy, and simultaneously the excess energy is released through X-ray emission.

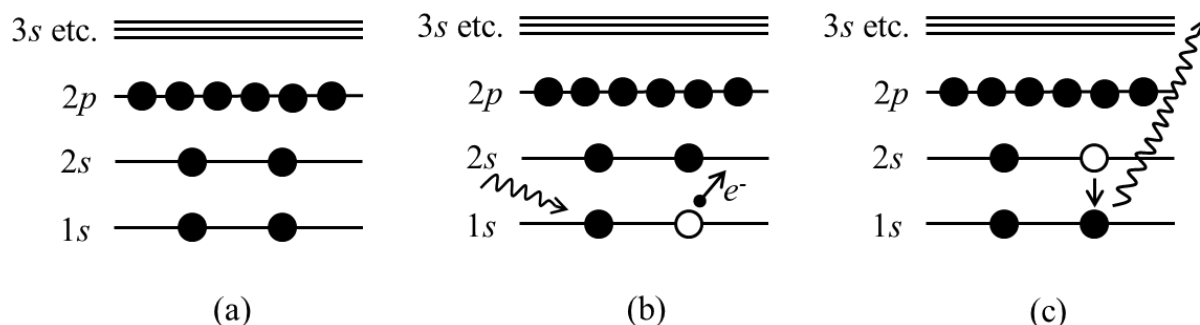


Figure 27. Schematic representation of electron energy transition: (a) initial state, (b) incident photon or electron ejects the 1s electron shell of the atom, (c) X-ray emission when 2s electron fills the hole.

The energy of the X-rays is characteristic of the energy difference between the two shells. Each atom in the Periodic Table has a unique electronic structure with a defined set of energy levels accounting for a set of peaks on its X-ray spectrum. The number and the energy of the X-rays emitted from a specimen is measured and on the base of these a chemical composition of the sample is determined.

In the current study the total iron content in the sample of iron oxide nanoparticles was determined by EDXRF with ARL Quant'X EDXRF Analyzer, Thermo Scientific.

Fourier transform infrared spectroscopy

Infrared spectroscopy is based on the interaction of molecules or crystals with electromagnetic radiation, or photons, in the wavelength range of 1 – 300 μm , i.e. wave numbers of 10000 – 33 cm^{-1} [24]. Molecules and crystals can be expressed as a systems of balls (atoms or ions) connected by springs (chemical bonds) [144]. These systems can vibrate with frequencies determined by the mass of the balls (atomic weights) and by the stiffness of the spring (bond strength). When the frequency of the impinging infrared radiation matches the transition energy of vibrating bond or group, the so called resonance frequency, then this radiation is absorbed by the material. These absorbed frequencies cause the excitation of

vibrations of chemical bonds and are specific to the type of bond and the atoms involved in the vibration. The intensity of the beam of infrared radiation is measured before and after the interaction with the sample and the infrared spectrum represents a plot of percent of absorbed radiation versus the frequency of impinging radiation, given in wavenumbers (cm^{-1}). The resolution and sensitivity as well as the time of measurement can be enhanced by applying the Fourier-transform infrared spectroscopy (FTIR).

One of the measurement modes in FTIR spectroscopy is called attenuated total reflectance FTIR (ATR-FTIR) it enables to measure a wide variety of solid and liquid samples without complex preparations. The basic principle is shown in figure 28. The sample is tightly attached to the ATR crystal, an infrared transparent material with a high refractive index.

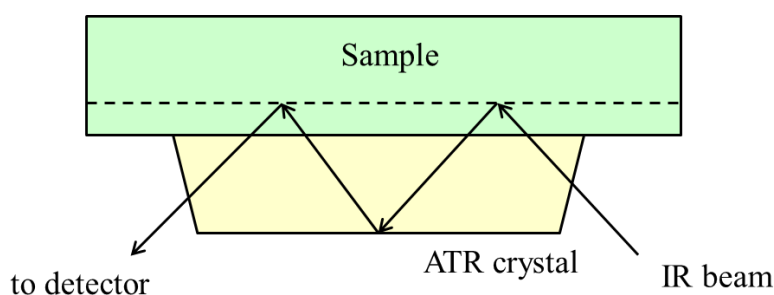


Figure 28. ATR principle.

The infrared beam enters the ATR crystal at an angle of 45° and impinges the sample interface. Because of its wave-like properties, the light is not reflected directly by the surface of a sample but by a virtual layer within the optically less dense sample. The fraction of light reaching into the sample is known as evanescent wave. In the spectral regions where the sample absorbs energy, the evanescent wave is attenuated. After one or several internal reflections, the infrared beam exits the ATR crystal and is directed to the detector.

In the current study FTIR spectroscopy was applied to determine the composition of the polymer composite material and to prove the completeness of the hydrosilylation reaction leading to crosslinking of silicon polymer. FTIR spectra were recorded in ATR mode with Ge crystal, on a Nicolet iS5, Thermo Scientific, collecting 64 scans in the $400\text{-}4000\text{ cm}^{-1}$ range with a resolution of 2 cm^{-1} .

Mössbauer spectroscopy

The technique of Mössbauer spectroscopy is used to examine the valence state of iron and the type of coordination of iron atom (tetrahedral, octahedral, etc.), therefore providing the qualitative and quantitative analysis of iron compounds. It is also used for evaluation of magnetic properties of the iron compounds on the base of hyperfine field effect (see below). The Mössbauer effect consists of the "recoilless" emission of gamma ray photons from certain radioactive nuclei, and the selective

reabsorption of those photons by other nearby nuclei [24, 146]. The process is very sensitive to small difference between the structure of the emitting and absorbing nuclei.

In Mössbauer spectroscopy a solid sample is exposed to a beam of gamma radiation of a source which moves back and forth generating gamma quanta with different energy by the Doppler Effect. The gamma quantum with the energy corresponding to the transition of the absorbing atom from its ground state to the excited state is absorbed in the sample. The detector measures the intensity of the beam transmitted through the sample. The Mössbauer spectrum (MS) represents a plot of percent of transmitted radiation versus the velocity of the source of radiation, given in $\text{mm}\cdot\text{s}^{-1}$. The main parameters of the MS are the isomer shift, I_s , and the quadrupole splitting, Q_s , which can be graphically defined from the spectra as is seen on figure 29. The isomer shift arises if the decaying atom in the source of gamma rays has the different surrounding than the absorbing atom (different chemical or crystal structure) i.e. from the different electron density between the source and the absorber. The quadrupole splitting is due to the shift in nuclear energy levels induced by an electrical field gradient caused by nearby electrons. For the magnetic materials one more parameter is added, the hyperfine splitting or the hyperfine field, B_{hf} . When a magnetic field is present at the nucleolus the Zeeman splitting take place yielding a sextet pattern. The positions of peaks in the sextet and their relative intensities (areas) define the hyperfine field.

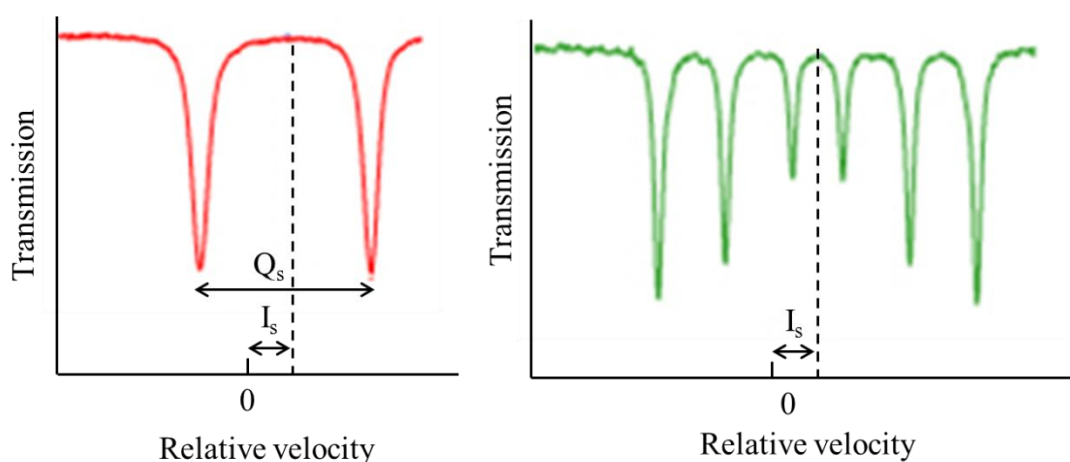


Figure 29. Graphical representation of the MS.

MS of iron oxides consists of sets of peaks (doublets and sextets), and each set corresponds to an iron nucleus in a specific environment in the sample [24]. The nuclear environment depends on a number of factors including the number of electrons (Fe^0 , Fe^{2+} , Fe^{3+}), the number of coordinating anions, the symmetry of the site, and the presence or absence of magnetic ordering (which is temperature-dependent). Between the Curie and Verwey temperatures magnetite is ferrimagnetic and MS can be fitted with two sextets (Figure 30), one corresponding to high spin

Fe^{3+} on the tetrahedral sites, $(\text{Fe}^{3+})_A$, and the other to $\text{Fe}^{2.5+}$ on the octahedral sites, $(\text{Fe}^{2.5+})_B$, as the electron hopping causes the nucleus to sense one average valence.

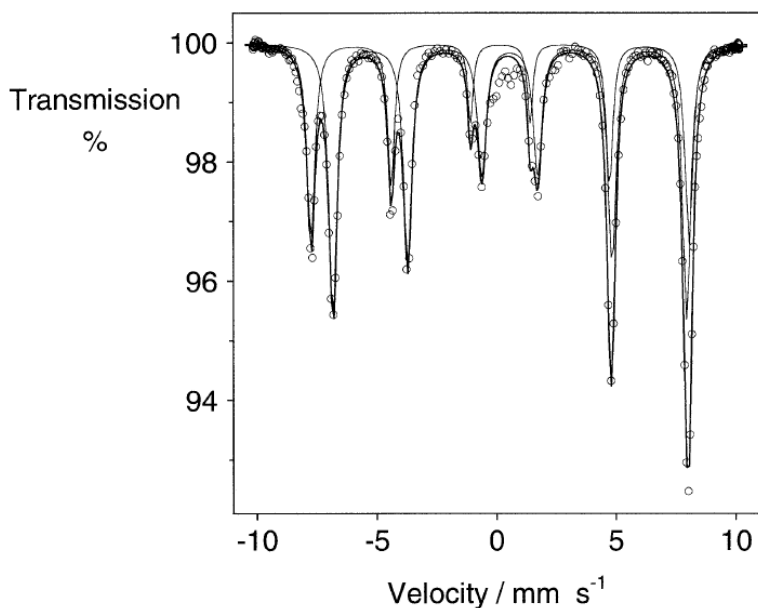


Figure 30. Room temperature spectrum of magnetite fitted with two sextets [24].

In the case of maghemite, Fe^{3+} occupies two different sites in the structure but only one sextet appears at the MS at any temperature as the hyperfine parameters of both A- and B-sites are very similar. Two sextets corresponding to A- and B- sites are hardly distinguishable, especially in well crystalline samples. Nonstoichiometry in the crystal structure, for example in magnetite due to vacancies on the octahedral sites, leads to the increase of the number of sextets [147]. The phase composition is determined on the base of the relative area of sextets or atomic fraction. The hyperfine parameters of MSs of magnetite, nonstoichiometric magnetite and maghemite at room temperature are listed in table 5.

Table 5. Hyperfine parameters for magnetite, nonstoichiometric magnetite and maghemite at room temperature [147]. All quadrupole splittings are close to zero.

Oxide	Valence and site	B_{hf} , T	I_s , $\text{mm}\cdot\text{s}^{-1}$	Area ratio
Fe_3O_4	$(\text{Fe}^{3+})_A$	~ 49.1	0.28	1
	$(\text{Fe}^{2.5+})_B$	~ 46.0	0.66	~ 1.9
$\text{Fe}_{3-x}\text{O}_4$	$(\text{Fe}^{3+})_B$	49.8 – 50.6	0.39	
$\gamma\text{-Fe}_2\text{O}_3$	$(\text{Fe}^{3+})_A$	49.8	0.24	1
	$(\text{Fe}^{3+})_B$	49.8	0.36	~ 1.6

Small particle sizes reduce the B_{hyp} below that of bulk material and broadens the resonance lines. The effect of particle size on MSs is well demonstrated by Goya et al. [148]. The room temperature MSs of iron oxide magnetic nanoparticles displayed the gradual passage from bulk-like to SPM behaviour as the size of nanoparticles decreased from 150 to 48, 11 and 4 nm (Figure 31).

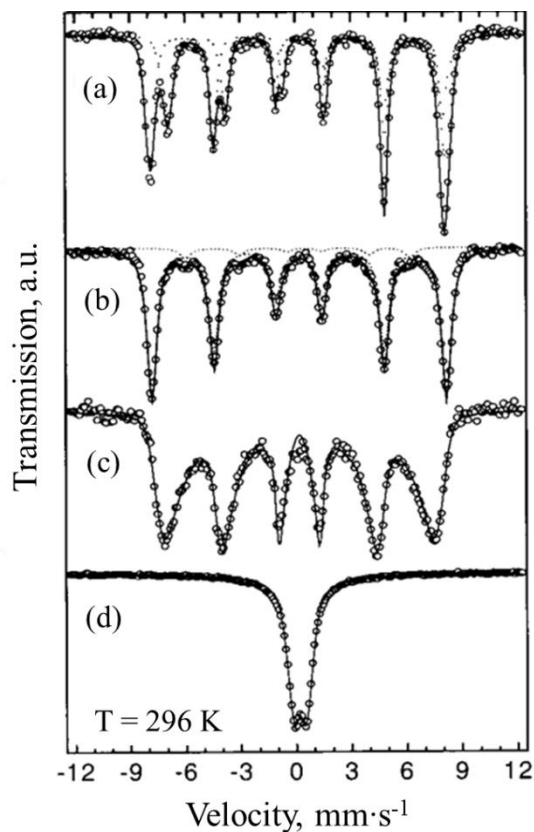


Figure 31. Illustration of particle size effect on room temperature MSs of nanoparticles with size of (a) 150 nm, (b) 48 nm, (c) 11 nm, (d) 4 nm. Adapted from [148].

For 150 nm sample the spectrum is fitted by two sextets with hyperfine fields of 49.5 and 46.0 T, corresponding to $(\text{Fe}^{3+})_{\text{A}}$ and $(\text{Fe}^{2.5+})_{\text{B}}$. As particle size decreases to 47 nm, two components merge into one sextet. For 11 nm sample the effect of thermal relaxation of magnetic moments leads to the line broadening. For sample with 4 nm size only a doublet signal corresponding to SPM state is observed. The same trend in MSs is observed with the change of temperature. SPM doublet observed at room temperature transforms to well resolved sextet at temperature below the Curie temperature.

Thermal fluctuations in SD nanoparticles leading to the broadening of spectral lines and their superposition make it difficult to analyse the phase composition. However, Mössbauer spectroscopy provides unambiguous information about magnetic ordering in nanoparticles (SPM or ferromagnetic).

In the current work the ^{57}Fe transmission Mössbauer spectra (MSs) of samples were recorded using a standard Mössbauer spectrometer in a constant acceleration mode with the ^{57}Co (Rh) gamma-ray source. The isomer shift values were related to α -Fe metal at room temperature. The MSs were measured in zero field in the temperature interval 5 – 293 K.

2.2.3. Magnetic properties

Magnetostatic properties

The main magnetostatic parameters M_S , M_R , H_C are determined from magnetization curves (see section 1.1.1., figure 6) measured on Vibrating Sample Magnetometer (VSM) at static magnetic fields with a strength of up to 10 kOe. The samples can be measured in the form of powders, solids (toroids) and liquids. In a typical measurement a sample is placed between two electromagnets where a uniform magnetic field is generated (Figure 32). The sample is then physically vibrated sinusoidally. The pickup coils registrate the induced voltage which is proportional to the sample's magnetic moment, but does not depend on the strength of the applied magnetic field. By changing the strength of an external electromagnetic field it is possible to obtain the hysteresis curve of a material.

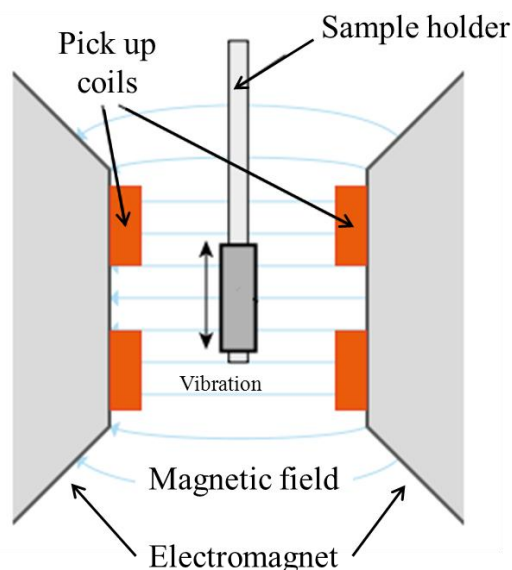


Figure 32. Schematic representation of measuring mechanism in Vibrating Sample Magnetometer.

According to the shape of magnetization curve it is possible to make a preliminary conclusion on the magnetic state of material under investigation. The magnetization curve for material with MD structure is characterized with a hysteresis loop, and saturation of magnetization in the fields utilized in the measurements. Materials with SD structure, both SPM and SSD nanoparticles, are not saturated in applied fields due to the increase of effective anisotropy as a result

of spin disorder on the surface of nanoparticles. SPM nanoparticles demonstrate no hysteresis and remanence. The interaction between SPM nanoparticles lead to the increase of effective magnetic anisotropy and non-zero hysteresis arises. SSD nanoparticles have a non-zero coercivity and remanent magnetization, lower to that of bulk material.

In the current study the magnetostatic properties of iron oxide nanoparticles in a powder form were performed on the vibrating sample magnetometer (VSM; Lake Shore 7407) at room temperature in air atmosphere in a magnetic field of up to 10 kOe.

Temperature dependence of magnetization is measured in a special kind of magnetometer called superconducting quantum interference device (SQUID). The sample in a powder form is cooled down to 4 – 50 K in liquid helium or nitrogen either in the presence of external magnetic field, field-cooled (FC) measurement, or without application of the field, zero-field-cooled (ZFC) measurement. The magnetization is recorded versus temperature. The ZFC magnetisation curve is recorded by measuring the magnetisation during a stepwise increase of temperature. The FC magnetisation curve is obtained by measuring magnetization at a stepwise decreasing temperature. This measurement allows to estimate the blocking temperature, T_B , for the magnetic nanoparticles. Experimentally, T_B is determined either as a maximum on the ZFC curve, T_{max} , or as a point at which the ZFC and FC curves diverge, the so-called irreversibility point, T_{ir} (Figure 33)[149]. Since nanoparticles are usually characterized by size and shape dispersion, two characteristic temperatures, T_{max} and T_{ir} are usually observed on the experimental curves. Therefore, one usually identifies T_{max} with T_B of smaller particles and T_{ir} with T_B of particles with maximum size [150].

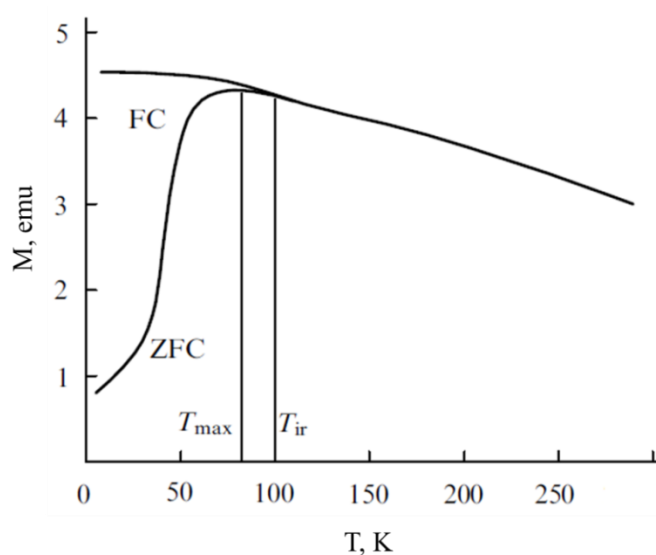


Figure 33. Temperature dependence of magnetic moment: FC and ZFC curves. Adapted from [150].

The experimentally obtained FC/ZFC curves for non-interacting iron oxide nanoparticles with the size of 3, 5 and 10 nm are represented on figure 34. As it is seen from the figure, with an increase of particle size the T_B increases up to 330 K and 360 K, indicating the room temperature ferromagnetism of larger nanoparticles [151].

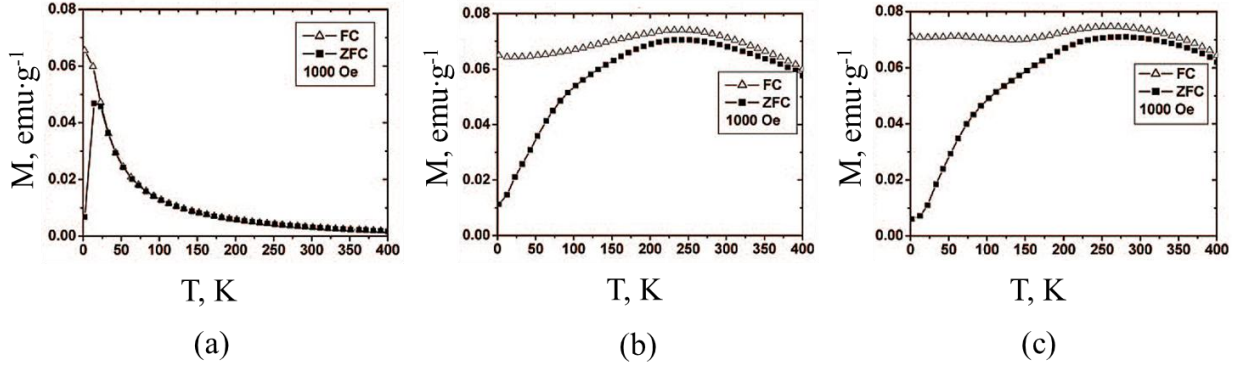


Figure 34. FC and ZFC curves for non-interacting nanoparticles with sizes of (a) 3 nm, (b) 5 nm, (c) 10 nm. Adapted from [151].

However, the characteristic temperatures, T_{max} and T_{ir} strongly depend on the rate of cooling and heating and on the interparticle interactions. Usually, the interparticle interactions broaden the peak on ZFC curve, thus the estimation of T_B becomes impossible.

ZFC and FC temperature dependent magnetization measurements of iron oxide nanoparticle prepared in the current work were performed with a SQUID magnetometer Quantum Design MPMS XL-7. Magnetization measurements were carried out in the temperature range of 50 – 300 K at magnetic fields of 50, 100, 500 and 1000 Oe.

Dynamic magnetization properties

In AC magnetic fields, ferromagnetic materials exhibit irreversible magnetization processes resulting in power loss which may be expressed in terms of the phase lag between impressed field \mathbf{H} and induction \mathbf{B} change (Figure 35). Such a lag is described by a complex magnetic permeability and magnetic loss tangent:

$$\mu = \mu' - i\mu'' , \quad \tan \delta = \frac{\mu''}{\mu'} , \quad (23)$$

where δ is the phase angle between \mathbf{B} and \mathbf{H} . The real part of complex magnetic permeability, μ' , determines that part of \mathbf{B} , which varies in-phase with the \mathbf{H} . The imaginary part of complex magnetic permeability, μ'' , expresses the component of \mathbf{B} which is delayed by the phase angle 90° from \mathbf{H} .

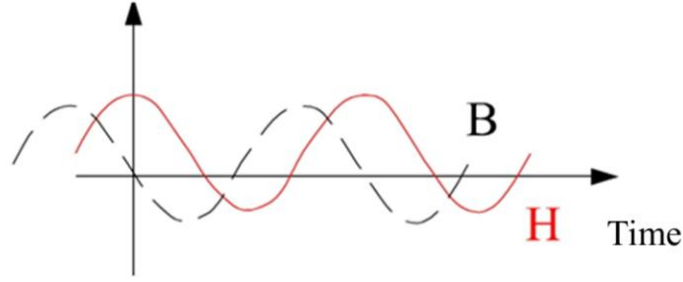


Figure 35. Response of magnetic material in AC field: the induction, **B**, lags in phase behind the applied field, **H**.

Extensive information can be obtained from the magnetic spectra (frequency dependence of μ) of materials with various compositions. Usually four regions of permeability dispersion are distinguished on magnetic spectra: low-frequency region (0 – 1 MHz), RF region (1 – 1000 MHz), superhigh-frequency region (10^3 – 10^5 MHz), and infrared region (frequencies of about 10^7 MHz) [1, 5]. Most of the publications on the magnetic spectra are devoted to the study of RF and superhigh-frequency (microwave) regions of permeability dispersion of ferrites, which is motivated by their application in radio-electronics. The RF dispersion of μ in ferrites is associated with the domain wall motion, i.e. the magnetic moments within the domain wall rotate as the wall moves to a new position. In this region, the dispersion curve may have either a relaxational or resonance character. The superhigh-frequency dispersion of μ is associated with a natural ferromagnetic resonance (NFR), also called the gyromagnetic spin resonance [2]. In nanoscale magnetic materials with SD structure, complex permeability dispersion is usually associated only with NFR [152].

To measure the complex permeability of a magnetic materials in the RF range one usually applies the inductance method with an RF Impedance Material Analyzer [153]. The measurements are performed on toroidal-shaped samples.

In order to determine the contributions of the domain wall resonance and the NFR to the complex magnetic permeability, the experimental magnetic spectrum is approximated by the frequency dispersion formula [154]:

$$\mu = 1 + \chi_{dw} + \chi_s = 1 + \frac{f_d^2 \chi_{d0}}{f_d^2 - f^2 + if\beta} + \frac{\chi_s + if\alpha}{\chi_s - f^2}, \quad (24)$$

where χ_{dw} and χ_s are the magnetic susceptibilities due to domain wall motion and spin (magnetic moment) rotation, respectively, f_d and f_s are the resonance frequencies of the domain wall and spin components, χ_{d0} and χ_{s0} are the static magnetic susceptibilities of each component, β and α are the damping factors of the domain wall motion and spin rotation, and f is the electromagnetic field frequency. The dispersion parameters (f_d , f_s , χ_{d0} , χ_{s0} , β and α) are determined from fitting the experimental magnetic spectra by a nonlinear least-squares method.

The frequency dependence of the complex magnetic permeability of the materials obtained was studied by the impedance method in the frequency range from 1 MHz to 3 GHz by an Agilent E4991A Impedance/Material Analyzer. In order to measure the magnetic spectra, magnetic particles were mixed with polyvinyl alcohol in a weight ratio of 3:1, respectively, dried and then compressed at 200 MPa into toroids with an inner diameter of 3.1 mm and an outer diameter of 8 mm.

2.2.4. Heating efficiency

The heat generation by iron oxide nanoparticles exposed to AC magnetic field is studied by calorimetric measurements. Figure 36 represents a scheme of measuring system. In the current study a home-made measuring system was used. It consisted of a signal generator (Agilent 33521A), RF broadband amplifier (AR RF/Microwave Instrumentation 800A3A), induction coil (90 mm diameter), interchangeable capacitors and measuring units for temperature and magnetic field sensing. The measurements were carried out at AC magnetic fields with frequencies of 114, 525, 1048 kHz and amplitudes of 5.9, 7.6, 13.8 kA·m⁻¹, approved for application in MH. The test tube with a sample in the form of a dispersion of iron oxide magnetic nanoparticles (2, 5, 7 wt. %) in glycerol or composite with different concentration of nanoparticles (2, 5, 7 wt. %) was inserted into a solenoid coil with an AC magnetic field. The glycerol dispersions of nanoparticles were prepared with ultrasonic homogenizer Sonoplus HD 2070. Before each measurement the samples were thermostatted at 25 °C in a water bath. The temperature was measured with optical hot spot module (Qualitrol TGL 589A) and fibre optic temperature sensor (T1S-03-PT06) inserted directly inside the sample.

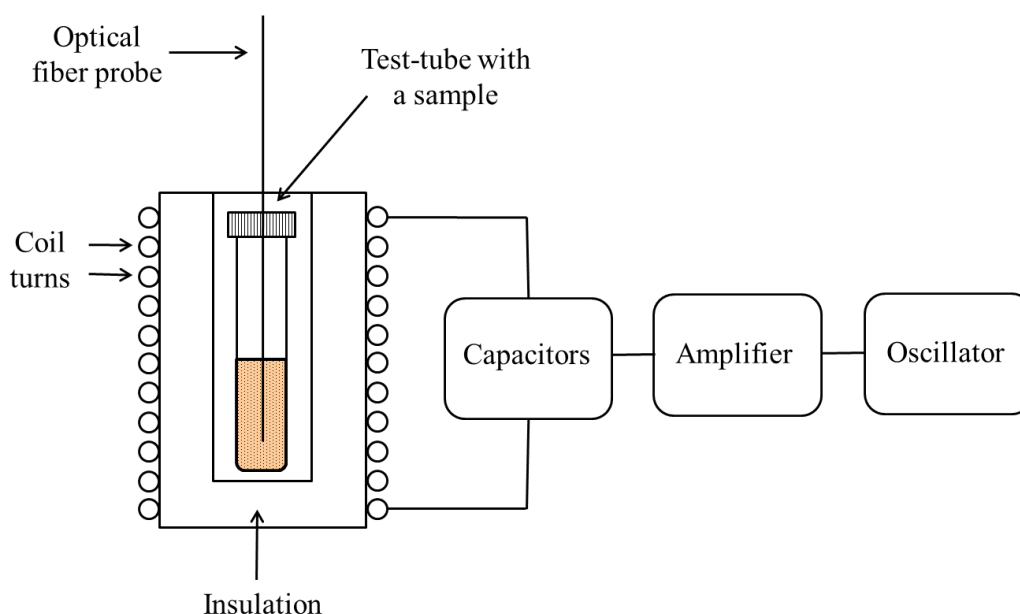


Figure 36. Schematic representation of measuring system.

The SLP was calculated according to the equation (18) (Section 1.4.2.). The SLP was measured in Watts per gram of iron in magnetic material ($\text{W}\cdot\text{g}_{\text{Fe}}^{-1}$). The total iron content was determined by EDXRF. Because the experimental setup is not perfectly adiabatic, the value of $\frac{dT}{dt}$ was determined from the initial slope of the temperature rise obtained from the linear term of a polynomial fit to the whole curve. The heat capacity of dispersion or composite of n -components is calculated as follows:

$$C = \sum_{i=1}^n x_i m_i, \quad (25)$$

where c_i ($\text{J}\cdot\text{g}^{-1}\cdot\text{K}^{-1}$) is the specific heat capacity and m_i (g) is the mass of the i -th component. As the dispersion consisted of two components, i.e. glycerol and iron oxide nanoparticles, the specific heat capacities of these substances were used (Table 6). For iron oxide nanoparticles, the specific heat capacity of magnetite, $c_{\text{magnetite}} = 0.5 \text{ J}\cdot\text{g}^{-1}\cdot\text{K}^{-1}$, was taken.

Table 6. Specific heat capacities and viscosities of commonly applied in hyperthermia dispersion mediums and of living matters.

Substance	$c_i, \text{J}\cdot\text{g}^{-1}\cdot\text{K}^{-1}$	η at 20 – 50 °C, Pa·s
Glycerol	2.434	1.41 – 0.142
Water	4.18	0.001 – 0.0005
Silicone	1.05 – 1.30	13.0 – 28.0
Blood	3.6 – 3.7	~ 0.005
Soft tissues	3.36	-
Fat tissues	2.3	-

Properties of dispersion medium influence much the heat generation. Specific heat capacity determines the heat distribution, i.e. low heat capacity facilitates the heat distribution. Viscosity of the medium influences the relaxation of magnetic moments of nanoparticles. It was established that at viscosities higher than 0.01 Pa·s, the Brown relaxation is suppressed and the heat is solely determined by Néel relaxation [15]. Response of nanoparticles to AC magnetic field is usually studied on water dispersions of nanoparticles, as the viscosity of water is much low then that of the living tissues and blood (Table 6). The results of these measurements are of a little interest. In the current study the SLP of nanoparticles dispersed in glycerol and silicon elastomer was studied. The same heat output is expected to be generated *in-vivo*.

2.2.5. Kinetics of polymer crosslinking

In the current study the composite material on the base of silicon elastomer and magnetic iron oxide nanoparticles was studied with a view of its application in AEH. Additional requirements are imposed on the mediator for AEH, besides the general requirements in MH (see Section 1.4.2). Of particular importance are rheological properties of the mediator: viscosity before injection into the blood vessel and after the curing process and the kinetics of polymer crosslinking.

The kinetics of composite formation in the current study was followed by rheological measurements performed on a Bohlin CVOR 150 rheometer using parallel plate geometry PP25 in oscillation mode. Right after mixing of the components of the composite (Vessel A and Vessel B) 0.15 ml of the obtained liquid was placed on the bottom plate of the geometry. The gap size between two plates was set to 300 μm . The rheological measurements were performed at 38 $^{\circ}\text{C}$, which corresponds to the average internal human body temperature. The composite was subjected to oscillation at a fixed frequency, $\omega = 0.1$ Hz, and fixed maximum strain, $\gamma_M = 0.005$. The response signal, stress wave, different in phase and amplitude from strain wave, was monitored. A phase difference, δ , is a measure of the viscous/elastic ratio for the material at frequency ω . The elastic (in-phase) and viscous (out-of-phase) components of the stress wave are separated by the software correlation analysis. The complex shear modulus is defined as [155]:

$$G^* = \frac{\tau^*}{\gamma_M} = \sqrt{G'^2 + G''^2}, \quad (26)$$

where τ^* is the complex stress, G' is real part, elastic modulus (in-phase), G'' is imaginary part, viscous modulus (out-of-phase). The complex viscosity, η^* , is equal to G^*/ω , and $\tan \delta$ is the ratio of G''/G' .

2.2.6. X-ray contrast measurements

X-rays with photon energy of 18 – 150 keV are used in diagnostic imaging [156]. The radiopacity of the composite was tested with Compact X-ray microtomograph, SkyScan 1174v2. The X-ray photographs were recorded at 50 kV of the X-ray tube, exposition 10000 ms. A 1.5-mm-thick aluminium plate of was placed before the samples as a body mimic. The X-ray photographs were analysed with ImageJ processing program, where the intensity histograms of the greyscale images were determined. The histograms range from 0 to 255, where 0 stands for black (zero intensity) and 255 for white colour (maximum intensity). Every image was characterized by the histogram mean value, which defines the balance between the bright and dark areas of a given sample.

CHAPTER 3. RESULTS AND DISCUSSION

3.1. Preparation of magnetic iron oxide nanoparticles for magnetic hyperthermia

Analysis of the literature has shown that the amount of heat generated by magnetic nanoparticles strongly depends on the nanoparticle's magnetic properties which in turn are connected with their structural properties. Particles in order to be used in MH have to display uniformity, phase purity, high crystallinity, size corresponding to a SSD state, high saturation magnetization and in particular high anisotropy energy. The first part of work was devoted to the preparation of magnetic iron oxide nanoparticles with this set of properties by coprecipitation method.

To solve the task, following investigations have been carried out:

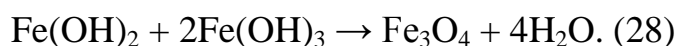
- (1) At first, the synthesis conditions for preparation of iron oxide nanoparticles with reproducible structural properties (shape, size and composition) were determined.
- (2) The correlation between synthesis parameters and magneto-structural properties of nanoparticles was established and explained through mechanism of nucleation and growth.
- (3) The effect of post treatment by annealing at elevated temperatures on structural and magnetic properties of nanoparticles was studied.
- (4) The heating potential of nanoparticles in viscous medium was analyzed in AC magnetic fields with frequencies and amplitudes allowed for MH.
- (5) The heat output of nanoparticles dispersions in AC magnetic field was explained by combined effect of magnetic interparticle interactions and specific properties of carrier medium (viscosity and heat capacity).

The detail explanation of work done is given below.

3.1.1. Synthesis conditions effect on magneto-structural properties of nanoparticles and heating efficiency in AC magnetic fields

Since the first reports of coprecipitation synthesis of iron oxide nanoparticles by Massart in 1981 [38], a large number of studies on the influence of reaction parameters on the properties of nanoparticles appeared. These main parameters influencing the magneto-structural properties of iron oxide nanoparticles are: iron (II) to iron (III) molar ratio; the type of the precipitant; pH of the reaction medium; reaction temperature; presence of surfactants; reagents addition rate; agitation, etc. [40, 157-159]. However, only little attention is given to the study of the mechanisms of nucleation and growth of magnetite from solution, although these mechanisms are of considerable importance for the optimization of morphological, crystallographic, and magnetic characteristics of nanoparticles.

The production of iron oxide by coprecipitation method is usually described by the following reactions:



This is a simplified representation of the magnetite production process. In [157, 160, 161], the authors have shown that magnetite is formed as a product in the conversion of iron oxyhydroxides, rather than by a direct reaction between Fe^{2+} and Fe^{3+} cations in an aqueous medium. In this work the impact of coprecipitation reaction course on the mechanism of magnetite nanoparticle formation is demonstrated, which determines the magneto-structural properties and the heating efficiency of nanoparticles in AC magnetic fields.

Influence of the reaction course on morphology and crystalline structure of nanoparticles

Iron oxide magnetic nanoparticles were obtained by two different coprecipitation reaction routes. In the first case, an alkali solution was added dropwise to a solution of ferrous and ferric salts (Sample I), so that the pH of the reaction medium was continuously changed from acidic to alkaline (Figure 37). In the second case, a solution of salts is added to an alkali solution (Sample II); therefore, the pH of the reaction mixture stayed alkaline. The results of SEM, TEM and HRTEM revealed that nanoparticles formed in the first route differ in shape and size and have a broad size distribution (Figures 38 a, b, c; Figure 39 a). In contrast to Sample I, the second reaction leads to the formation of almost spherical nanoparticles with a narrow size distribution obeying a log-normal distribution (Figures 38 d, e, f; Figure 39 b). The average particle size (d_{TEM}) calculated from TEM and HRTEM images are 22 nm for Sample I and 13 nm for Sample II. The polydispersity index (σ_{TEM}) for Sample II is 0.3. The HRSEM and TEM images also show that the particles of both samples are partly incorporated into aggregates.

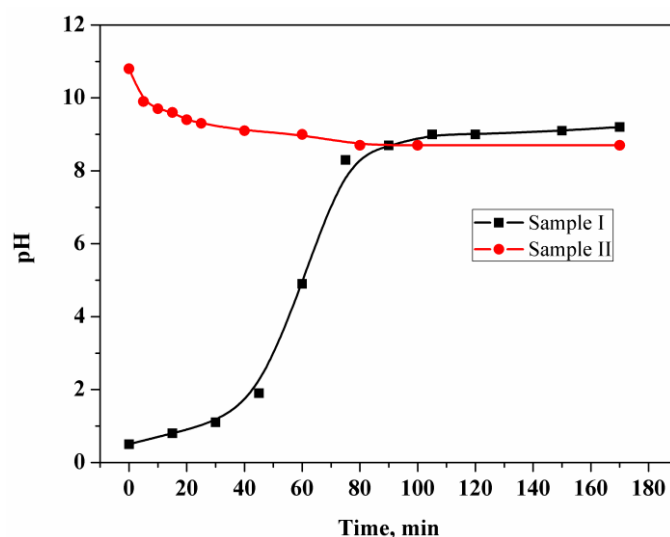


Figure 37. Variation of pH in the reaction medium during coprecipitation.

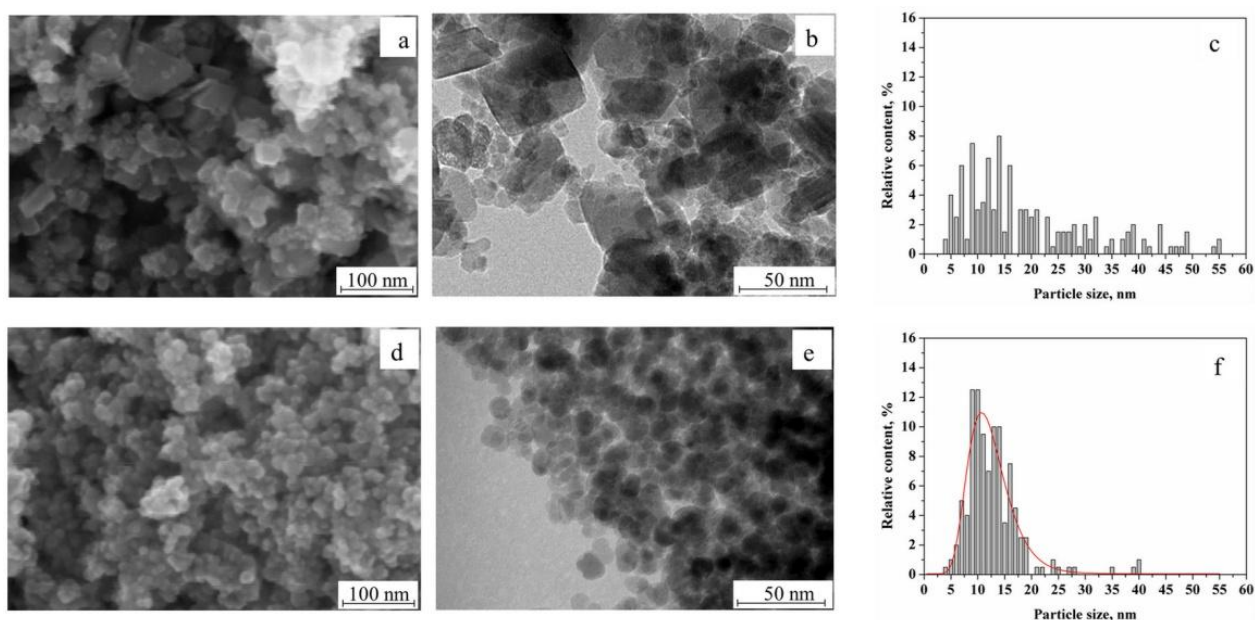


Figure 38. Microscopy of samples. Sample I: (a) – HRSEM, (b) – TEM, (c) – particle size distribution. Sample II: (d) – SEM, (e) – TEM, (f) – particle size distribution.

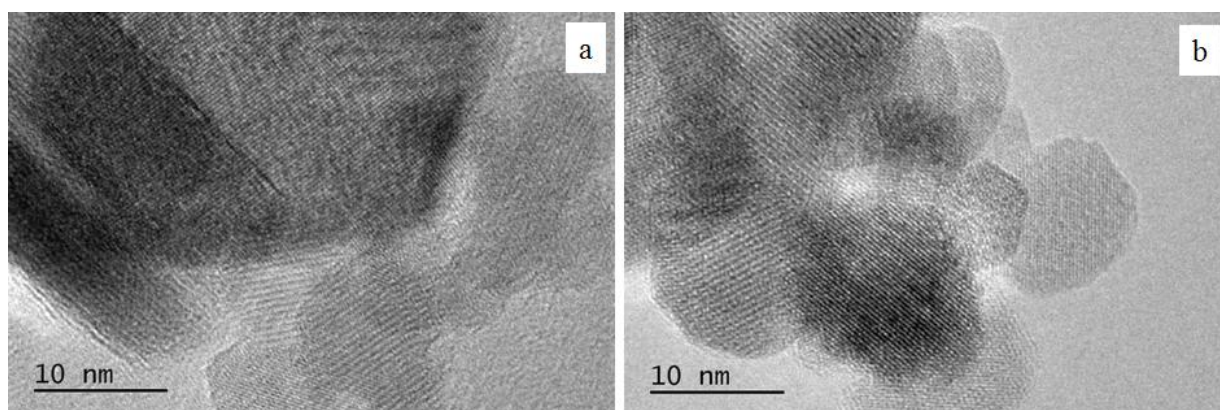


Figure 39. HRTEM of nanoparticles of (a) Sample I and (b) Sample II.

The XRD pattern of both samples exhibits eight lattice planes (111), (220), (311), (222), (400), (422), (511), and (440) corresponding to the cubic spinel structure of magnetite phase, while the two remarkable lattice planes (210) and (213) correspond to the tetragonal structure of maghemite phase (Figure 40). The XRD data refinement has been done using $Fd3m$ space group for magnetite phase and $P4_12_12$ space group for maghemite phase. It is established that Sample I comprises 48 % of magnetite and 52 % of maghemite phase, whereas Sample II contains 72 % of magnetite and 28 % of maghemite. This mixed phase composition of nanoparticles is consistent with previously reported results for iron oxide nanoparticles obtained by coprecipitation method [40, 158]. The crystal lattice strain (ϵ) evaluated by the Rietveld method for Sample I ($\epsilon \sim 0.8 - 1.7$ %) is higher than for Sample II ($\epsilon = 0.3$ %). Structural parameters like crystallite size, lattice constants, phase formation, and crystal lattice strain of the samples determined from XRD pattern analysis are listed in Table 7. This table also shows the average particle size and the polydispersity index obtained from TEM data. According to the particle sizes calculated from TEM and XRD data, Sample I consists of SD and MD nanoparticles, while nanoparticles of Sample II are SPM.

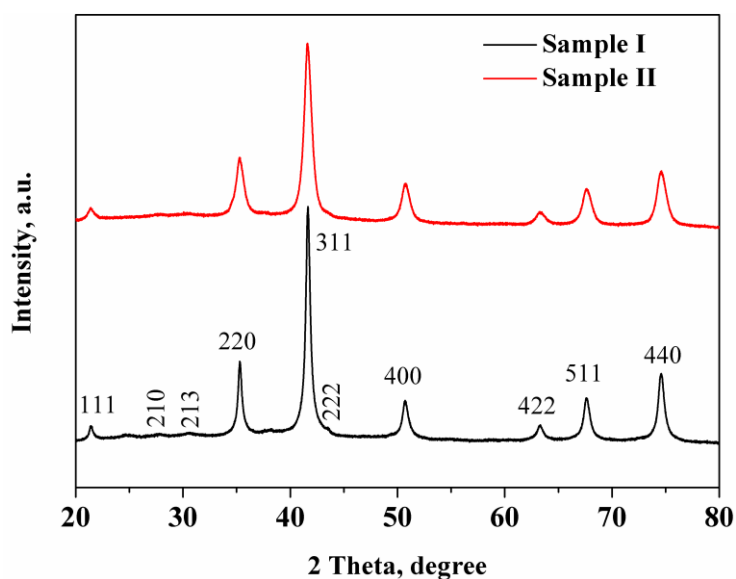


Figure 40. XRD patterns of samples obtained by two different coprecipitation reaction courses.

Table 7. Structural and magnetic properties of obtained iron oxides nanoparticles, and bulk magnetite and maghemite reported in [24, 162].

Property	Sample I	Sample II	Bulk Fe ₃ O ₄	Bulk γ -Fe ₂ O ₃
d_{TEM} , (nm)	22	13	-	-
σ_{TEM}	polydispersed	0.3	-	-
$d_{\text{XRD}} \pm 0.5$, (nm)	12	12	-	-
$a \pm 0.0004$, (Å)	Magnetite $a=8.3444$	$a=8.3584$	$a=8.3960$	-
	Maghemite $a=b=8.3441,$ $c=25.0375$	$a=b=8.3465,$ $c=25.0173$	-	$a=b=8.3470,$ $c=25.0100$
Magnetite content $\pm 3\%$, (%)	48	72	100	-
M_s , (emu·g ⁻¹)	63 ± 4	56 ± 2	92-100	60-82
M_r , (emu·g ⁻¹)	6 ± 2	0.8 ± 0.2	-	-
H_c , (Oe)	61 ± 26	11 ± 4	-	-
ε , (%)	0.8 – 1.7	0.3	-	-
f_r , (Hz)	1.5×10^9	2×10^9	10^6	-
μ' at 10^7 Hz .	5	3.5	5000	-

Influence of the reaction course on magnetic properties of nanoparticles

Figure 41 shows the magnetization curves of both samples measured in the form of powders. The value of M_s for both samples are lower than those of bulk magnetite ($92\text{--}100\text{ emu}\cdot\text{g}^{-1}$ [24]) and maghemite ($60\text{--}82\text{ emu}\cdot\text{g}^{-1}$ [24]) and agree with those reported for iron oxide nanoparticles produced by the coprecipitation method (Table 7) [40, 150]. The lower values of M_s for iron oxide nanoparticles are primarily associated with a finite size effect caused by a strong disorder of spins on the surface [163]. The M_s of Sample I is reached in fields of the order of 7 kOe, whereas Sample II is not saturated even at 10 kOe (Figure 41, Insert b). The average values of M_s , M_r , and H_c for Sample I are higher than those for Sample II (Table 7). However, the standard deviations of these values for Sample I are several times higher than for Sample II. The magnetization curve of Sample I exhibits ferromagnetic behaviour: the sample is generally magnetized up to saturation and demonstrates visible coercivity and remanent magnetization. On the contrary, Sample II is not saturated even in a magnetic field of 10 kOe and is characterized by low coercivity and almost zero remanent magnetization.

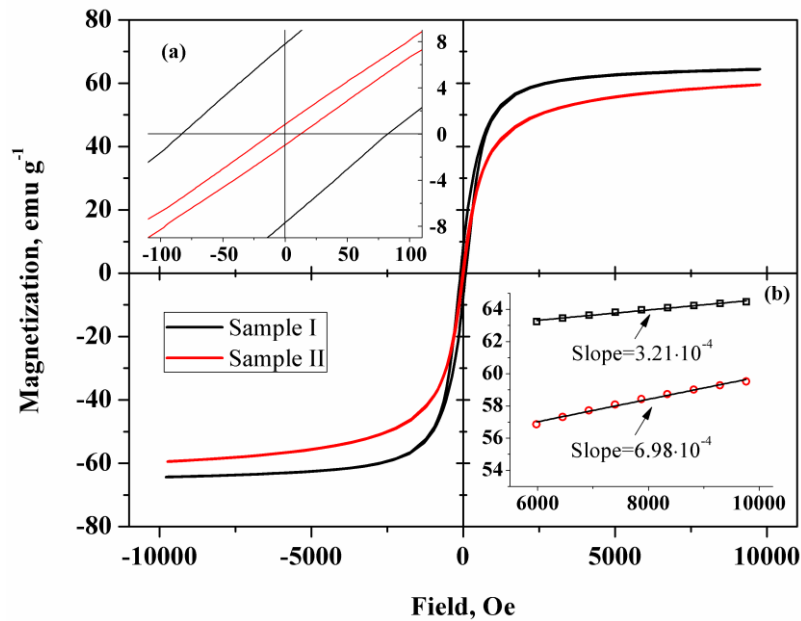


Figure 41. Magnetization curves for Sample I and Sample II. Insets: (a) magnetization at low magnetic fields, (b) magnetization at high magnetic fields.

Figure 42 shows the frequency dependence of the complex magnetic permeability of Sample I and Sample II (magnetic spectra) in the radio-frequency band. Compared with the magnetic spectra of bulk magnetite (Figure 42 a) [162], the complex permeability dispersion region in samples of nanoparticles is shifted to the high-frequency part of the radio-frequency band (Figure 42 b, c). Moreover, bulk magnetite shows a relaxation type of magnetic dispersion and a broad magnetic loss peak, whereas samples of magnetic nanoparticles demonstrate a mixed relaxation resonance type of magnetic dispersion and a narrow magnetic loss peak. The

approximation of magnetic spectra by the frequency dispersion formula [154], allowing to evaluate the relative contributions of domain-wall motion, **dw**, and magnetization rotation, **mr**, to the complex magnetic permeability, demonstrates the following results. Magnetization processes in bulk magnetite that occur in the low-frequency part of the radio-frequency band (10^6 – 10^8 Hz) are primarily attributed to the **dw** motion; however, **mr** replaces **dw** motion at higher frequencies. The magnetic spectra of the samples reveal the contribution of two magnetization processes, **dw** motion and **mr**, to μ . The difference between the samples is that the contribution of **dw** motion to μ in Sample I is almost equal to that of **mr** (Figure 42 b), whereas, in Sample II, the contribution of **dw** motion is negligible (Figure 42 c). This fact indicates that Sample I is apparently in a MD state, while the magnetization process in Sample II is mainly determined by **mr**, which confirms the rotational mobility of magnetic moments in individual SD particles.

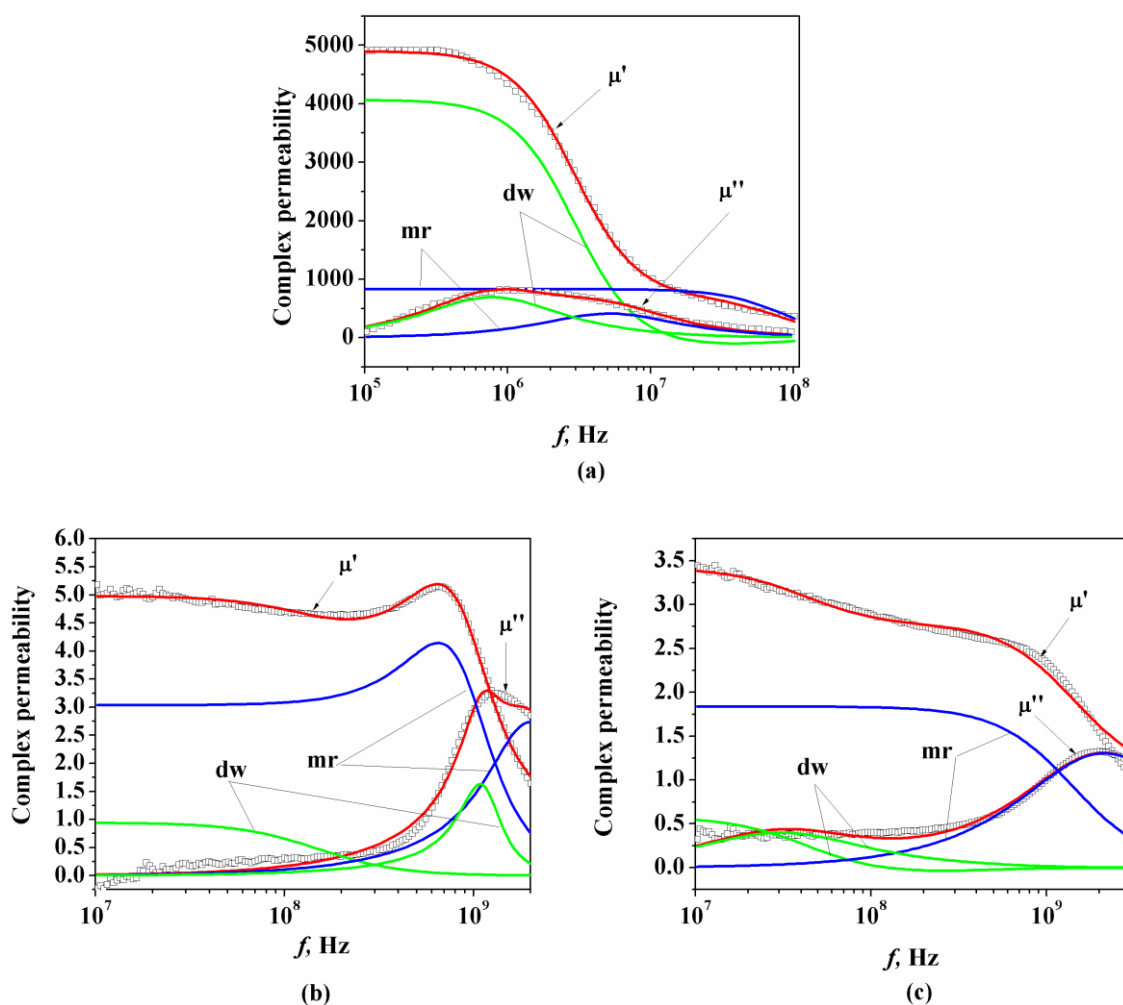


Figure 42. Complex permeability spectra of (a) bulk magnetite and of obtained nanoparticles: (b) Sample I, (c) Sample II. The experimental values of μ' and μ'' are indicated by open squares. The colored solid lines show the total calculated permeability (red) obtained by combining the domain-wall motion (green) and magnetization rotation (blue) components.

Correlation between magneto-structural properties of iron oxide nanoparticles and their heating efficiency in AC magnetic field

The thermal response of magnetic nanoparticles of Sample I and Sample II dispersed in glycerol (2 wt. %) was studied by calorimetric measurements at different frequencies (114 kHz, 525 kHz and 1048 kHz) and amplitudes ($5.9 \text{ kA}\cdot\text{m}^{-1}$, $7.6 \text{ kA}\cdot\text{m}^{-1}$ and $13.8 \text{ kA}\cdot\text{m}^{-1}$) of an AC magnetic field. The temperature evolution curves for both samples at different AC magnetic field parameters are presented in figure 43. The calculated values of SLP are listed in Table 8. The samples studied display dramatically different heating efficiency due to the significant difference between their magneto-structural properties. According to the results obtained the temperature of Sample II dispersion increases from $37 \text{ }^\circ\text{C}$ to the hyperthermia temperatures ($42 \text{ }^\circ\text{C} - 45 \text{ }^\circ\text{C}$) in tens of seconds; the value of SLP increases with the frequency and the field intensity. Contrariwise, Sample I is not heated to the desired temperatures at any of the applied AC magnetic field fields. Note that the dispersion of Sample II exhibits different heating rates depending on the amplitude and frequency of the field. At a low frequency (114 kHz), high amplitude ($13.8 \text{ kA}\cdot\text{m}^{-1}$) is needed to achieve fast heating, whereas, at higher frequencies, fast heating is achieved even for moderate amplitudes ($5.9 \text{ kA}\cdot\text{m}^{-1}$, $7.6 \text{ kA}\cdot\text{m}^{-1}$).

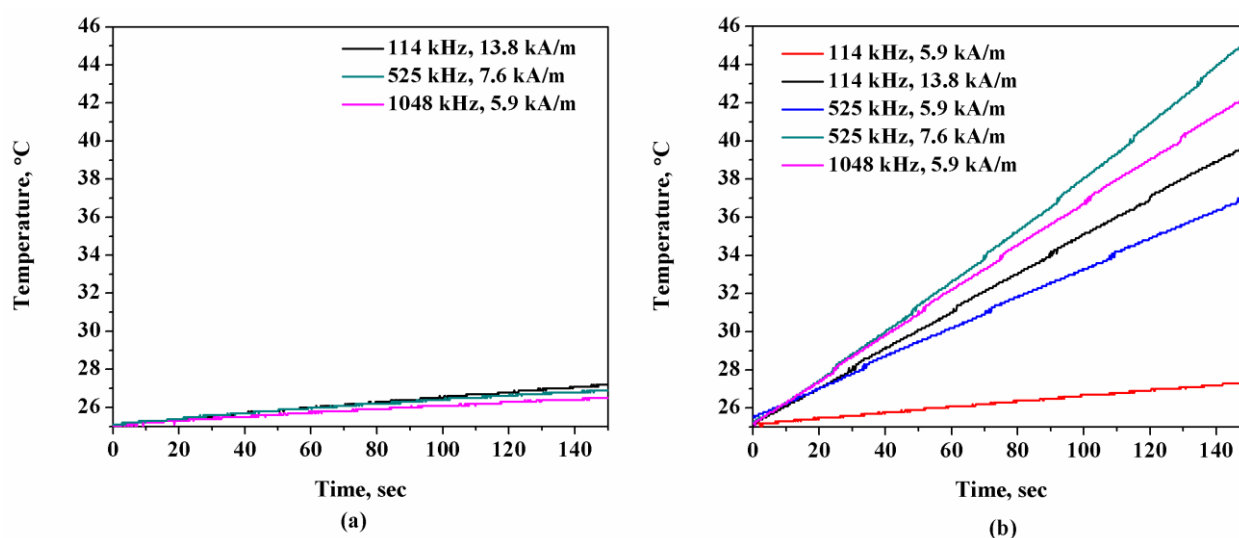


Figure 43. Heating rate of (a) Sample I and (b) Sample II dispersed in glycerol (2 wt. % of nanoparticles) for given frequency and amplitude of AC magnetic field.

Table 8. SLP of Sample I and Sample II dispersed in glycerol (2 wt. % of nanoparticles).

AC magnetic field		SLP, W·g ⁻¹	
Frequency, kHz	Amplitude, kA·m ⁻¹	Sample I	Sample II
114	5.9	0	1.3 ± 0.2
	13.8	1.5	14.1 ± 0.1
525	5.9	0	10.2 ± 1.3
	7.6	0.51	18.0 ± 2.1
1048	5.9	0.71	16.9 ± 0.4

The primary mechanism leading to the variation of SLP of nanoparticles is the variation of the energy barrier of magnetization reversal. This effect might be expected to strongly depend on the particle shape and size and the magnetic anisotropy. For Sample I, low heating efficiency is a result of nanoparticles polydispersity (variation of particle size, shape, and anisotropy), which leads to a broad distribution of energy barriers. The relatively high heating potential of Sample II is determined by its narrow particle size distribution and interparticle interactions. Thus, the heating ability of nanoparticles is attributed to their structural and magnetic properties. These properties, in their turn, are determined by the nucleation and nanoparticle growth processes in a coprecipitation reaction.

3.1.2. Influence of synthesis parameters on nucleation and growth of iron oxide nanoparticles in solution

The observed difference in nanoparticles properties obtained by the same synthesis protocol but with different reagent addition order is due to difference in nucleation and growth mechanisms. Figure 44 illustrates the course of coprecipitation reaction of ferrous and ferric salts when an alkali solution is added to a solution of salts so that the pH of the reaction medium changes continuously from acidic to basic (synthesis of Sample I). In [160], it was established that, at the initial stage of the reaction when the pH of the reaction medium is about 1 – 2, a hydrolysis of Fe³⁺ salt occurs, which produces akageneite (β -FeOOH). An increase in the pH of the reaction medium induces the conversion of akageneite into goethite (α -FeOOH) and then into hematite (α -Fe₂O₃). The formation of magnetite with spinel structure occurs for pH > 5. The conversion of iron oxyhydroxides into hematite and magnetite is catalysed by Fe²⁺ cations, because the electron exchange between Fe²⁺ and Fe³⁺ plays the dominant role in the crystallization of magnetite.

The continuous change in the colour of the reaction mixture from transparent to yellow, brown, and finally to black was observed in the reaction with Sample I, confirming the above discussed transformations.

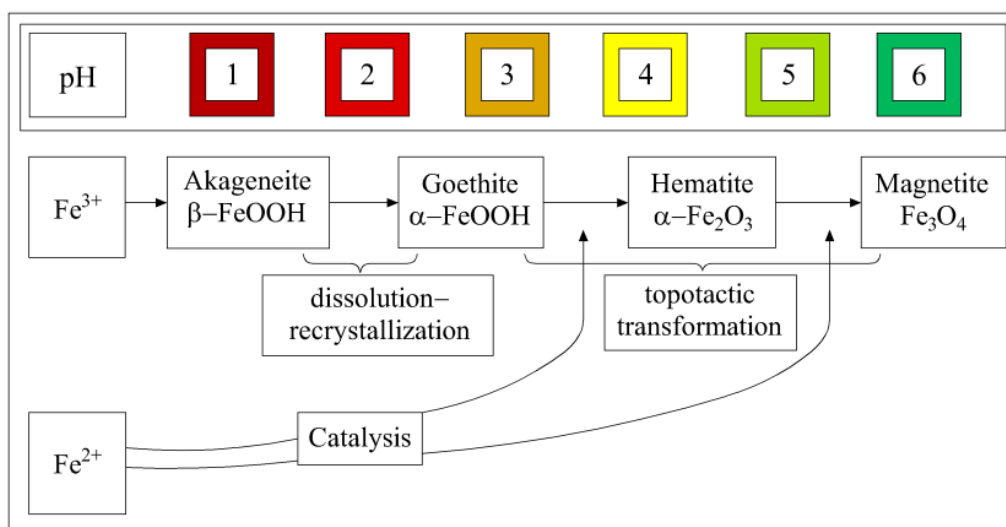


Figure 44. Coprecipitation reaction course: alkali solution is added to the salts solution. Modified from [160].

Nevertheless, this is not the only mechanism by which magnetite is formed in the coprecipitation reaction when an alkali solution is added to a solution of salts. Here a competitive process occurs, which also produces magnetite (Figure 45). This fact is attributed to the inhomogeneity of pH in the reaction medium, namely, to the presence of regions with high values of pH $\sim 6 - 7$ in which ferrous hydroxide, $\text{Fe}(\text{OH})_2$, is formed. Under stirring the reaction mixture, the pH in these regions decreases and ferrous hydroxide is oxidized to lepidocrocite ($\gamma\text{-FeOOH}$), which afterwards transforms into magnetite in a topotactic process.

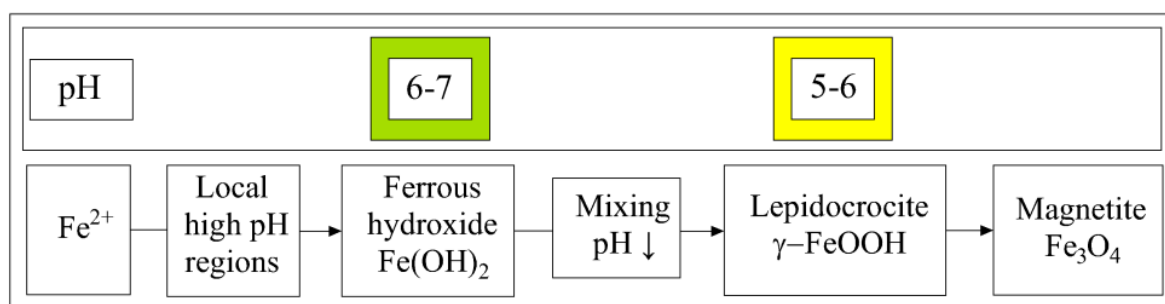


Figure 45. Parallel reaction of magnetite formation on addition of alkali to the salts solution.

Generally, monodisperse nanoparticles arise from a burst homogeneous nucleation followed by diffusion-controlled growth [144]. This is not the case for Sample I. A competition between several routes of magnetite formation results in

polydispersity of particles (Figures 38 a, b, c) and in poor reproducibility of their magnetic properties. The crystal lattice strain calculated from XRD data for Sample I is high (Table 7). As discussed before, these nanoparticles are not suitable for MH.

In the course of preparation of Sample II, when a solution of Fe^{3+} and Fe^{2+} salts is added to an alkali solution, the formation of magnetite occurs through a single intermediate stage, namely, through the formation of ferrihydrite [133, 157, 164]. The reaction starts in an alkaline medium at $\text{pH} \sim 11$. Under this condition, Fe^{3+} is hydroxylized to form ferrihydrite. Simultaneously, Fe^{2+} cations are incorporated into the ferrihydrite structure to form a mixed valence material, which is subsequently transformed into magnetite. The reaction is schematically illustrated in figure 46. This transformation proceeds rapidly and produces an abrupt supersaturation resulting in a burst of nucleation, the so-called homogeneous precipitation. The instantaneous change in the colour of the reaction mixture into black was observed as the first drops of iron salts solution reach the base solution. In contrast to Sample I, this reaction forms monodisperse nanoparticles of almost spherical shape (Figures 38 d, e, f).

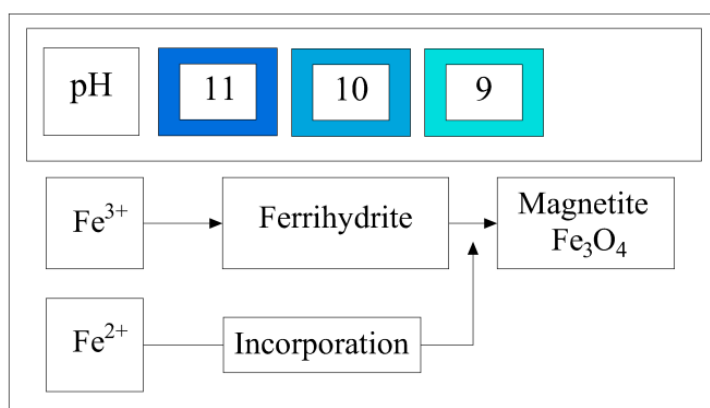


Figure 46. Coprecipitation reaction course: salts solution is added to the alkali solution.

To verify the initial magnetic phase formation in the reaction for Sample II and continuous phase transformations in the reaction for Sample I, the synthesis was interrupted at different time points and the reaction intermediates were isolated and analysed by VSM. As is shown in figure 47, in Sample I, the saturation magnetization reaches its maximum value in about 75 minutes after the start of the synthesis, at $\text{pH} \approx 8$, whereas, in Sample II, the magnetic phase with $M_s \sim 50 \text{ emu} \cdot \text{g}^{-1}$ is formed at the very beginning of the reaction.

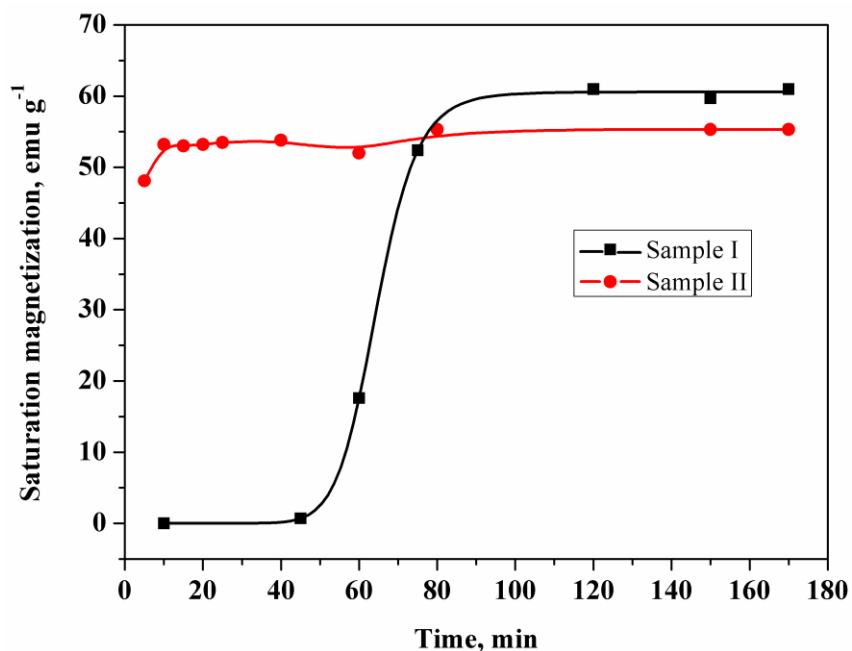


Figure 47. Variation of saturation magnetization during coprecipitation reaction.

The formation mechanism of nanoparticles during the synthesis of Sample II is explained by the results of average crystallite size determined by XRD analysis (d_{XRD}) and magnetization (M_s) of reaction intermediates separated at different stages of the reaction (Table 9). The growth rate of nanoparticles during coprecipitation reaction is presented in figure 48. The reaction product during the first five minutes represents nanocrystals with an average diameter of $d_{\text{XRD}} = 8.3$ nm, mixed phase composition (82 % of magnetite and 18 % of maghemite), high saturation magnetization of $M_s = 56$ emu·g⁻¹, and low values of crystal lattice strain ($\varepsilon = 0.3\%$). Note that, as the nanoparticle size increases during the reaction, the values of M_s and ε are not changed; however, the amount of the maghemite phase increases to 27 %. The change in the phase composition of a sample is associated with the decrease in the pH of the reaction medium [165].

Table 9. Effect of reaction time on the structural parameters of the reaction intermediates of Sample II determined from XRD pattern analysis.

Reaction time, (min)	pH of the reaction mixture	$a \pm 0.0004, (\text{\AA})$		$d_{\text{XRD}} \pm 0.5, (\text{nm})$	Magnetite content $\pm 3\%, (\%)$	Maghemite content $\pm 3\%, (\%)$
		Magnetite	Maghemite			
5	9.9	8.3849	$a=b=8.3672$ $c=24.9073$	8.3	82	18
10	9.7	8.3746	$a=b=8.3596$ $c=24.9670$	9.6	80	20
15	9.6	8.3636	$a=b=8.3509$ $c=24.9532$	9.9	79	21
20	9.4	8.3610	$a=b=8.3498$ $c=24.9986$	10.6	77	23
25	9.3	8.3601	$a=b=8.3486$ $c=25.0013$	10.8	74	26
40	9.1	8.3608	$a=b=8.3480$ $c=25.0015$	11.1	73	27
60	9.0	8.3600	$a=b=8.3470$ $c=25.0017$	11.4	72	28
80	8.7	8.3598	$a=b=8.3466$ $c=25.0189$	11.8	72	28

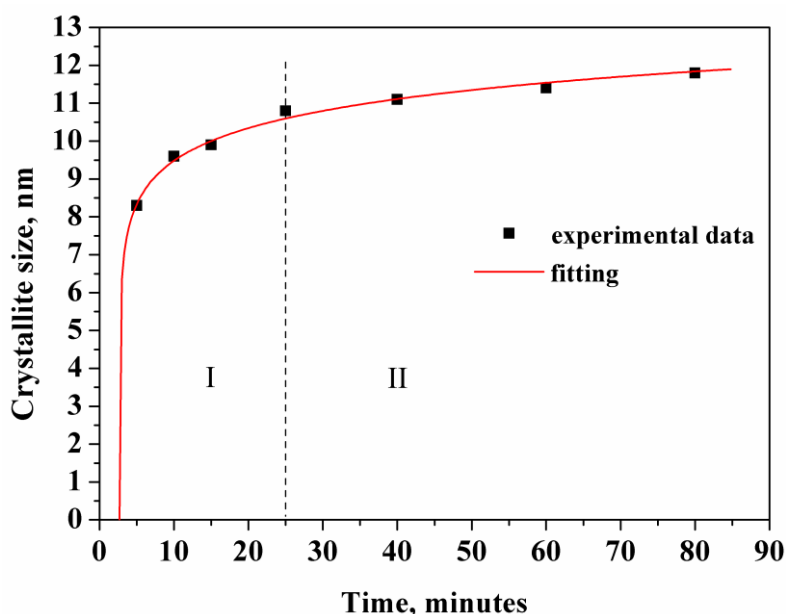


Figure 48. The dependence of crystallite size on the reaction time for Sample II. Black dots are the experimental values of crystalline size, measured from the peak broadening of XRD patterns. The solid red line shows the fitting of experimental results by a logarithmic function.

The experimental dependence of the particle size variation on the reaction time (Figure 48) is approximated by a logarithmic function; this points to the existence of two stages in the reaction: stage I with high growth rate, and stage II with low growth rate.

At the first stage, a supersaturation condition is reached, which is determined by the concentration of ferrihydrite with incorporated Fe^{2+} cations in the reaction medium. The supersaturation state immediately initiates the process of nuclei formation, which serve as building blocks for the formation of nanoparticles. As shown in [133], the fusion of nuclei leads to the formation of primary particles of various sizes. The growth of primary particles occurs via two mechanisms: (1) growth of large particles at the expense of small particles (the so-called Oswald ripening) and (2) attachment of nuclei to primary particles. Since the salt solution is added continuously during the synthesis, there occur both the formation of new primary particles and their growth. When a sufficient number of particles in the equilibrium state determined by the minimum of their surface energy is accumulated in the reaction medium, the growth rate decreases, and the process moves to stage II. At the second stage, the slow growth of particles is continued until the end of the reaction when the solution of salts is completely exhausted. The driving force of growth is the tendency of all particles to grow to the equilibrium state, which leads to the formation of nanoparticles with approximately the same size. Simultaneously, the aggregation of nanoparticles occurs due to magnetic interactions leading to the decrease of magnetostatic energy of individual nanoparticle.

Thus, it is shown that coprecipitation reaction in an alkaline medium with slow addition of salts of iron (II) and iron (III) to alkali stimulates instantaneous homogeneous nucleation and a slow growth of particles at the final stage of the reaction. This leads to the formation of magnetic nanoparticles of spherical shape with a narrow size distribution, high crystallinity, and high values of saturation magnetization. It should be also noted that such a reaction guarantees the reproducibility of the structural and magnetic properties of nanoparticles and, hence, their heating efficiency in AC magnetic fields.

3.1.3. Effect of post-treatment by annealing of iron oxide nanoparticles on their structural and magnetic properties

Further work on the optimization of nanoparticles properties was devoted to Sample II due to its set of reproducible properties: uniformity, high crystallinity, high saturation magnetization and high heating potential in AC magnetic field. Hereinafter this sample is referred as original sample.

The original sample consists of 72% of magnetite and 28 % of maghemite. Such a mixed phase composition may cause the variation in the values of energy barrier of magnetization reversal and the decrease in SLP. Therefore a post-treatment of obtained nanoparticles was performed in order to prepare pure maghemite nanoparticles. As maghemite is a stable form of magnetic iron oxide, it does not

undergo oxidation at room temperature, then the post-treatment will also ensure the stability of magnetic properties of nanoparticles over time.

It is known that magnetite readily oxidises to maghemite at elevated temperatures on air [24], therefore to obtain pure maghemite nanoparticles the annealing of original sample was performed. As maghemite is a stable form of iron oxides from the viewpoint of oxidation, thus the annealing of the mix phase nanoparticles also leads to the stability of magnetic properties over time.

The annealing of nanoparticles of original sample was carried out at 300 °C in air for 2 and 6 hours and two samples were obtained, named as 2h annealed sample and 6 h annealed sample, respectively. The annealing parameters were chosen so that:

- (1) To achieve complete oxidation of magnetite to maghemite and thus to obtain single-phase nanoparticles and
- (2) To prevent the formation of hematite (to this end, temperature should be kept below 320 °C [24]).

The annealing does not change the morphology of the nanoparticles (Figure 49), but the annealing time affects their phase composition, which is discuss below.

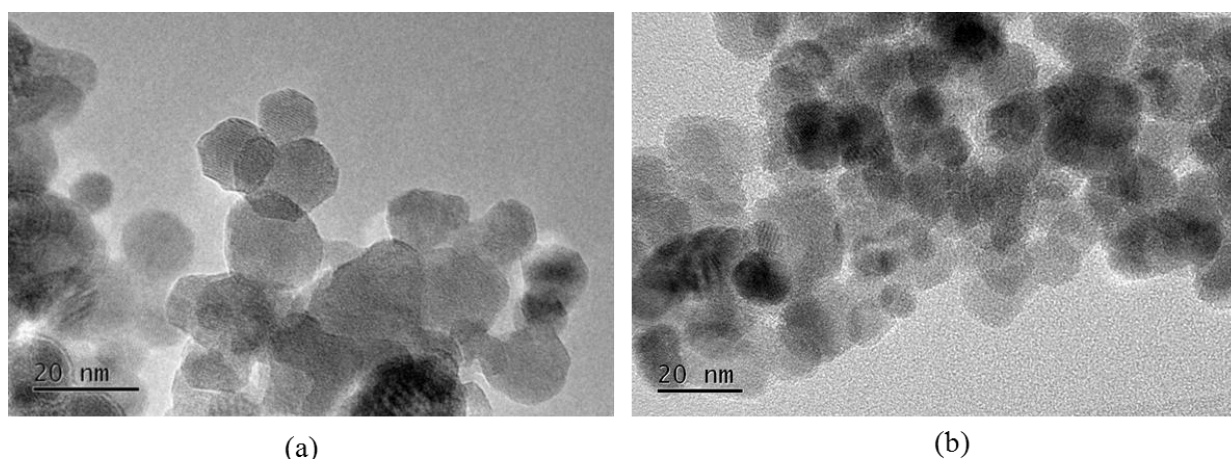


Figure 49. TEM images of (a) 2 h annealed sample and (b) 6 h annealed sample.

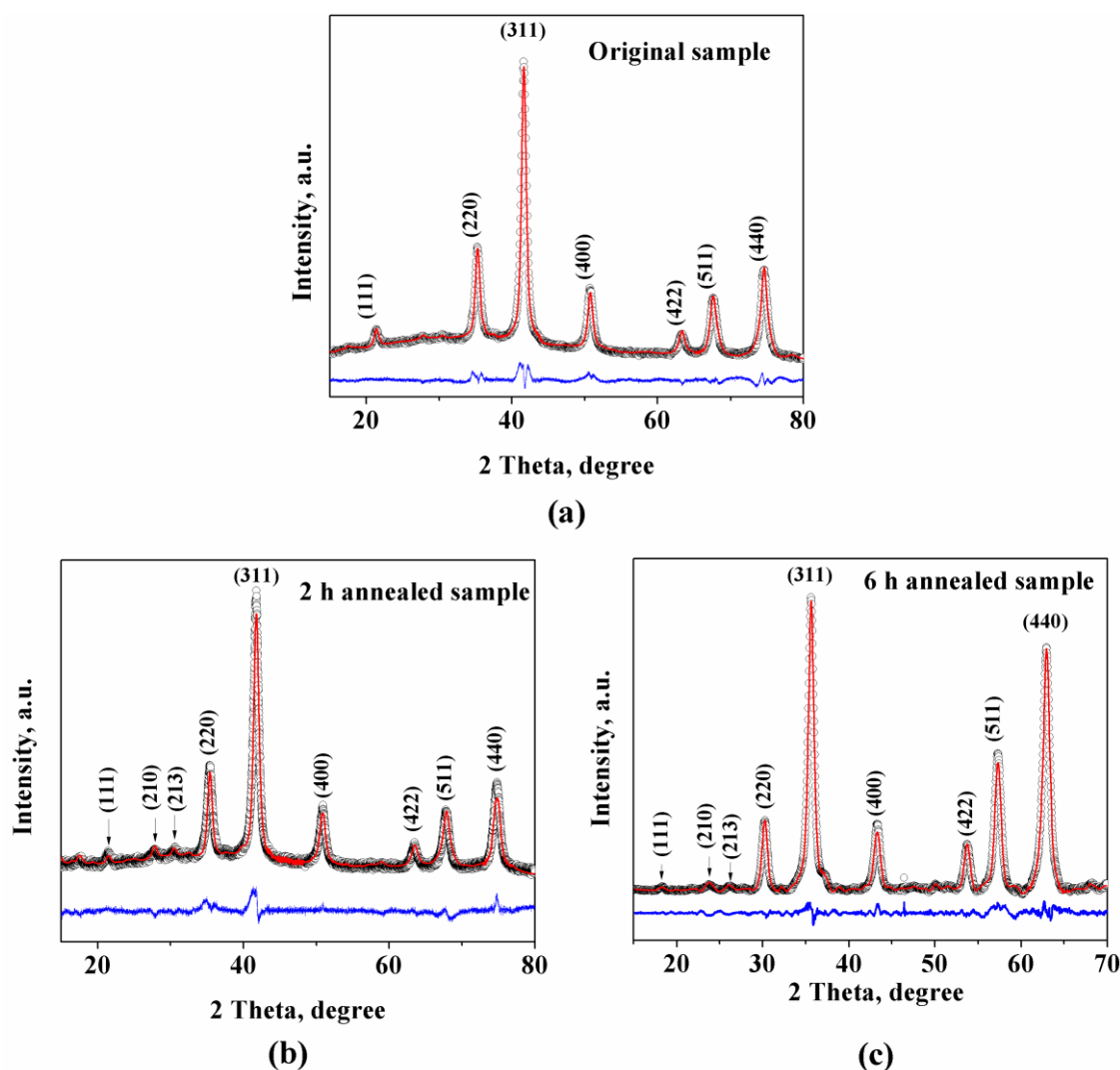


Figure 50. XRD patterns of (a) original sample, (b) 2 h annealed sample, (c) 6 h annealed sample.

Figure 50 represents the XRD patterns of original and annealed samples. Seven diffraction peaks corresponding to the lattice planes (111), (220), (311), (400), (422), (511), and (440) of the cubic spinel structure of magnetite are detected for all samples. While the patterns of annealed samples display two additional peaks corresponding to the lattice planes (210) and (213) of the tetragonal structure of maghemite. The average crystallite size, phase composition, and crystal lattice strains determined by the XRD data refinement are listed in table 10. It was established that the annealing of the original sample for 2 hours decreases the content of magnetite to 45 %, and annealing for 6 hours leads to almost complete oxidation of magnetite to maghemite (92 %). The low value of crystal lattice strain and well-resolved XRD peaks indicate the high crystallinity of all the samples.

Fast Fourier transformation of HRTEM images of the original and 2 h annealed sample revealed the presence of both magnetite and maghemite single-phase nanoparticles (Figure 51). However, no core-shell structure, which was suggested

for partially oxidized magnetite nanoparticles, where core is magnetite and shell is maghemite [158], was observed on the HRTEM images.

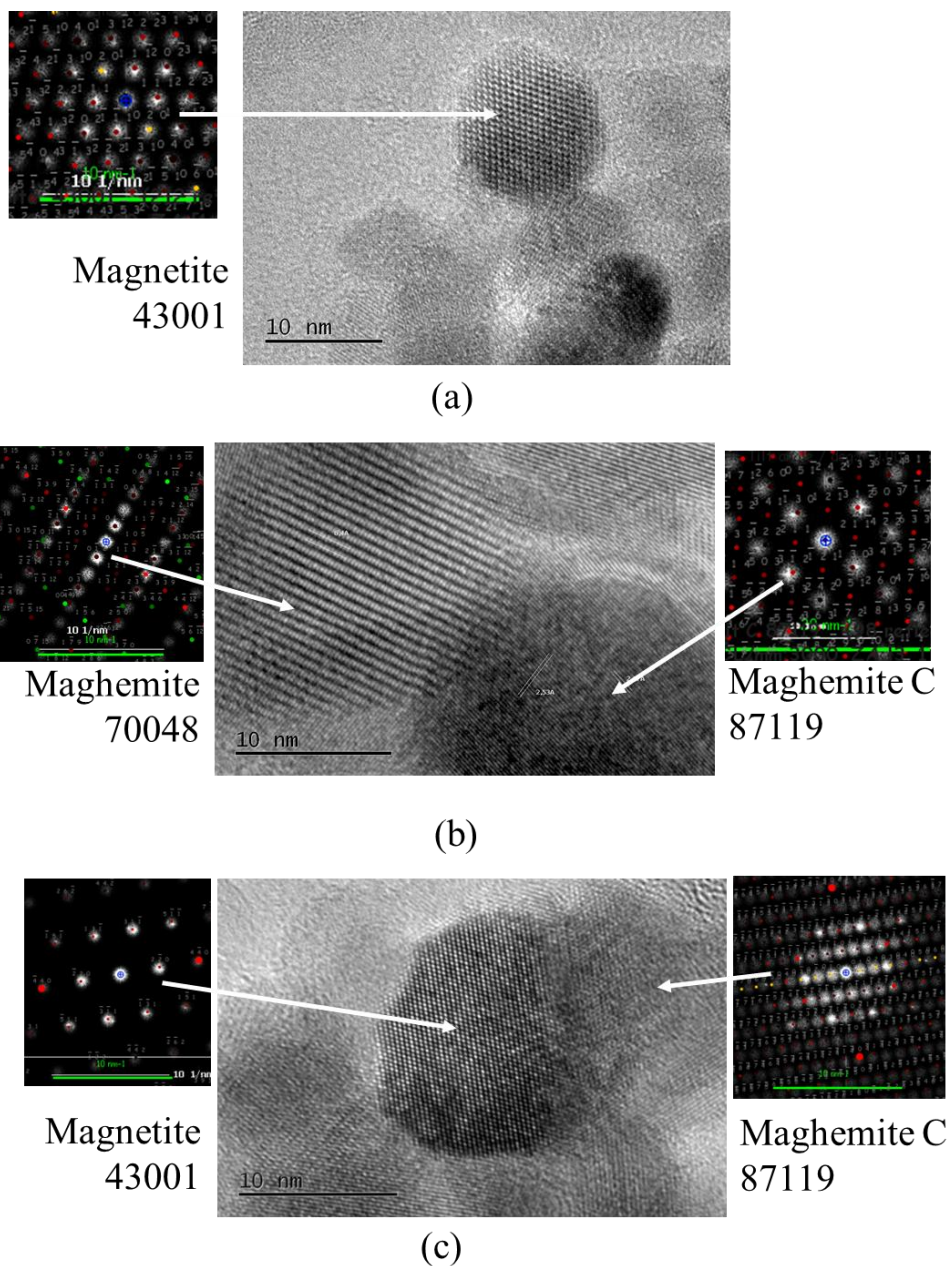


Figure 51. HRTEM images with fast Fourier transformation of the (a, b) original sample, and (c) 2 h annealed sample.

Table 10. Structural and magnetic properties of iron oxides nanoparticles.

Property	Original sample	2 h annealed sample	6 h annealed sample
d_{TEM} , (nm)	13	13	13
σ_{TEM}	0.3	0.3	0.3
d_{XRD} , (nm)	12	14	12
ε , (%)	0.3	1.7	0.6
Magnetite content determined from XRD, (%)	72	45	8
Magnetite content determined from MS, (%)	60	58	0
M_s , ($\text{emu}\cdot\text{g}^{-1}$)	56 ± 2	50 ± 1	48 ± 1
M_r , ($\text{emu}\cdot\text{g}^{-1}$)	0.8 ± 0.2	0.9 ± 0.2	0.8 ± 0.2
H_c , (Oe)	11 ± 4	10 ± 3	10 ± 3
μ' at 10^7 Hz	3.40	2.90	3.40
μ''_{max}	1.32	1.00	1.47
f_r , (GHz)	2.01	2.09	2.18

Magnetization curves at room temperature for original and annealed samples are shown in figure 52. The corresponding values of M_s , M_r and H_C are listed in Table 10. The annealing decreases M_s from $56 \text{ emu}\cdot\text{g}^{-1}$ to $48 \text{ emu}\cdot\text{g}^{-1}$ due to the transformation of magnetite into maghemite. However, no change in H_C after annealing was observed. Taking into account the fact that the size and the shape of nanoparticles, as well as the lattice strain, were not changed after annealing, it is possible to assume that the value of effective magnetic anisotropy remains the same.

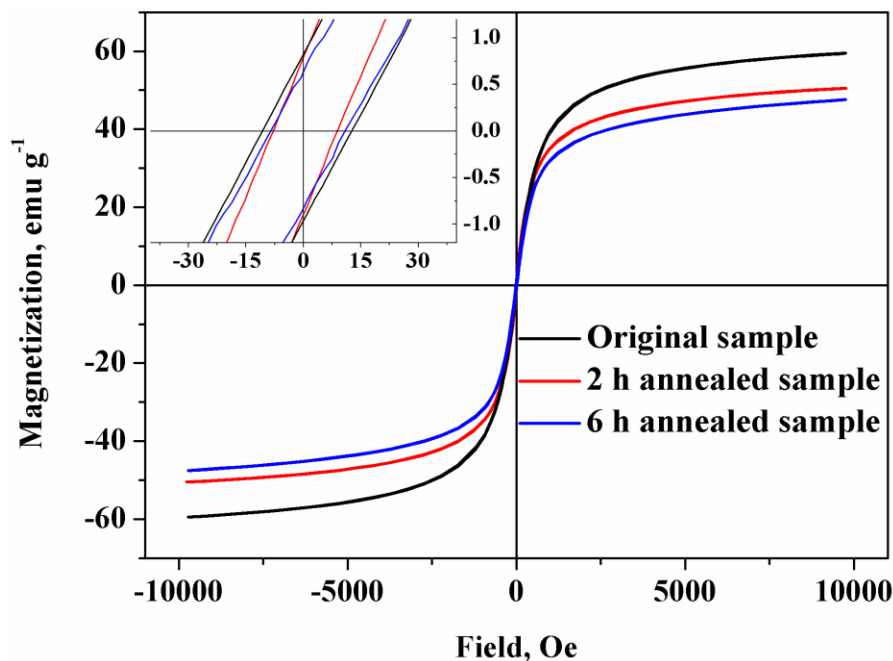


Figure 52. Magnetization curves at room temperature for the original and annealed samples. The inset shows the central area of the loops at higher magnification.

The complex magnetic permeability dispersion in the samples occurs in the high-frequency part of the RF band (Figure 53), where the NFR of the ferrites with cubic structure occurs [2]. Samples differ from each other in the real part of permeability μ' and the magnetic loss μ''_{max} , and slightly differ in the resonance frequency f_r (Table 10). It should be noted that a 2h annealed sample shows the smallest values of μ' and μ''_{max} . The observed difference between the magnetic spectra of a 2 h annealed sample and other samples can be explained by the more pronounced effect of demagnetizing fields in this sample. It is known that the NFR is determined by magnetization rotation in effective magnetic anisotropy fields and demagnetizing fields [2]. The source of demagnetizing fields in multi-phase systems is the interface between phases with different magnetic properties, and a 2 h annealed sample has the largest interface between magnetite and maghemite phases.

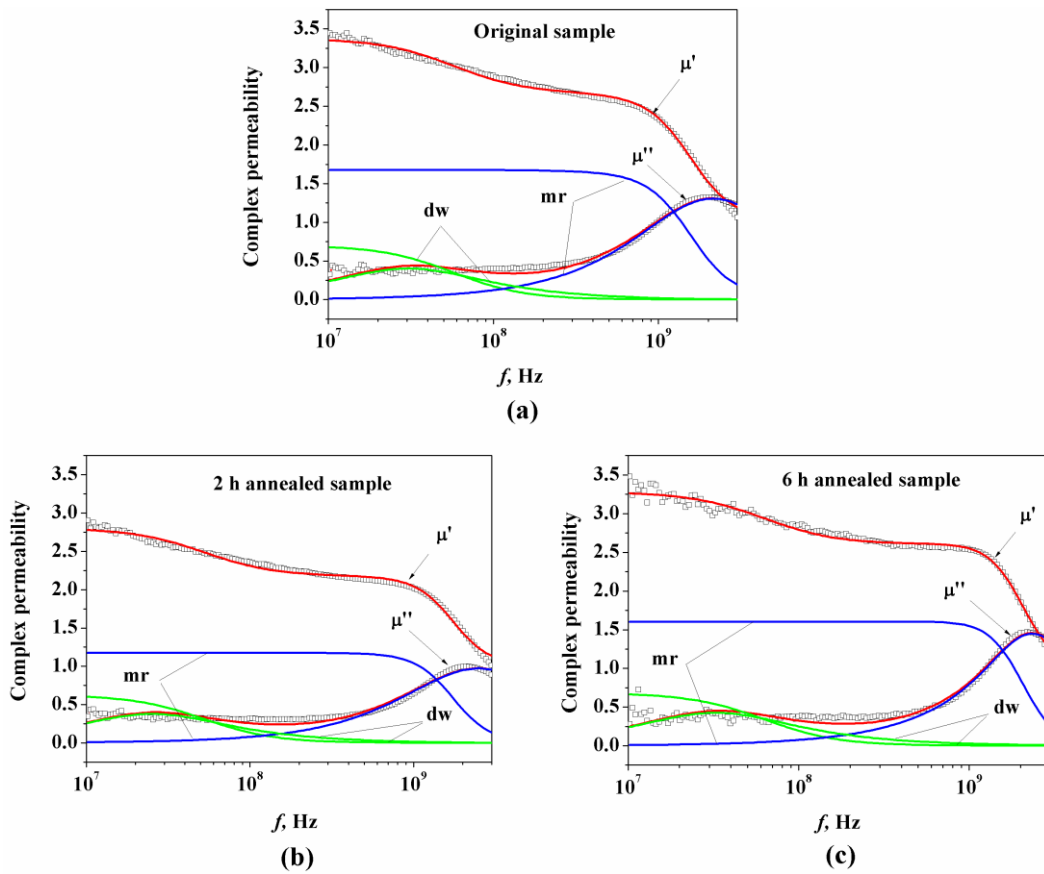


Figure 53. Permeability spectra: (a) original sample, (b) 2 h annealed sample and (c) 6 h annealed sample. The experimental values of μ' and μ'' are indicated by open squares. The coloured solid lines show the total permeability calculated with regard to the contributions of domain wall motion (**dw**) and magnetization rotation (**mr**).

The approximation of magnetic spectra of annealed samples by the dispersion formula [154] reveals the dominant role of magnetization rotation to the complex permeability, thus indicating that annealed samples are in a SD state as is the original sample. These results show that annealing has no effect on the magnetic state of nanoparticles, Taking into account that according to the average particle size nanoparticles are SPM it is possible to conclude that nanoparticles are SD in the SPM state. However, non-zero values of coercivity and remanent magnetization show that the nanoparticles are in the ferromagnetic state. In order to resolve this contradiction, Mössbauer spectroscopic studies of the samples at 5 K and 293 K were carried out (Figure 54). The Mössbauer parameters are listed in Table 11.

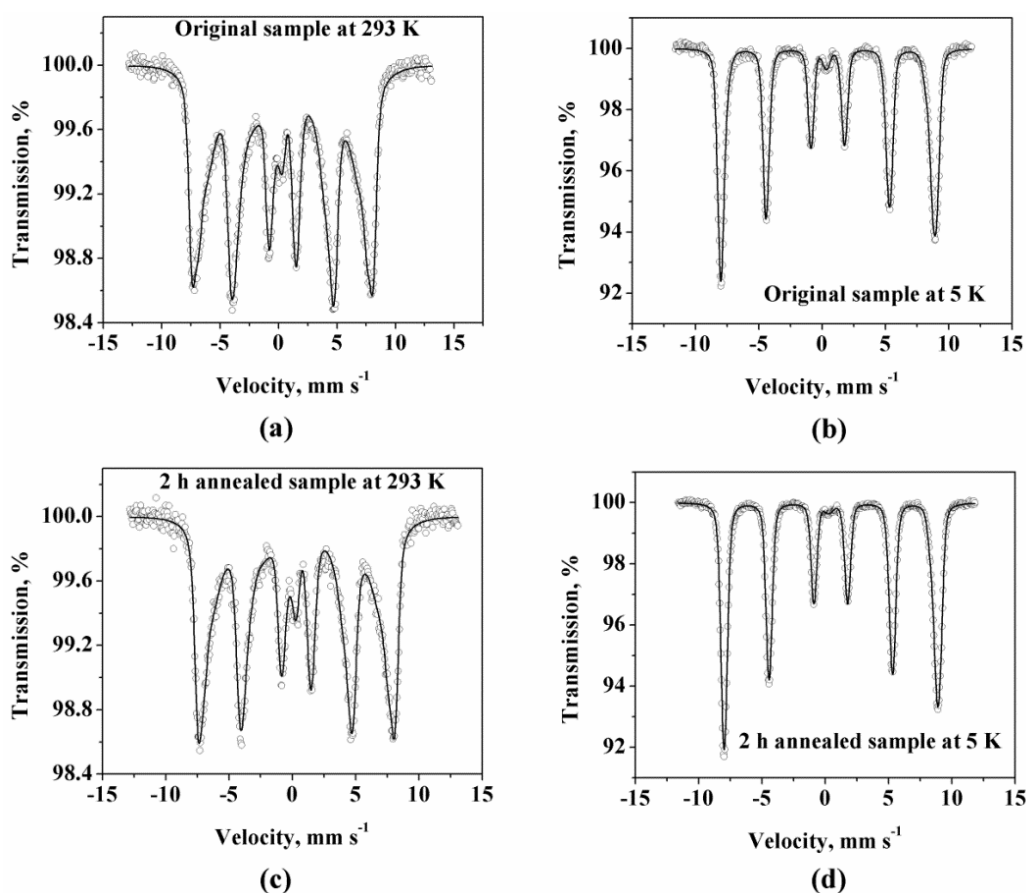


Figure 54. Mössbauer spectra: (a, b) of the original sample (c, d) of the 2 h annealed sample at 293 K and at 5 K.

The samples exhibit similar MSs at 293 K and at 5 K: the experimental data can be fitted by three / four sextets with well-developed magnetic hyperfine splitting indicating the magnetic ordering of Fe ions and ferromagnetic state of the materials. However, the hyperfine field values detected from room temperature MSs are lower than those of bulk magnetite and maghemite [147]. Such decrease in the hyperfine field values is attributed to the size effect [148].

The relative amounts of magnetite and maghemite in the samples, calculated from the MSs at 5 K are listed in Table 10. The MSs at 5 K have been used for calculations to escape the thermal relaxation effects. The results obtained slightly differ from the XRD data. Because these two methods provide an approximate phase composition of magnetic iron oxide nanoparticles due to the superposition of the diffraction patterns of magnetite and maghemite in the XRD data and the strong overlapping of the MS components.

Table 11. Mössbauer parameters of samples at 293 K and 5 K. Af is the atomic fraction of the component in the MSs.

Sample	Spectrum component	Af	$I_s, \text{mm}\cdot\text{s}^{-1}$	B_{hf}, T
Original 293 K	1st sextet	0.22	0.33	48.2
	2nd sextet	0.11	0.36	45.0
	3rd sextet	0.30	0.30	42.0
	4th sextet	0.36	0.65	33.0
Original 5 K	1st sextet	0.38	0.53	53.2
	2nd sextet	0.32	0.37	52.3
	3rd sextet	0.30	0.39	50.8
2 h annealed 293 K	1st sextet	0.27	0.33	48.2
	2nd sextet	0.11	0.33	45.2
	3rd sextet	0.31	0.29	42.8
	4th sextet	0.31	0.56	34.4
2 h annealed 5 K	1st sextet	0.42	0.47	53.3
	2nd sextet	0.48	0.42	51.9
	3rd sextet	0.10	0.32	50.0

The temperature dependence of magnetization of the original sample in the ZFC and FC regimes measured in an external magnetic field of 50 – 1000 Oe is presented in figure 55. The shapes of the ZFC and FC curves differ from those for SPM nanoparticles [83, 151]. According to the results obtained, there is no maximum on the ZFC curve. In low magnetic fields (of 50, 100 and 500 Oe), T_{ir} lies above 300 K; i.e., the ZFC and FC curves in these fields do not overlap over the whole range of temperatures. As the magnetic field amplitude increases to 1 kOe, T_{ir} becomes about 300 K. It is known that nanoparticles obtained are aggregated and therefore should display strong magnetic interactions, which lead to a shift of the blocking temperature toward higher temperatures. A similar effect of interparticle interactions has already been discussed, for example, for bioaffine ligand-coated iron oxide

nanoparticles, less than 20 nm in diameter, that are gathered in clusters [166]. Magnetic interactions between particles change the energy barrier and affect the blocking temperature; as a consequence, the material exhibits a non-zero coercive field. Thus, it is possible to conclude that interparticle interactions lead to the room temperature ferromagnetism in the nanoparticles obtained, which should be in the SPM state according to their particle size.

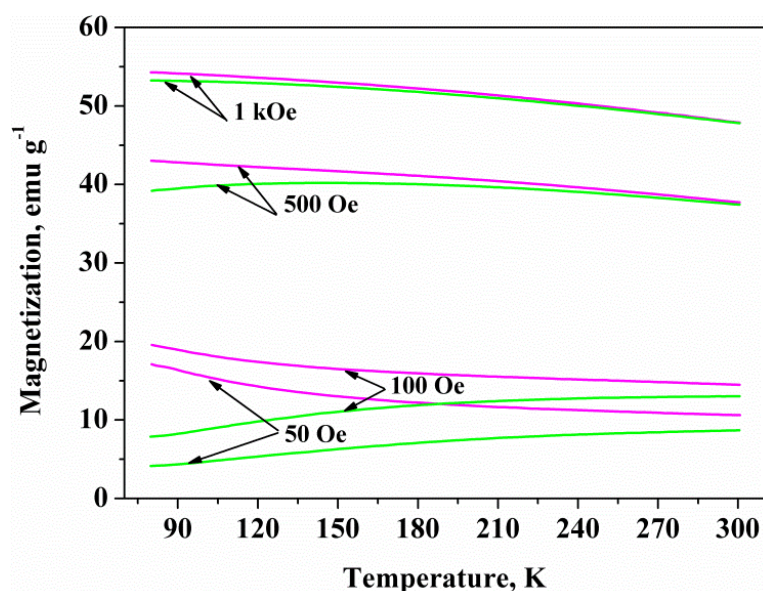


Figure 55. FC (pink) and ZFC (green) curves of the original sample for different intensities of the external magnetic field.

3.1.4. Alternating magnetic field energy absorption in dispersion of iron oxide nanoparticles in viscous medium: Effect of interparticle interactions and properties of carrier medium

The thermal response of nanoparticles of original and annealed samples to an AC magnetic field was studied using calorimetric measurements. The powders of nanoparticles were dispersed in a viscous glycerol medium with concentrations from 2 wt. % to 7 wt. %, which are typical of *in-vivo* and clinical studies in MH [21, 23, 44, 87]. All samples demonstrated rapid heating at all frequencies and amplitudes of AC magnetic fields: the hyperthermic temperatures were attained in all dispersions within tens of seconds (Figure 56).

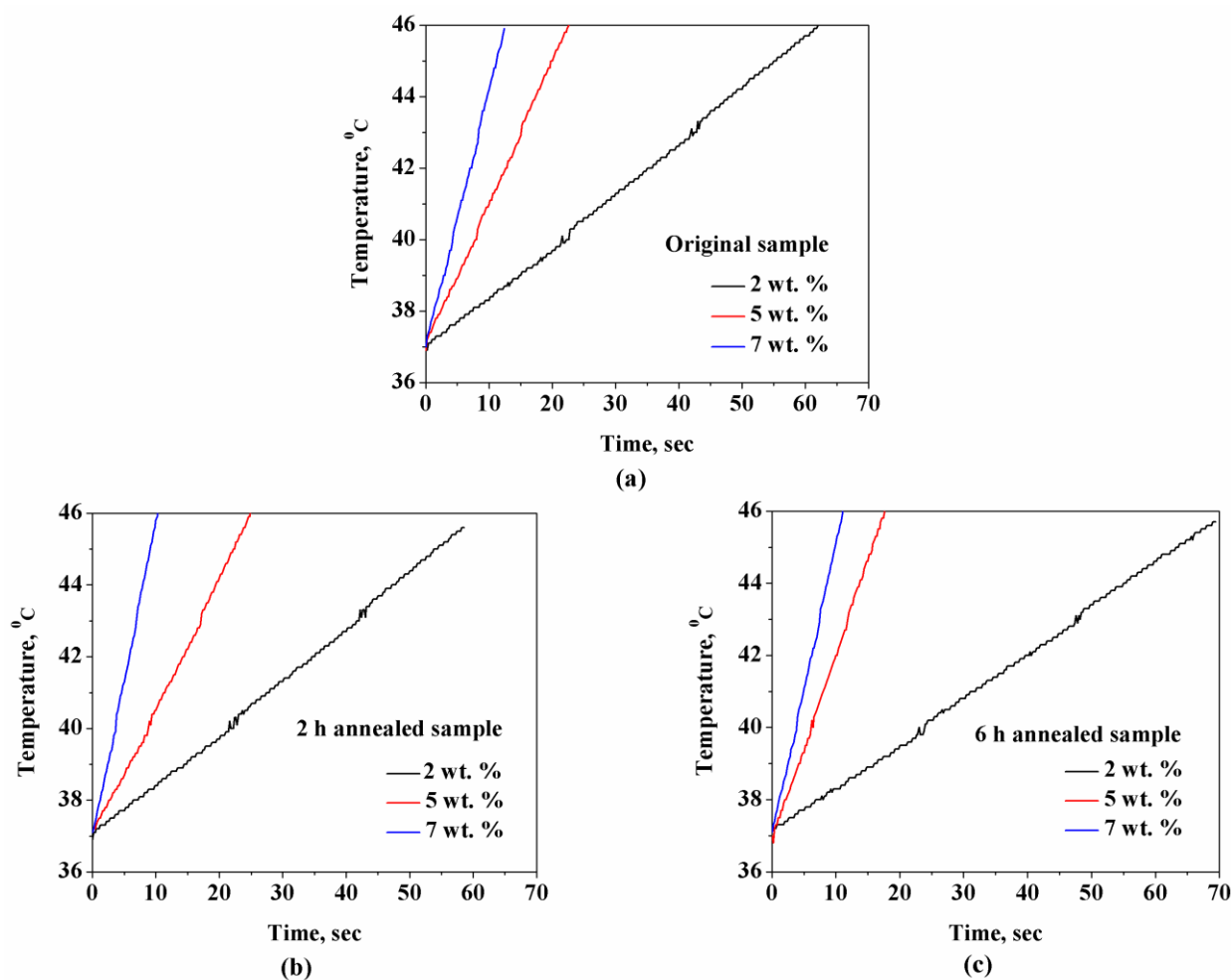


Figure 56. Inductive heating of iron oxide nanoparticles dispersions: (a) of original sample, (b) of 2h annealed sample, and (c) of 6 h annealed sample at AC magnetic field of $7.6 \text{ kA}\cdot\text{m}^{-1}$ alternating at 525 kHz.

No significant difference between the SLP values for the original and annealed samples was observed; therefore, the phase composition has a minor impact on the SLP (Table 12). Nevertheless, calculated values of SLP do not exceed $30 \text{ W}\cdot\text{g}_{\text{Fe}}^{-1}$. The results obtained are explained by the combined effect of interparticle magnetic interactions and the properties of the carrier medium.

Table 12. SLP values of nanoparticles dispersions (2 wt. %, 5 wt. % and 7 wt.%) in glycerol in AC magnetic fields of various frequencies and amplitudes.

AC magnetic field	f , kHz	114 kHz	525 kHz		1048 kHz
	H , kA·m ⁻¹	13.8 kA·m ⁻¹	5.8 kA·m ⁻¹	7.6 kA·m ⁻¹	5.8 kA·m ⁻¹
Original sample	2 wt.%	14.1 ± 0.1	10.2 ± 1.3	18.0 ± 2.1	16.9 ± 0.4
	5 wt.%	17.4 ± 0.7	13.4 ± 2.1	23.1 ± 2.2	23.0 ± 3.1
	7 wt.%	19.6 ± 0.6	15.2 ± 1.9	26.1 ± 2.5	25.8 ± 1.5
2h. annealed sample	2 wt.%	16.5 ± 1.1	9.1 ± 1.6	17.9 ± 1.8	14.6 ± 0.4
	5 wt.%	20.8 ± 2.3	11 ± 1.0	23.1 ± 0.4	18.1 ± 2.3
	7 wt.%	32.6 ± 1.6	16.7 ± 1.5	31.6 ± 0.8	22.7 ± 1.4
6h. annealed sample	2 wt.%	17.5 ± 0.7	8.4 ± 0.9	17.3 ± 1.2	13.4 ± 0.4
	5 wt.%	26.5 ± 1.9	13.6 ± 1.6	26.8 ± 0.6	20.3 ± 1.5
	7 wt.%	31.1 ± 1.0	16.8 ± 1.6	30.0 ± 0.7	21.8 ± 1.7

The heating rate of dispersion is determined by the intrinsic properties of nanoparticles, their concentration, the field parameters, as well as by the heat capacity of the carrier medium. An increase in the nanoparticles concentration leads to the increase in the heating rate. The low specific heat capacity of glycerol contributes to the high heating rate of the dispersion. At the same time, glycerol has high viscosity η , which decreases, as temperature increases, from $\eta = 1.41$ Pa·s at 20 °C to $\eta = 0.14$ Pa·s at 50 °C. Presently, it is theoretically established that, at such viscosity, the magnetization process is determined solely by the Néel relaxation, which limits the value of SLP to tens of W·g⁻¹ [15]. Meanwhile, the highest values of SLP of the order of 1 – 2 kW·g⁻¹ were obtained in a dispersion of iron oxide particles in water [89, 109], where two mechanisms of magnetization rotation, Néel and Brownian, account for the high heat generation. It should also be noted that high values of SLP reported in the literature are obtained for high field amplitudes (much higher than 15 kA·m⁻¹), while, in the current work, the heating effect is studied in AC magnetic fields with amplitudes below 15 kA·m⁻¹.

Therefore, the heat generation in the viscous dispersions of nanoparticles obtained subjected to an AC magnetic field of moderate amplitude is predominantly due to

the Néel relaxation loss. At the same time, the high heating rate observed in such systems is determined by the presence of nanoparticle aggregates that exhibit ferromagnetic behaviour with hysteresis. Nanoparticles are bound together during the synthesis through interparticle exchange interactions[14]. These interactions result in an increase in the effective magnetic anisotropy in a system, which, in turn, increases the magnetization reversal energy barrier and thus decreases the effect of thermal fluctuations on magnetization dynamics.

To sum up, for preparation of iron oxide nanoparticles for MH the following work was done:

- (1) Magnetic iron oxide nanoparticles were synthesized by coprecipitation; the reaction parameters were established that provide nanoparticles with a set of magneto-structural properties required for their application in MH.
- (2) The mechanism of nanoparticles nucleation and growth was determined and correlated with structural properties of nanoparticles.
- (3) The heating ability of nanoparticles in AC magnetic fields at frequencies and amplitudes allowed in MH was investigated.
- (4) The dispersions of nanoparticles (2 – 7 wt. %) in glycerol demonstrate high heating rate in AC magnetic fields of all tested frequencies and moderate amplitudes, i.e. the dispersions temperature increased from 37 °C to 45 °C within tens of seconds.
- (5) The heat output of nanoparticles dispersions in AC magnetic fields is explained by combined effect of magnetic interparticle interactions and properties of carrier medium (viscosity and heat capacity).
- (6) The developed magnetic nanoparticles are intended for preparation of a polymer composite material for application in AEH.

3.2. Maghemite based silicone composite for arterial embolization hyperthermia

The next step of the work was devoted to the preparation of the magnetic mediator, which can be applied in AEH. In AEH the hyperthermic effect is combined with effect of arterial occlusion. For successful performance of AEH two factors should be accomplished simultaneously: (1) effective embolization and (2) attaining of hyperthermic temperatures.

In the current work the mediator represents a polymer composite material, composed of:

- Polymer matrix – silicone elastomer which is characterized by non-toxicity, non- antigenicity, stability for lysis,
- Magnetic filler – maghemite nanoparticles (6 h annealed sample) with stable over time magnetic properties.

To prepare the magnetic composite material for application as heat mediator in AEH the following investigations have been carried out:

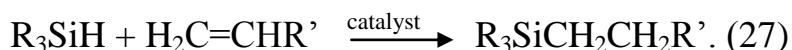
- (1) Polymer matrix of the composite was prepared by the hydrosilylation reaction of silicones with vinyl- and hydro-side groups.
- (2) The influence of initial components concentrations (silicones with vinyl- and hydro-side groups, plasticizer, and magnetic filler) on the composite's rheological properties was studied.
- (3) The optimal composition was estimated, which provides simultaneously low initial viscosity for delivery through catheters and controlled vulcanization time for successful performance of blood vessels embolization.
- (4) Radiopaque property of mediator was investigated.
- (5) The heating potential of mediator was analyzed in AC magnetic field at frequencies and amplitudes allowed for MH.
- (6) The heat output of mediator in AC magnetic field was explained by heating efficiency of magnetic filler and low specific heat capacity of silicone.

The detail explanation of work done is given below.

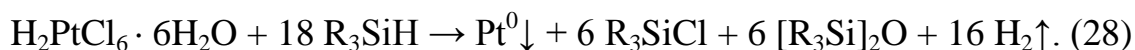
3.2.1. Composite formation

The silicone magnetic composite was prepared by hydrosilylation reaction of hydro- and a vinyl-functional silicone polymers in the presence of maghemite nanoparticles. In course of composite preparation the content of the flask A (PVS, maghemite nanoparticles, CAT) was mixed together with the content of the flask B (PHS, PDMS) (Figure 25, Section 2.1.2.).

Once the contents of the flasks are mixed the polyaddition reaction starts. The vinyl- groups of PVS react with hydro- groups of PHS. Chloroplatinic acid dissolved in poly(dimethylsiloxane) to prevent it's oxidation serves as a catalyst of hydrosilylation process [167]:



L. N. Lewis et al. have shown that at the first step of the hydrosilylation reaction hydrosiloxane reacts with the platinum complex forming the colloidal platinum, which then catalyses the addition reaction (27) [168, 169]:



The formation of the colloidal platinum is slow. That is why the hydrosilylation reaction is characterized by presence of induction period. During the induction period the viscosity of the reaction medium remains almost constant, and after that the viscosity increases rapidly due to the reaction between vinyl- and hydro- groups leading to the crosslinking of the polymer chains. A clear indication of the colloidal platinum formation is the emission of hydrogen, forming boodles in the composite. Maghemite nanoparticles don't take part in the reaction and serve as filler and PDMS is utilized as a plasticizer to adjust the viscosity of the composite.

The FTIR spectra of the PHS and the composite materials are presented in figure 57. As it is seen from the spectra, the Si-H stretching peak at 2100 cm^{-1} presents in the spectrum of PHS but disappears in the spectrum of composite. It shows that all hydro-groups were consumed during the reaction.

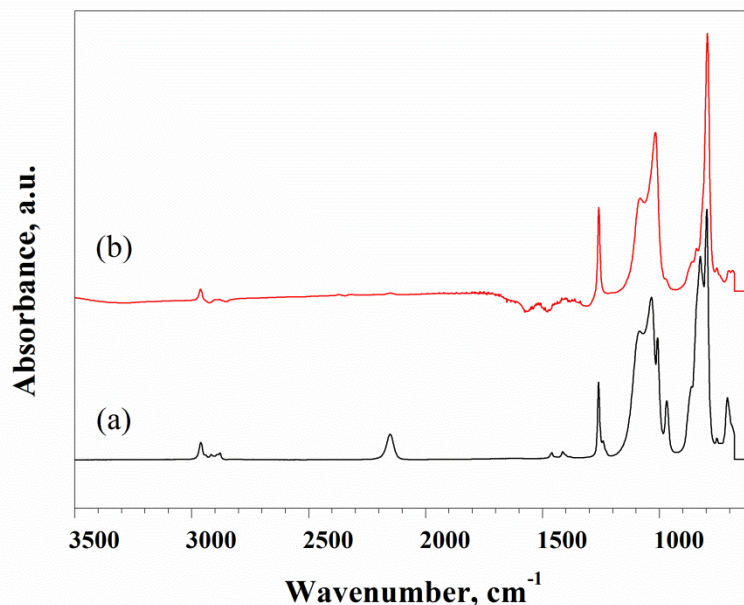


Figure 57. FTIR spectra of (a) PHS and (b) silicone magnetic composite.

3.2.2. Rheological study of composite formation: choice of embolic composition

The rheological measurements were performed at 38 °C which corresponds to average internal human temperature. After mixing of the contents of vessel A and B (Figure 25, Section 2.1.2.) the liquid system was loaded onto parallel plate geometry. The upper plate was oscillated at fixed frequency, ω , and fixed maximum strain, γ_M . The response signal, stress wave, different in phase and amplitude from strain wave, was monitored.

Variation of rheological properties of the composite during its formation is presented in figure 58. At the beginning no changes in G' and G'' are observed and the viscosity of the system stays constant, this corresponds to the induction period of the reaction. During the induction period the composition is in a fluid state which is evidenced by a greater value of G'' over G' . As the reaction between vinyl- and hydro-groups starts, both G' and G'' increase, but G' increases faster than G'' . After a certain time the crossover between G' and G'' is observed which is called the vulcanization point. Above the vulcanization point the elastic component dominates over viscous, $G' > G''$, and the viscosity of the composition rapidly increases till it reaches a maximum. The viscosity stays constant after all the hydro-groups have reacted.

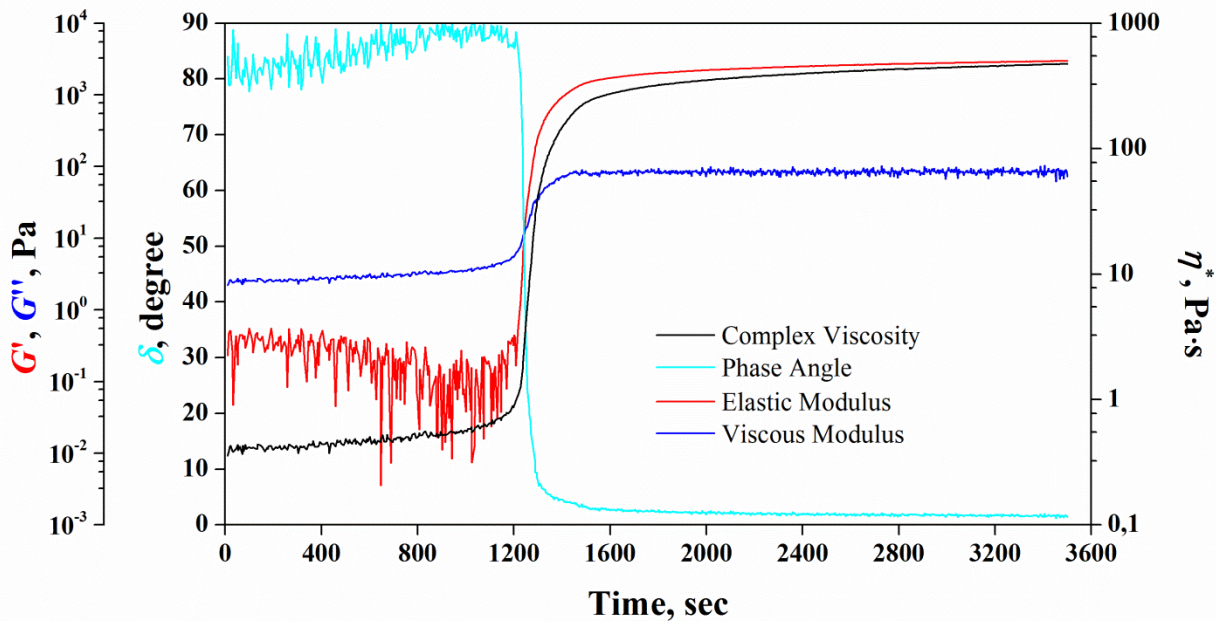


Figure 58. Kinetics of the composite formation.

The investigation of the impact of the relative concentration of initial reagents on the induction period time t_{in} , initial viscosity, η^*_{in} , and final viscosity, η^*_{fin} , of the composite was performed, as for the practical application these parameters are crucial. In order to introduce the embolization material in the artery through thin catheter the initial viscosity of the composition should be of the order of 0.5 Pa·s. The requirements for the initial viscosity depend on the morphology of blood vessels to be occluded; for occlusion of large vessels the material with high initial viscosity is needed and for small vessels the less viscous material is superior [170]. The induction period during which the viscous component is dominated over elastic, is the time during which the surgeon has to administrate the embolization material to the blood vessel. Usually 15-20 minutes are necessary to accomplish the delivery and distribution of material in the tumour's blood vessels [141, 170]. Then the occlusion of the blood vessel occurs due to polymer crosslinking with formation of soft emboli. Note that the emboli should stop the blood flow but, at the same time, should not injure the vessel, i.e. be flexible and able to bend with the vessels. Thus the effect of each composite's component concentration on the rheological properties was studied with a view to find out the optimal embolic agent composition.

Effect of PHS concentration on rheological properties of composite

The induction period is affected in the large extent by the PHS concentration as it takes part in the formation of colloidal platinum serving as an active catalyst of hydrosilylation reaction (Equation 28). The influence of PHS concentration on the rheological properties of the composite was studied by varying PHS concentration,

whereas other component's concentrations were the same (Table 13). The concentration of maghemite nanoparticles in composites was 2 wt. %.

Table 13. Effect of PHS concentration on rheological properties of the composite.

Relative concentration of the initial components, mass fraction				η^*_{in} , Pa·s	η^*_{fin} , Pa·s	t_{in} , min
PVS	CAT	PHS	PDMS			
2.5	0.1	0.2	0	2.2	6250	90
2.5	0.1	0.3	0	2.0	5755	31
2.5	0.1	0.5	0	2.0	4000	18
2.5	0.1	1.0	0	1.1	1100	11
2.5	0.1	1.6	0	0.8	300	8
2.5	0.1	1.8	0	0.8	120	8

For the composition with PHS mass fraction of 0.2 the induction period is long, since low concentration of PHS leads to the formation of low amount of colloidal platinum. With the increase of PHS concentration the induction period time decreases and reaches minimum value (Figure 59). This time corresponds to the reaction time of colloidal platinum formation. Further increase of PHS concentration has no effect on the induction period time.

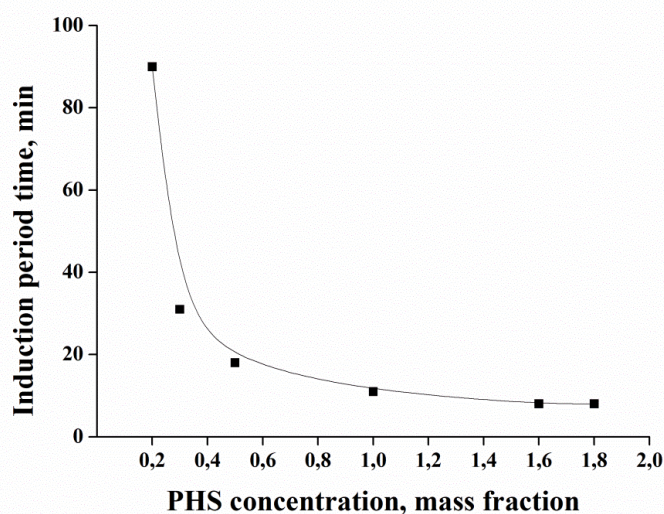


Figure 59. Dependence of induction period time on PHS concentration at constant concentration of the other components of the mixture.

Consequently, to achieve the duration of the induction period about 15 – 20 min, which is the time needed for delivery and distribution of material, the concentration of PHS of 0.6 – 0.7 mass fractions is chosen as optimal and used in further study of rheological properties.

Effect of plasticizer concentration on rheological properties of composite

It is established that the presence of plasticizer in the composition has a minor effect on the induction period time, which remained about 20 minutes (Table 14). However it is possible to adjust necessary initial and final viscosities of composite by varying plasticizer concentration.

Table 14. Effect of plasticizer concentration on rheological properties of composite.

Relative concentration of the initial components, mass fraction				η^*_{in} , Pa·s	η^*_{fin} , Pa·s	t_{in} , min
PVS	CAT	PHS	PDMS			
2.5	0.1	0.6	0	1.7	3000	20
2.5	0.1	0.6	0.6	1.1	2100	18
2.5	0.1	0.6	1.0	0.8	1300	19
2.5	0.1	0.7	1.5	0.6	750	19
2.5	0.1	0.7	2.0	0.4	500	21

Figure 60 depicts the effect of plasticizer concentration on the initial and final viscosities of the composite. As it is seen both parameters decrease with the increase of PDMS concentration.

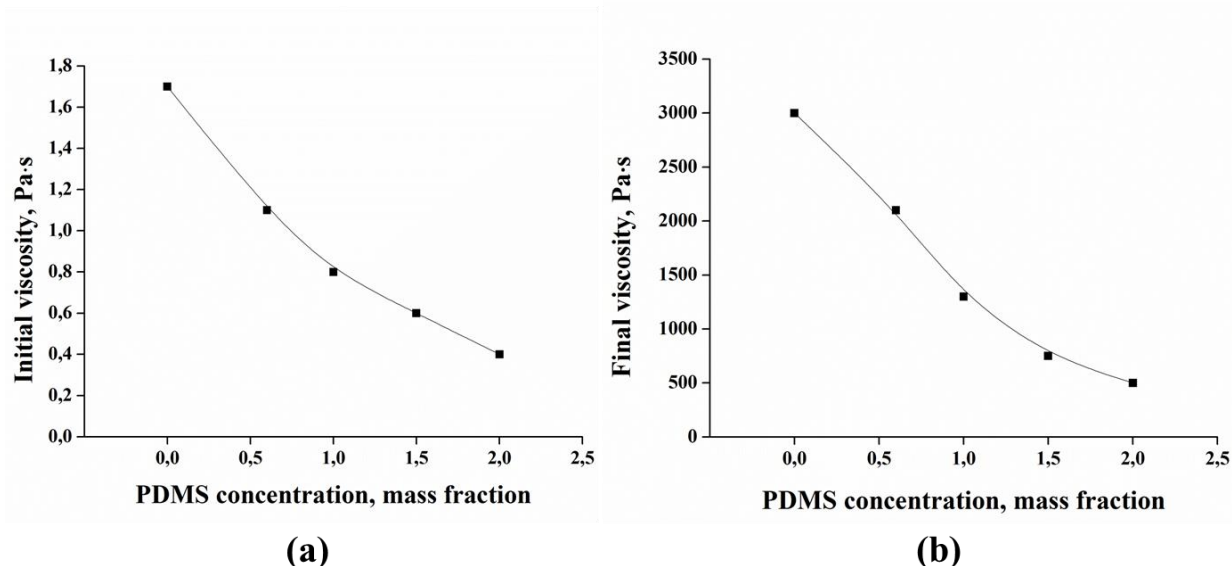


Figure 60. Effect of PDMS concentration on (a) initial viscosity and (b) final viscosity of the composite.

Effect of magnetic filler concentration on rheological properties of composite

To verify the effect of the filler concentration on the rheological properties of the composite, the composition with 2, 5, 7 and 14 wt. % of maghemite NPs were investigated (Table 15). Table 15 shows that the maghemite filler concentration within the tested range has a minor effect on the rheological properties of the composites.

Table 15. Effect of filler concentration on rheological properties of composite.

Concentration of NPs, wt. %	Relative concentration of the initial components, mass fraction				η^*_{in} , Pa·s	η^*_{fin} , Pa·s	t_{in} , min
	PVS	CAT	PHS	PDMS			
2	2.5	0.1	0.7	2.0	0.4	500	21
5	2.5	0.1	0.7	2.0	0.4	500	20
7	2.5	0.1	0.7	2.0	0.5	500	19
14	2.5	0.1	0.7	2.0	0.6	400	18

As a consequence, investigation of rheological properties of composites has shown that by adjusting the relative concentrations of the initial components it is possible to obtain embolic material with required rheological properties, i.e. low initial viscosity and the duration of induction period about 20 minutes after which the viscosity of the composite rapidly increases.

3.2.3. Radiopaque property of the composite

The radiopaque property is important for monitoring the position of mediator in the blood vessels. The composites were subjected to X-rays of the energy of 50 keV. To simulate the tissue layer, a 1.5-mm-thick aluminium plate was set before the samples, as is usually done in the radiopacity tests of materials (see ASTM F640 – Standard Test Methods for Determining Radiopacity for Medical Use). The images obtained for composites with different nanoparticles concentrations are shown in figure 61. For comparison, a pure silicon elastomer and the powders of maghemite nanoparticles and potassium iodide (a well-known radiopaque substance) were tested (Figure 61 a, g, h). The image histogram mean values obtained by processing the X-ray grayscale images of samples are shown in table 16.

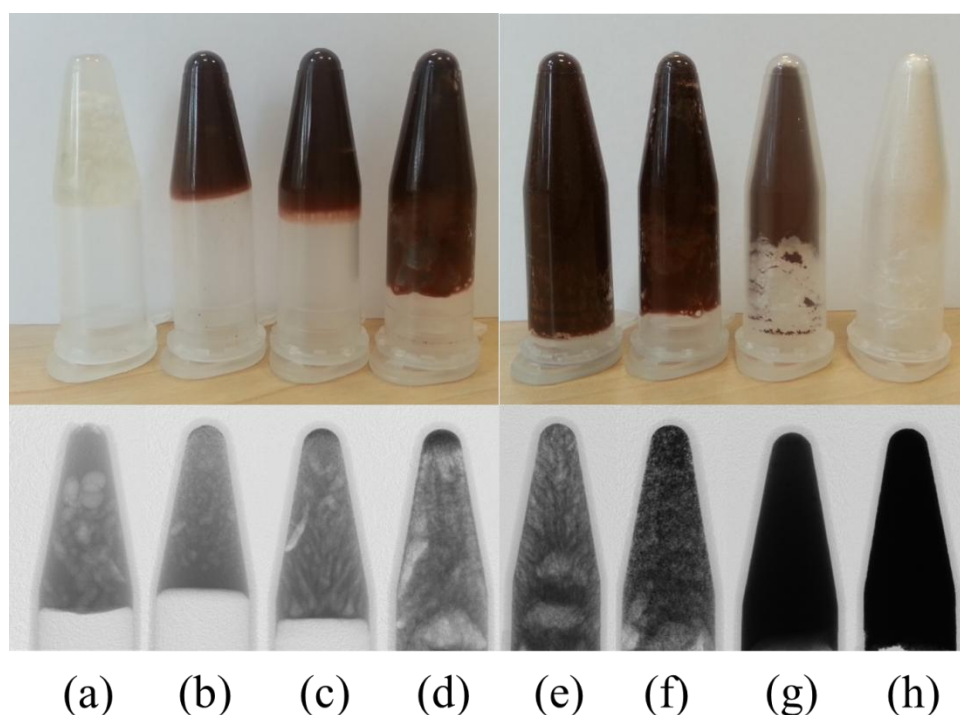


Figure 61. Photography and subsequent X-ray tomography images of (a) pure silicon elastomer and composites with, (b) 2 wt % of nanoparticles, (c) 5 wt % of nanoparticles, (d) 7 wt % of nanoparticles, (e) 14 wt. % of nanoparticles, (f) 7 wt % of nanoparticles and 7 wt. % of potassium iodide, and powders of (g) maghemite nanoparticles and (h) potassium iodide.

Table 16. The image histogram mean values obtained by processing the X-ray grayscale images of samples. Zero value denotes black colour and 255 denotes white colour.

Sample	Image histogram mean value
Silicone elastomer pure	136
Composite with 2 wt.% of maghemite	126
Composite with 5 wt.% of maghemite	119
Composite with 7 wt.% of maghemite	104
Composite with 14 wt.% of maghemite	89
Composite with 7 wt.% of maghemite and 7 wt.% of potassium iodide	55
Maghemite nanoparticles powder	17
Potassium iodide	6

The radiopaque property of the composites is attributed to the photoelectric absorption in atoms with high atomic numbers: I, Fe and Si. Presence of maghemite nanoparticles in concentration of 2 – 7 wt. % in the composite does not considerably enhance the radiopaque property (Figures 61 b, c, d and table 16). The X-ray contrast can be enhanced either by using a higher amount of magnetic filler, or by addition of potassium iodide in an amount that does not affected the rheological properties and the heating efficiency of the material (Figure 61 e, f). The X-ray contrast of the composite with 7wt. % of maghemite nanoparticles and addition of 7 wt. % of potassium iodide is higher than that for composite with 14 wt. % of maghemite nanoparticles.

3.2.4. Heating efficiency of the composite in AC magnetic field

In order to study the possibility of application of the obtained composite material as heat mediator in AEH the investigation of it's heating ability in AC magnetic fields was conducted. The AC magnetic field frequency and amplitude were within the limits established in MH. The temperature increase of the composites with different concentration of maghemite nanoparticles at different AC magnetic fields is displayed in figure 62. The heating rates of the composite at different AC magnetic fields are listed in table 17.

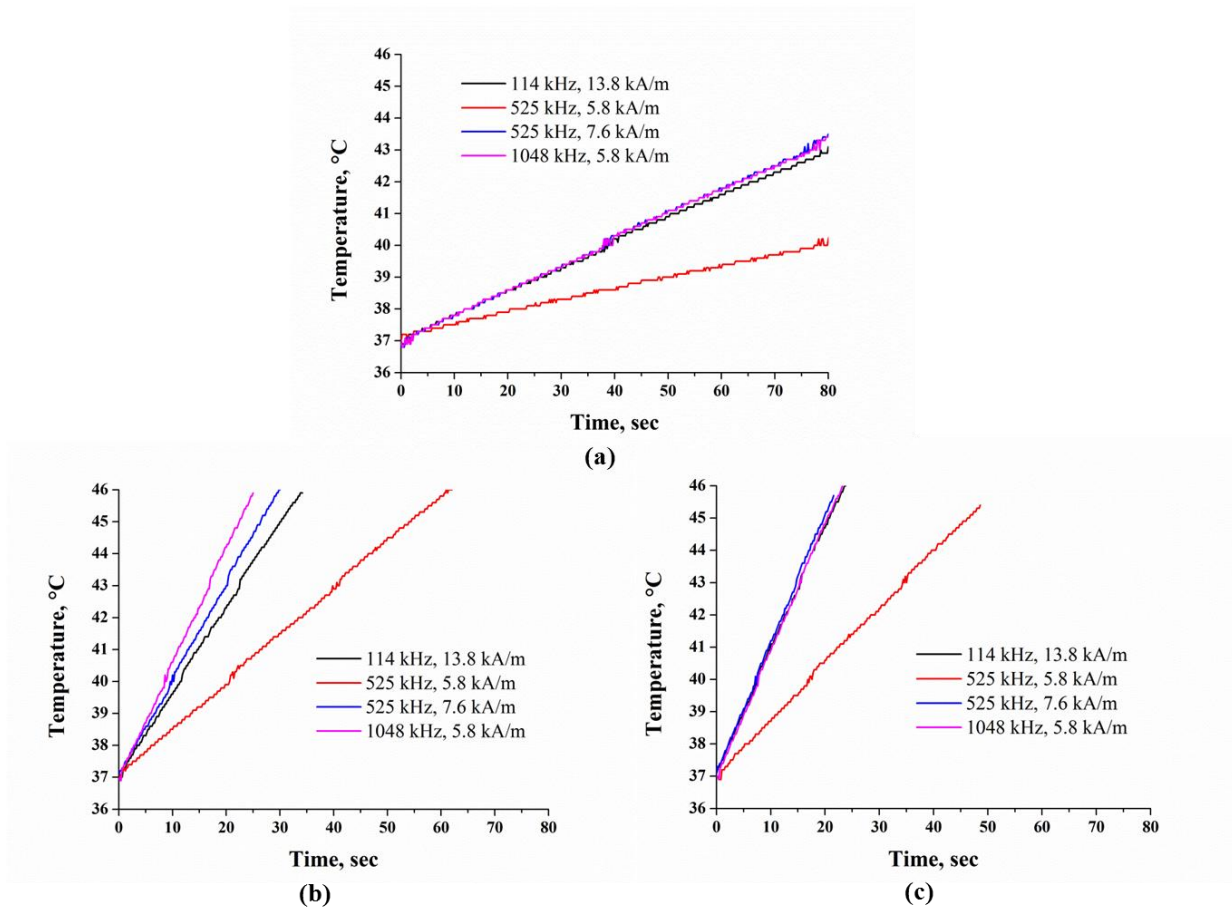


Figure 62. Inductive heating of composite with (a) 2 wt. % of nanoparticles, (b) 5 wt. % of nanoparticles, (c) 7 wt. % of nanoparticles at different AC magnetic field parameters.

Table 17. Heating rates in $^{\circ}\text{C}\cdot\text{min}^{-1}$ of composites with different concentrations of nanoparticles in AC magnetic fields of various frequencies and amplitudes.

Heating rate of composite, $^{\circ}\text{C}\cdot\text{min}^{-1}$						
AC magnetic field	f , kHz	114 kHz		525 kHz		1048 kHz
	H , $\text{kA}\cdot\text{m}^{-1}$	13.8 $\text{kA}\cdot\text{m}^{-1}$	5.8 $\text{kA}\cdot\text{m}^{-1}$	7.6 $\text{kA}\cdot\text{m}^{-1}$	5.8 $\text{kA}\cdot\text{m}^{-1}$	5.8 $\text{kA}\cdot\text{m}^{-1}$
Silicone magnetic composite	2 wt. %	5	3	5	5	5
	5 wt. %	16	9	17	21	21
	7 wt. %	24	12	24	24	24

As it is seen from figure 62 and table 17 the obtained composites provide a rapid heating in all applied AC magnetic fields. The heating rate increases with the

increase of nanoparticles concentration. The calculated SLP values according to equation (18) (section 1.4.2.) are represented in table 18. These values are lower than that obtained for glycerol dispersions of nanoparticles (table 12, section 3.1.4.). Moreover, while for glycerol dispersions the SLP increases with nanoparticles concentration, for composites SLP stays the same regardless the nanoparticles concentration. This difference is determined by the value of the viscosity of the dispersion medium. Since the viscosity of glycerol is lower than for silicone and decreases considerably from 1.41 Pa·s at 20 °C to 0.142 Pa·s at 50 °C, more probably, the regions with low viscosity appear in the vicinity of the nanoparticles surface during heating. The low viscosity favors the Brown relaxation, whose contribution to SLP increases with the nanoparticles concentration. Contrariwise, the viscosity of the silicone matrix does not change with temperature; therefore, the heat loss in such a system is determined solely by the Néel relaxation, and the SLP is constant regardless of the nanoparticles concentration.

Table 18. SLP values in $W \cdot g^{-1}$ of composites with different concentrations of nanoparticles in AC magnetic fields of various frequencies and amplitudes.

SLP, $W \cdot g^{-1}$					
AC magnetic field	f , kHz	114 kHz	525 kHz		1048 kHz
	H , $kA \cdot m^{-1}$	13.8 $kA \cdot m^{-1}$	5.8 $kA \cdot m^{-1}$	7.6 $kA \cdot m^{-1}$	5.8 $kA \cdot m^{-1}$
Silicone magnetic composite	2 wt.%	7.9 ± 1.3	3.5 ± 0.9	7.4 ± 0.9	8.0 ± 1.6
	5 wt.%	7.7 ± 1.7	4.2 ± 0.4	8.3 ± 0.6	9.7 ± 0.7
	7 wt.%	8.6 ± 0.1	4.3 ± 0.4	8.6 ± 1.0	9.0 ± 1.5

Recent theoretical study by Raikher et al. estimated for a model of maghemite nanoparticles of 13 nm average size and polydispersity, $\sigma = 0.3$, dispersed in a medium of viscosity higher than 0.01 Pa·s, that maximum SLP value is about 50 $W \cdot g^{-1}$ at AC magnetic field of 500 kHz and 7.96 $kA \cdot m^{-1}$ [15]. Taking into account that the calculations based on a constant value of anisotropy constant significantly overestimate the expected heating [171], it is possible to conclude, that the obtained SLP values of 4, 8 $W \cdot g^{-1}$ in the silicone magnetic composite at low field amplitudes belong to maximum possible for such type of material.

CONCLUSIONS

1. Uniform magnetic iron oxide nanoparticles with the size corresponding to SD state are obtained by coprecipitation method. Reaction conditions were established that provide homogeneous nucleation followed by slow particles growth and guarantee the repeatability of magneto-structural properties of nanoparticles. The stability of magnetic properties over time is ensured by complete oxidation of magnetite to maghemite via annealing at 300 °C in air.

2. The obtained nanoparticles demonstrate high heating rate in viscous media (tens of °C min⁻¹) which is explained by increased value of effective magnetic anisotropy due to magnetic interparticle interactions.

3. Maghemite silicone composite was elaborated possessing a set of properties required for use as a mediator in AEH: ability for secure embolization of the tumour blood vessels, radiopaque property and high heating rate in AC magnetic fields allowed for medical applications.

4. The possibility of secure embolization was achieved by optimization of composition to provide low initial viscosity allowing to deliver and to distribute the material uniformly in tumour's blood vessels, and 15 – 20 minutes induction period after which the viscosity of the composite rapidly increases forming a soft emboli.

5. The radiopaque property of composite was ensured by addition of 7 wt. % of potassium iodide.

6. The high heating rate (tens of °C·min⁻¹) of composite was reached at low concentration of maghemite nanoparticles (2–7 wt. %).

7. The SLP value of composite is determined by magneto-structural properties of nanoparticles as well as on the viscosity and specific heat capacity of dispersion medium. High viscosity of silicone limited the SLP value as solely Néel relaxation accounted for magnetic losses. Therefore the achieved SLP of 8 W·g⁻¹ in AC magnetic field with low amplitude belongs to maximal attainable for such type of systems.

FUTURE PROSPECTS

The first steps towards practical application are the *in-vitro* tests of obtained magnetic nanoparticles and mediators based on thereof. The impact of the mediator on cell viability under exposure to the AC magnetic field has to be studied.

AUTHOR'S CURRICULUM VITAE

Personal information

Surname(s) / First name(s): Ilona Sergeevna Smolková (Stepanova)
Telephone(s): +420 57 603 8112,
E-mail: smolkova@ft.utb.cz
Date of birth: 2nd September 1986
Nationality: Russian

Education and training

Dates: October 2009 - present
Title of qualification awarded: Ph.D. study
University: Tomas Bata University in Zlín,
Faculty of Technology, Polymer Centre

Dates: 2007 - 2009
Title of qualification awarded: M.Sc.
University: Saint-Petersburg State University,
Faculty of Chemistry,
Department of polymer chemistry

Dates: 2003 - 2007
Title of qualification awarded: Bc.
University: Saint-Petersburg State University,
Faculty of Chemistry.

Work experience

Dates: September 2013 – present
Position held: Junior researcher
Name of employer: Tomas Bata University in Zlín,
Centre of polymer systems

Dates: September 2011 – August 2013
Position held: Research project stuff
Name of employer: Tomas Bata University in Zlín,
Faculty of Technology

Dates: 2005 - 2009
Position held: Research staff
Name of employer: Institute of Macromolecular Compounds
Russian Academy of Sciences,
Saint-Petersburg, Russia

Projects

- 2012 IGA/FT/2012/033, Synthesis and characterization of iron oxide based nanocomposites for application in magnetic mediated hyperthermia, solver
- 2013 IGA/FT/2013/024, Electric and magnetic properties of multicomponent polymer systems, team member
- 2013 Participation in the preparation of the application for Standard GAČR project entitled: “Polymer magnetic gels with bi-functional properties for magnetically mediated hyperthermia and tumor vasculature embolization”
- 2014 Participation in the preparation of an application for Standard GAČR project entitled: “Optimized magnetic nanoparticles based dispersions for Magnetic Hyperthermia”

Publications before enrolment to Ph.D. study program

1. TROFIMOV, A. E., STEPANOVA, I.S., TENKOVTCHEV, A. V. New approach to the synthesis of organic-inorganic nanocomposites. *Russian Journal of Applied Chemistry*. 2007, Vol. 80, Issue 4, pp. 615-618.
2. GOFMAN, I. V., SUKHANOVA, T. E., VYLEGZHANINA, M. E., ABALOV, I. V., STEPANOVA, I. S., TROFIMOV, A. E., TENKOVTCHEV, A. V. Aliphatic polyurethane-silica nanocomposites prepared by the parallel synthesis: Morphology and mechanical characteristics. *Physics of the Solid State*. 2010, Vol. 52, Issue 3, pp 612-619.

Manuscripts prepared during the Ph.D. study

1. SMOLKOVA I. S., KAZANTSEVA N. E., PARMAR H., BABAYAN V., SMOLKA P., SAHA P. Correlation between coprecipitation reaction course and magneto-structural properties of iron oxide nanoparticles. Submitted to Materials Chemistry and Physics, manuscript number MATCHEMPHYS-D-14-00333, status on 13th of June – submission needs revision.

2. SMOLKOVA I. S., KAZANTSEVA N. E., BABAYAN V., SMOLKA P., PARMAR H., VILCAKOVA J., SCHNEEWEISS O., PIZUROVA N. Alternating magnetic field energy absorption in the dispersion of iron oxide nanoparticles in a viscous medium. Submitted to Journal of Magnetism and Magnetic Materials, manuscript number MAGMA-D-14-00540, status on 13th of June – submission needs revision.

3. SMOLKOVA I. S., KAZANTSEVA N. E., MAKOVECKAYA K. N., SMOLKA P., SAHA P., GRANOV A. M. Maghemite based silicone composite for arterial embolization hyperthermia. Submitted to Materials Science and Engineering C, manuscript number MSEC-S-14-00919, status on 13th of June – under review.

4. PARMAR H., SMOLKOVA I. S., KAZANTSEVA, N. E., BABAYAN, V., PASTOREK M., PIZUROVA N. Heating efficiency of iron oxide nanoparticles in hyperthermia: effect of preparation conditions. Manuscript accepted for publication in IEEE Transactions on Magnetics – Conferences.

Presentation at conferences

1. STEPANOVA I. S., KAZANTSEVA N. E., MOUCKA R., BABAYAN V., VILCAKOVA J., SAHA P. Iron oxide nanoparticles as heat mediators in magnetic-mediated hyperthermia. In: Plastko 2012, April 11th-12th 2012, Zlin, Czech Republic.

2. KAZANTSEVA N. E., STEPANOVA I. S., MOUCKA R., BABAYAN V., VILCAKOVA J., SAHA P. Iron oxides nanoparticles for magnetic mediated hyperthermia. In: Drug Delivery Devices, Medical Plastics, October 9th-10th 2012, Copenhagen, Denmark.

3. SMOLKOVA I. S., KAZANTSEVA N. E., MOUCKA R., BABAYAN V., VILCAKOVA J., SAHA P. Single-domain iron oxide nanoparticles for magnetically mediated hyperthermia. In: Mendeleev-2013, April 2th-5th 2013, Saint-Petersburg, Russia.

4. PARMAR H., SMOLKOVA I. S., KAZANTSEVA, N. E., BABAYAN, V., SMOLKA P., VILCAKOVA, J., SAHA, P. Heating efficiency of iron oxide

single domain nanoparticles prepared by different synthetic methods. In: Plastko 2014, April 8th-9th 2014, Zlin, Czech Republic.

5. PARMAR H., SMOLKOVA I. S., KAZANTSEVA, N. E., BABAYAN, V., PASTOREK M., PIZUROVA N. Heating efficiency of iron oxide nanoparticles in hyperthermia: effect of preparation conditions. In: INTERMAG 2014, May 4th-8th 2014, Dresden, Germany.

ABBREVIATIONS AND SYMBOLS

AC	Alternating
AEH	Arterial embolization hyperthermia
ATR	Attenuated total reflectance
CAT	Catalyst
CT	Computed Tomography
EDXRF	Energy dispersive X-ray fluorescence
FC	Field-cooled
FTIR	Fourier transform infrared spectroscopy
HRTEM	High resolution transmission electron microscopy
ICSD	Inorganic Crystal Structure Database
MD	Multidomain
MH	Magnetic hyperthermia
MRI	Magnetic Resonance Imaging
MS	Mössbauer spectre
NFR	Natural ferromagnetic resonance
PDMS	Poly(dimethylsiloxane)
PHS	Poly(dimethylsiloxane-co-methylhydrosiloxane)
PVS	Poly(dimethylsiloxane-co-methylvinylsiloxane)
RF	Radio frequency
SAED	Selected area diffraction
SAR	Specific absorption rate
SD	Single-domain
SEM	Scanning electron microscopy
SHP	Specific heating power
SLP	Specific loss power, frequency
SPM	Superparamagnetic
SQUID	Superconducting quantum interference device
SSD	Stable single-domain
TEM	Transmission electron microscopy
VSM	Vibrating Sample Magnetometer
XRD	X-Ray diffraction
ZFC	Zero-field-cooled

A	Exchange stiffness constant
A_f	Atomic fraction of the component in the Mössbauer spectrum
B	Magnetic induction
B_{hf}	Hyperfine field
c	Heat capacity
c_i	Specific heat capacity
D	Diameter of induced current loop
$D_{\text{cr}}^{\text{SD}}$	Critical diameter of single domain state
$D_{\text{cr}}^{\text{SPM}}$	Critical diameter of superparamagnetic state
d_{hkl}	Interplanar lattice spacing
d_{TEM}	Average particle size determined by TEM
d_{XRD}	Average crystallite size determined by XRD
dw	Contribution of domain-wall motion to the complex magnetic permeability
f	Frequency of alternating magnetic field
f_r	Resonance frequency
H	Magnetic field strength
H	Amplitude of alternating magnetic field
H_0	Stationary magnetic field
H_c	Coercive field, coercivity
H_s	Saturation field
I_s	Isomer shift
K_A	Magnetic anisotropy constants
k_B	Boltzmann constant
l_{ex}	Exchange length
M	Magnetization of a material
M_s	Saturation magnetization
M_r	Remanent magnetization
m	Mass
mr	Contribution of magnetization rotation to the complex magnetic permeability
P_b	Rate of heat loss per unit volume due to the blood flow
P_c	Rate of heat loss per unit volume due to thermal conduction
P_m	Metabolic heating rate
Q	Heat
Q_s	Quadrupole splitting
T	Temperature

T_B	Blocking temperature
T_C	Curie temperature
T_{ir}	Irreversibility point of ZFC and FC curves divergence
T_{max}	Maximum on the ZFC curve
T_N	Nèel temperature
t	time
t_{in}	Induction period time
t_{meas}	Measurement time
ΔU	Change of internal energy of a system
V	Volume of a particle
V_{hydr}	Hydrodynamic volume of a particle
W	Work
W_{ab}	Absorbed energy
δ_0	Domain wall width
ε	Crystal lattice strain
θ	Bragg angle
λ	Wavelength of electromagnetic radiation
μ'	Imaginary part of the complex permeability, magnetic losses
μ''	Real part of complex magnetic permeability
μ_0	Magnetic permeability of vacuum
μ_B	Bohr magneton
ρ	Mass density of a magnetic material
σ	Polydispersity index
τ	Effective relaxation time
τ_B	Brown relaxation time
τ_N	Néel relaxation time
χ	Magnetic susceptibility
χ''	Imaginary part of magnetic materials susceptibility
χ_a	Initial magnetic susceptibility
χ_{max}	Maximal magnetic susceptibility
η	Viscosity of a carrier medium
η_{fin}^*	Final viscosity of composite
η_{in}^*	Initial viscosity of composite

LIST OF FIGURES

Figure 1. Properties of diamagnetic material: (a) dependence of magnetization on external magnetic field strength, (b) temperature dependence of magnetic susceptibility. p. 11

Figure 2. Properties of paramagnetic material: (a) dependence of magnetization on external magnetic field strength, (b) temperature dependence of magnetic susceptibility. p. 12

Figure 3. Alignment of individual atomic magnetic moments in different types of materials. p. 12

Figure 4. Schematic representation of domain structure of magnetic materials. p.13

Figure 5. Initial magnetization curve. p. 14

Figure 6. Initial magnetization curve and hysteresis loop for ordered magnetic material. Adapted from [5]. p. 15

Figure 7. Schematic illustration of the size effect on the magnetic state of material on its coercivity. Solid curve coercivity dependence for non-interacting particles. Dashed line for particles with coupling between them. Modified from [7]. p.17

Figure 8. Calculated Néel and Brown relaxation times over a range of particle sizes for a water-based magnetite ferrofluid. Adapted from [13]. p.19

Figure 9. Magnetization curves of SD nanoparticles (red line) and of SPM nanoparticles (green line). p. 20

Figure 10. Magnetite crystal structure: (a) Magnetite unit cell. White atoms are oxygen, blue and green represent iron - different colours for tetrahedral and octahedral sites respectively; modified from [25]; (b) Iron polyhedra network (blue tetrahedra and green octahedra) in magnetite unit cell. p. 22

Figure 11. Schematic representation of the overlapping of $\text{Fe}^{2+} / \text{Fe}^{3+}$ cations and O^{2-} anion $3d$ - and $2d$ - orbitals. p.24

Figure 12. Schematic representation of ferrimagnetic ordering in magnetite. p. 25

Figure 13. Schematic representation of ferrimagnetic ordering in maghemite. p. 25

Figure 14. TEM image of (a) whole magnetotactic bacteria *Magnetospirillum magneticum* AMB-1, (b) extracted magnetosomes. The arrow denotes the external magnetic field direction. Adapted from [37]. p. 27

Figure 15. Cell cycle of a normal mammalian cell. p. 33

Figure 16. Polarization of atom: (a) atom in the absence of electric field; (b) formation of electric dipole in non-zero electric field. p. 36

Figure 17. Capacitive applicator: (a) schematic representation; (b) Thermotron RF-8. Adapted from [76]. p. 37

Figure 18. Microwave applicator: (a) schematic representation; (b) custom-built Lucite Cone waveguide applicator; (c) commercially available BSD – 2000 system (BSD Medical Corporation, Salt Lake City, Utah). Adapted from [72, 76]. p.38

Figure 19. Schematic representation of inductive heating applicator. Adapted from [76]. p. 39

Figure 20. Sketch of the first prototype of inductive heating system (MFH Hyperthermie systeme GmbH, Berlin, Germany). Adapted from [80]. p. 40

Figure 21. Particle size dependence of SLP at 500 kHz in a model single core maghemite nanoparticles under variation of the carrier medium viscosity: (1) $\eta = 10$ P, (2) 0.1 P, (3) 0.02 P, (4) 0.01 P, (5) 0.005 P. Adapted from [15]. p.47

Figure 22. Photographs of hamsters bearing osteosarcoma at 20 day of the study [118]: (a) treated by MH with magnetic cationic liposomes, (b) control group, untreated hamster. p. 52

Figure 23. (a) CT images showing magnetic nanoparticle deposition as hyperdense areas. Isothermal lines indicate calculated treatment temperatures between 40 °C (blue line) and 50 °C (red line). The brown line represents the tumor area; (b) 3-D reconstruction of fused MRI and CT showing the tumor (brown region), magnetic fluid (blue region) and thermometry catheter (green line). Adapted from [120]. p. 53

- Figure 24. Schematic representation of the setting for the iron oxide nanoparticles synthesis. p. 60
- Figure 25. Schematic representation of magnetic polymer composite preparation. p. 62
- Figure 26. X-Ray powder diffractograms of bulk magnetic iron oxides: magnetite and maghemite. Adapted from [24]. p. 65
- Figure 27. Schematic representation of electron energy transition: (a) initial state, (b) incident photon or electron ejects the 1s electron shell of the atom, (c) X-Ray emission when 2s electron fills the hole. p. 66
- Figure 28. ATR principle. p. 67
- Figure 29. Graphical representation of the MS. p. 68
- Figure 30. Room temperature spectrum of magnetite fitted with two sextets [24]. p. 69
- Figure 31. Illustration of particle size effect on room temperature MSs of nanoparticles with size of (a) 150 nm, (b) 48 nm, (c) 11 nm, (d) 4 nm. p.70
- Figure 32. Schematic representation of measuring mechanism in Vibrating Sample Magnetometer. p. 71
- Figure 33. Temperature dependence of magnetic moment: FC and ZFC curves. Adapted from [150]. p. 72
- Figure 34. FC and ZFC curves for non-interacting nanoparticles with sizes of (a) 3 nm, (b) 5 nm, (c) 10 nm. Adapted from [151]. p. 73
- Figure 35. Response of magnetic material in AC field: the induction, \mathbf{B} , lags in phase behind the applied field, \mathbf{H} . p. 74
- Figure 36. Schematic representation of measuring system. p. 75
- Figure 37. Variation of pH in the reaction medium during coprecipitation. p. 80
- Figure 38. Microscopy of samples. Sample I: (a) – HRSEM, (b) – TEM, (c) – particle size distribution. Sample II: (d) – SEM, (e) – TEM, (f) – particle size distribution. p. 80

Figure 39. HRTEM of nanoparticles of (a) Sample I and (b) Sample II.

p. 80

Figure 40. XRD patterns of samples obtained by two different coprecipitation reaction courses.

p. 81

Figure 41. Magnetization curves for Sample I and Sample II. Insets: (a) magnetization at low magnetic fields, (b) magnetization at high magnetic fields.

p. 83

Figure 42. Complex permeability spectra of (a) bulk magnetite and of obtained nanoparticles: (b) Sample I, (c) Sample II. The experimental values of μ' and μ'' are indicated by open squares. The colored solid lines show the total calculated permeability (red) obtained by combining the domain-wall motion (green) and magnetization rotation (blue) components.

p. 84

Figure 43. Heating rate of (a) Sample I and (b) Sample II dispersed in glycerol (2 wt. % of nanoparticles) for given frequency and amplitude of AC magnetic field.

p. 85

Figure 44. Coprecipitation reaction course: alkali solution is added to the salts solution. Modified from [160].

p. 87

Figure 45. Parallel reaction of magnetite formation on addition of alkali to the salts solution.

p. 87

Figure 46. Coprecipitation reaction course: salts solution is added to the alkali solution.

p. 88

Figure 47. Variation of saturation magnetization during coprecipitation reaction.

p. 89

Figure 48. The dependence of crystallite size on the reaction time for Sample II. Black dots are the experimental values of crystallite size, measured from the peak broadening of XRD patterns. The solid red line shows the fitting of experimental results by a logarithmic function.

p. 90

Figure 49. TEM images of (a) 2 h annealed sample and (b) 6 h annealed sample.

p. 92

Figure 50. XRD patterns of (a) original sample, (b) 2 h annealed sample, (c) 6 h annealed sample.

p. 93

Figure 51. HRTEM images with fast Fourier transformation of the (a, b) original sample, and (c) 2 h annealed sample. p. 94

Figure 52. Magnetization curves at room temperature for the original and annealed samples. The inset shows the central area of the loops at higher magnification. p. 96

Figure 53. Permeability spectra: (a) original sample, (b) 2 h annealed sample and (c) 6 h annealed sample. The experimental values of μ' and μ'' are indicated by open squares. The coloured solid lines show the total permeability calculated with regard to the contributions of domain wall motion (**dw**) and magnetization rotation (**mr**). p. 97

Figure 54. Mössbauer spectra: (a, b) of the original sample (c, d) of the 2 h annealed sample at 293 K and at 5 K. p.98

Figure 55. FC (pink) and ZFC (green) curves of the original sample for different intensities of the external magnetic field. p. 100

Figure 56. Inductive heating of iron oxide nanoparticles dispersions: (a) of original sample, (b) of 2h annealed sample, and (c) of 6 h annealed sample at AC magnetic field of $7.6 \text{ kA}\cdot\text{m}^{-1}$ alternating at 525 kHz. p. 101

Figure 57. FTIR spectra of (a) PHS and (b) silicone magnetic composite. p. 106

Figure 58. Kinetics of the composite formation. p. 107

Figure 59. Dependence of induction period time on PHS concentration at constant concentration of the other components of the mixture. p. 108

Figure 60. Effect of PDMS concentration on (a) initial viscosity and (b) final viscosity of the composite. p. 110

Figure 61. Photography and subsequent X-ray tomography images of (a) pure silicon elastomer and composites with, (b) 2 wt % of nanoparticles, (c) 5 wt % of nanoparticles, (d) 7 wt % of nanoparticles, (e) 14 wt. % of nanoparticles, (f) 7 wt % of nanoparticles and 7 wt. % of potassium iodide, and powders of (g) maghemite nanoparticles and (h) potassium iodide. p. 111

Figure 62. Inductive heating of composite with (a) 2 wt. % of nanoparticles, (b) 5 wt. % of nanoparticles, (c) 7 wt. % of nanoparticles at different AC magnetic field parameters. p. 113

LIST OF TABLES

- Table 1. Characteristic magnetic lengths for magnetite. p. 24
- Table 2. Classification of hyperthermia modalities according to heating principle and applied AC field. p. 35
- Table 3. Comparison of normal tissue and tumor conductivity at different frequencies of AC magnetic field. p. 39
- Table 4. Examples of experimental SLP data and corresponding ILP values of iron oxides nanoparticles at different AC magnetic fields. d is average particle diameter, for multicore nanoparticles hydrodynamic radius and in brackets the size of the nanocrystals forming the aggregate. p. 51
- Table 5. Hyperfine parameters for magnetite, nonstoichiometric magnetite and maghemite at room temperature [147]. All quadrupole splittings are close to zero. p. 69
- Table 6. Specific heat capacities and viscosities of commonly applied in hyperthermia dispersion mediums and of living matters. p. 76
- Table 7. Structural and magnetic properties of obtained iron oxides nanoparticles, and bulk magnetite and maghemite reported in [24, 162]. p. 82
- Table 8. SLP of Sample I and Sample II dispersed in glycerol (2 wt. % of nanoparticles). p. 86
- Table 9. Effect of reaction time on the structural parameters of the reaction intermediates of Sample II determined from XRD pattern analysis. p. 90
- Table 10. Structural and magnetic properties of iron oxides nanoparticles. p. 95
- Table 11. Mössbauer parameters of samples at 293 K and 5 K. A_f is the atomic fraction of the component in the MS. p. 99
- Table 12. SLP values of nanoparticles dispersions (2 wt. %, 5 wt. % and 7 wt.%) in glycerol in AC magnetic fields of various frequencies and amplitudes. p. 102
- Table 13. Effect of PHS concentration on rheological properties of the composite. p. 108

Table 14. Effect of plasticizer concentration on rheological properties of composite. p. 109

Table 15. Effect of filler concentration on rheological properties of composite. p. 110

Table 16. The image histogram mean values obtained by processing the X-ray grayscale images of samples. Zero value denotes black color and 255 denotes white color. p. 112

Table 17. Heating rates in $^{\circ}\text{C}\cdot\text{min}^{-1}$ of composites with different concentrations of nanoparticles in AC magnetic fields of various frequencies and amplitudes. p. 113

Table 18. SLP values in $\text{W}\cdot\text{g}^{-1}$ of composites with different concentrations of nanoparticles in AC magnetic fields of various frequencies and amplitudes. p. 114

REFERENCES

- [1] J. Smit, H.P.J. Wijn, Ferrites: physical properties of ferrimagnetic oxides in relation to their technical applications, Philips Technical Library, [Eindhoven], 1959.
- [2] S.s. Chikazumi, C.D. Graham, Physics of ferromagnetism, 2nd ed., Clarendon Press, Oxford, 1997.
- [3] J.M.D. Coey, Magnetism and magnetic materials, Cambridge University Press, Cambridge, UK ; New York, 2010.
- [4] J.B. Goodenough, Atomic Moments and Magnetic Coupling in Cation Excess-Nickel Arsenides, J Appl Phys, 34 (1963) 1193.
- [5] S. Thomas, Polymer composites, Wiley-VCH, Weinheim, 2012.
- [6] A.P. Guimaraes, Principles of nanomagnetism, Springer, Berlin Heidelberg, 2009.
- [7] U. Jeong, X.W. Teng, Y. Wang, H. Yang, Y.N. Xia, Superparamagnetic colloids: Controlled synthesis and niche applications, Adv Mater, 19 (2007) 33-60.
- [8] R.A. McCurrie, Ferromagnetic materials: structure and properties, Academic Press, 1994.
- [9] R. Skomski, Nanomagnetism, J Phys-Condens Mat, 15 (2003) R841-R896.
- [10] S.A. Majetich, M. Sachan, Magnetostatic interactions in magnetic nanoparticle assemblies: energy, time and length scales, J Phys D Appl Phys, 39 (2006) R407-R422.
- [11] A.G. Kolhatkar, A.C. Jamison, D. Litvinov, R.C. Willson, T.R. Lee, Tuning the Magnetic Properties of Nanoparticles, Int J Mol Sci, 14 (2013) 15977-16009.
- [12] L. Neel, Influence Des Fluctuations Thermiques Sur Laimantation De Grains Ferromagnetiques Tres Fins, Cr Hebd Acad Sci, 228 (1949) 664-666.
- [13] P. O'Brien, V.S. Coker, Royal Society of Chemistry (Great Britain), Nanoscience. Volume 1, Nanostructures through chemistry: a review of recent literature.
- [14] S. Dutz, R. Hergt, Magnetic nanoparticle heating and heat transfer on a microscale: Basic principles, realities and physical limitations of hyperthermia for tumour therapy, Int J Hyperthermia, 29 (2013) 790-800.
- [15] Y.L. Raikher, V.I. Stepanov, Physical aspects of magnetic hyperthermia: Low-frequency ac field absorption in a magnetic colloid, J Magn Magn Mater, <http://dx.doi.org/10.1016/j.jmmm.2014.01.070> (2014).
- [16] J.-P. Jolivet, M. Henry, J. Livage, E.P. Bescher, Metal oxide chemistry and synthesis : from solution to solid state, John Wiley, Chichester, 2000.
- [17] M. Colombo, S. Carregal-Romero, M.F. Casula, L. Gutierrez, M.P. Morales, I.B. Bohm, J.T. Heverhagen, D. Prosperi, W.J. Parak, Biological applications of magnetic nanoparticles, Chem Soc Rev, 41 (2012) 4306-4334.
- [18] I. Hilger, W.A. Kaiser, Iron oxide-based nanostructures for MRI and magnetic hyperthermia, Nanomedicine-Uk, 7 (2012) 1443-1459.

- [19] M. Kawashita, M. Tanaka, T. Kokubo, Y. Inoue, T. Yao, S. Hamada, T. Shinjo, Preparation of ferrimagnetic magnetite microspheres for in situ hyperthermic treatment of cancer, *Biomaterials*, 26 (2005) 2231-2238.
- [20] K.M. Krishnan, Biomedical Nanomagnetism: A Spin Through Possibilities in Imaging, Diagnostics, and Therapy, *Ieee T Magn*, 46 (2010) 2523-2558.
- [21] P. Moroz, S.K. Jones, B.N. Gray, Magnetically mediated hyperthermia: current status and future directions, *Int J Hyperther*, 18 (2002) 267-284.
- [22] A.G. Roca, R. Costo, A.F. Rebolledo, S. Veintemillas-Verdaguer, P. Tartaj, T. Gonzalez-Carreno, M.P. Morales, C.J. Serna, Progress in the preparation of magnetic nanoparticles for applications in biomedicine, *J Phys D Appl Phys*, 42 (2009).
- [23] L. Trahms, Biomedical applications of magnetic nanoparticles, *Lect. Notes. Phys*, 763 (2009) 327-358.
- [24] R.M. Cornell, U. Schwertmann, *The iron oxides : structure, properties, reactions, occurrences, and uses*, 2nd, completely rev. and extended ed., Wiley-VCH, Weinheim, 2003.
- [25] J.L. Kirschvink, *Magnetite biomineralization and magnetoreception in organisms*, Mir, Moscow, 1989.
- [26] E. Murad, U. Schwertmann, Temporal Stability of a Fine-Grained Magnetite, *Clay Clay Miner*, 41 (1993) 111-113.
- [27] W. Baaziz, B.P. Pichon, S. Fleutot, Y. Liu, C. Lefevre, J.M. Greneche, M. Toumi, T. Mhiri, S. Begin-Colin, Magnetic Iron Oxide Nanoparticles: Reproducible Tuning of the Size and Nanosized-Dependent Composition, Defects, and Spin Canting, *J Phys Chem C*, 118 (2014) 3795-3810.
- [28] C. Vichery, I. Maurin, P. Bonville, J.P. Boilot, T. Gacoin, Influence of Protected Annealing on the Magnetic Properties of $\gamma\text{-Fe}_2\text{O}_3$ Nanoparticles, *J Phys Chem C*, 116 (2012) 16311-16318.
- [29] K.P. Belov, Mystery of magnetite, *International Soros Science Education Program*, 6 (2000) 71-76.
- [30] J.M.D. Coey, Noncollinear Spin Arrangement in Ultrafine Ferrimagnetic Crystallites, *Phys Rev Lett*, 27 (1971) 1140.
- [31] L.C. Varanda, M. Jafellici, P. Tartaj, K. O' Grady, T. Gonzalez-Carreno, M.P. Morales, T. Munoz, C.J. Serna, Structural and magnetic transformation of monodispersed iron oxide particles in a reducing atmosphere, *J Appl Phys*, 92 (2002) 2079-2085.
- [32] C.L. Dennis, R. Ivkov, Physics of heat generation using magnetic nanoparticles for hyperthermia, *Int J Hyperthermia*, 29 (2013) 715-729.
- [33] A.K. Gupta, M. Gupta, Synthesis and surface engineering of iron oxide nanoparticles for biomedical applications, *Biomaterials*, 26 (2005) 3995-4021.
- [34] A.S. Teja, P.Y. Koh, Synthesis, properties, and applications of magnetic iron oxide nanoparticles, *Prog Cryst Growth Ch*, 55 (2009) 22-45.

- [35] R. Hergt, R. Hiergeist, M. Zeisberger, D. Schuler, U. Heyen, I. Hilger, W.A. Kaiser, Magnetic properties of bacterial magnetosomes as potential diagnostic and therapeutic tools, *J Magn Magn Mater*, 293 (2005) 80-86.
- [36] U. Heyen, D. Schuler, Growth and magnetosome formation by microaerophilic *Magnetospirillum* strains in an oxygen-controlled fermentor, *Appl Microbiol Biot*, 61 (2003) 536-544.
- [37] E. Alphantery, Y. Ding, A.T. Ngo, Z.L. Wang, L.F. Wu, M.P. Pileni, Assemblies of Aligned Magnetotactic Bacteria and Extracted Magnetosomes: What Is the Main Factor Responsible for the Magnetic Anisotropy?, *Acs Nano*, 3 (2009) 1539-1547.
- [38] R. Massart, Preparation of Aqueous Magnetic Liquids in Alkaline and Acidic Media, *Ieee T Magn*, 17 (1981) 1247-1248.
- [39] S. Dutz, R. Hergt, J. Murbe, R. Muller, M. Zeisberger, W. Andra, J. Topfer, M.E. Bellemann, Hysteresis losses of magnetic nanoparticle powders in the single domain size range, *J Magn Magn Mater*, 308 (2007) 305-312.
- [40] J. Murbe, A. Rechtenbach, J. Topfer, Synthesis and physical characterization of magnetite nanoparticles for biomedical applications, *Mater Chem Phys*, 110 (2008) 426-433.
- [41] K. Okawa, M. Sekine, M. Maeda, M. Tada, M. Abe, N. Matsushita, K. Nishio, H. Handa, Heating ability of magnetite nanobeads with various sizes for magnetic hyperthermia at 120 kHz, a noninvasive frequency, *J Appl Phys*, 99 (2006).
- [42] M. Racuciu, Synthesis protocol influence on aqueous magnetic fluid properties, *Curr Appl Phys*, 9 (2009) 1062-1066.
- [43] S. Dutz, J.H. Clement, D. Eberbeck, T. Gelbrich, R. Hergt, R. Muller, J. Wotschadlo, M. Zeisberger, Ferrofluids of magnetic multicore nanoparticles for biomedical applications, *J Magn Magn Mater*, 321 (2009) 1501-1504.
- [44] J.P. Fortin, C. Wilhelm, J. Servais, C. Menager, J.C. Bacri, F. Gazeau, Size-sorted anionic iron oxide nanomagnets as colloidal mediators for magnetic hyperthermia, *J Am Chem Soc*, 129 (2007) 2628-2635.
- [45] L.A. Thomas, L. Dekker, M. Kallumadil, P. Southern, M. Wilson, S.P. Nair, Q.A. Pankhurst, I.P. Parkin, Carboxylic acid-stabilised iron oxide nanoparticles for use in magnetic hyperthermia, *J Mater Chem*, 19 (2009) 6529-6535.
- [46] R. Hergt, R. Hiergeist, I. Hilger, W.A. Kaiser, Y. Lapatnikov, S. Margel, U. Richter, Maghemite nanoparticles with very high AC-losses for application in RF-magnetic hyperthermia, *J Magn Magn Mater*, 270 (2004) 345-357.
- [47] L. Lartigue, P. Hugounenq, D. Alloyeau, S.P. Clarke, M. Levy, J.C. Bacri, R. Bazzi, D.F. Brougham, C. Wilhelm, F. Gazeau, Cooperative Organization in Iron Oxide Multi-Core Nanoparticles Potentiates Their Efficiency as Heating Mediators and MRI Contrast Agents, *Acs Nano*, 6 (2012) 10935-10949.
- [48] A.B. Chin, I.I. Yaacob, Synthesis and characterization of magnetic iron oxide nanoparticles via w/o microemulsion and Massart's procedure, *J Mater Process Tech*, 191 (2007) 235-237.

- [49] A.L. Loo, M.G. Pineda, H. Saade, M.E. Trevino, R.G. Lopez, Synthesis of magnetic nanoparticles in bicontinuous microemulsions. Effect of surfactant concentration, *J Mater Sci*, 43 (2008) 3649-3654.
- [50] Z.H. Zhou, J. Wang, X. Liu, H.S.O. Chan, Synthesis of Fe₃O₄ nanoparticles from emulsions, *J Mater Chem*, 11 (2001) 1704-1709.
- [51] A.K. Gupta, S. Wells, Surface-modified superparamagnetic nanoparticles for drug delivery: Preparation, characterization, and cytotoxicity studies, *Ieee T Nanobiosci*, 3 (2004) 66-73.
- [52] T. Hyeon, S.S. Lee, J. Park, Y. Chung, H. Bin Na, Synthesis of highly crystalline and monodisperse maghemite nanocrystallites without a size-selection process, *J Am Chem Soc*, 123 (2001) 12798-12801.
- [53] J. Park, E. Lee, N.M. Hwang, M.S. Kang, S.C. Kim, Y. Hwang, J.G. Park, H.J. Noh, J.Y. Kim, J.H. Park, T. Hyeon, One-nanometer-scale size-controlled synthesis of monodisperse magnetic iron oxide nanoparticles, *Angew Chem Int Edit*, 44 (2005) 2872-2877.
- [54] K. Woo, J. Hong, S. Choi, H.W. Lee, J.P. Ahn, C.S. Kim, S.W. Lee, Easy synthesis and magnetic properties of iron oxide nanoparticles, *Chem Mater*, 16 (2004) 2814-2818.
- [55] J. Rockenberger, E.C. Scher, A.P. Alivisatos, A new nonhydrolytic single-precursor approach to surfactant-capped nanocrystals of transition metal oxides, *J Am Chem Soc*, 121 (1999) 11595-11596.
- [56] S.H. Sun, H. Zeng, Size-controlled synthesis of magnetite nanoparticles, *J Am Chem Soc*, 124 (2002) 8204-8205.
- [57] N.R. Jana, Y.F. Chen, X.G. Peng, Size- and shape-controlled magnetic (Cr, Mn, Fe, Co, Ni) oxide nanocrystals via a simple and general approach, *Chem Mater*, 16 (2004) 3931-3935.
- [58] J. Park, K.J. An, Y.S. Hwang, J.G. Park, H.J. Noh, J.Y. Kim, J.H. Park, N.M. Hwang, T. Hyeon, Ultra-large-scale syntheses of monodisperse nanocrystals, *Nat Mater*, 3 (2004) 891-895.
- [59] T. Hyeon, Chemical synthesis of magnetic nanoparticles, *Chem Commun*, (2003) 927-934.
- [60] M. Levy, A. Quarta, A. Espinosa, A. Figuerola, C. Wilhelm, M. Garcia-Hernandez, A. Genovese, A. Falqui, D. Alloyeau, R. Buonsanti, P.D. Cozzoli, M.A. Garcia, F. Gazeau, T. Pellegrino, Correlating Magneto-Structural Properties to Hyperthermia Performance of Highly Monodisperse Iron Oxide Nanoparticles Prepared by a Seeded-Growth Route, *Chem Mater*, 23 (2011) 4170-4180.
- [61] Q.A. Pankhurst, N.T.K. Thanh, S.K. Jones, J. Dobson, Progress in applications of magnetic nanoparticles in biomedicine, *J Phys D Appl Phys*, 42 (2009).
- [62] A.G.J. Tibbe, B.G. de Grooth, J. Greve, P.A. Liberti, G.J. Dolan, L.W.M.M. Terstappen, Optical tracking and detection of immunomagnetically selected and aligned cells, *Nat Biotechnol*, 17 (1999) 1210-1213.

- [63] B.Y. Kularatne, P. Lorigan, S. Browne, S.K. Suvarna, N.O. Smith, J. Lawry, Monitoring tumour cells in the peripheral blood of small cell lung cancer patients, *Cytometry*, 50 (2002) 160-167.
- [64] R.E. Zigeuner, R. Riesenberger, H. Pohla, A. Hofstetter, R. Oberneder, Isolation of circulating cancer cells from whole blood by immunomagnetic cell enrichment and unenriched immunocytochemistry in vitro, *J Urology*, 169 (2003) 701-705.
- [65] C. Alexiou, W. Arnold, R.J. Klein, F.G. Parak, P. Hulin, C. Bergemann, W. Erhardt, S. Wagenpfeil, A.S. Lubbe, Locoregional cancer treatment with magnetic drug targeting, *Cancer Res*, 60 (2000) 6641-6648.
- [66] S.C. Goodwin, C.A. Bittner, C.L. Peterson, G. Wong, Single-dose toxicity study of hepatic intra-arterial infusion of doxorubicin coupled to a novel magnetically targeted drug carrier, *Toxicol Sci*, 60 (2001) 177-183.
- [67] S.K. Pulfer, S.L. Ciccotto, J.M. Gallo, Distribution of small magnetic particles in brain tumor-bearing rats, *J Neuro-Oncol*, 41 (1999) 99-105.
- [68] A.S. Lubbe, C. Bergemann, H. Riess, F. Schriever, P. Reichardt, K. Possinger, M. Matthias, B. Dorken, F. Herrmann, R. Gurtler, P. Hohenberger, N. Haas, R. Sohr, B. Sander, A.J. Lemke, D. Ohlendorf, W. Huhnt, D. Huhn, Clinical experiences with magnetic drug targeting: A phase I study with 4'-epidoxorubicin in 14 patients with advanced solid tumors, *Cancer Res*, 56 (1996) 4686-4693.
- [69] A.M. Granov, M.I. Davidov, *Interventional radiology in oncology: Ways of development and perspectives*, OOO "Publisher Foliant", Saint-Petersburg, 2007.
- [70] W. Bush, *Verhandlungen ärztlicher Gesellschaften, Klinische Wochenschrift*, 4 (1868) 1519-1525.
- [71] J. Bickels, Y. Kollender, O. Merinsky, I. Meller, Coley's toxin: Historical perspective, *Israel Med Assoc J*, 4 (2002) 471-472.
- [72] J. van der Zee, Heating the patient: a promising approach?, *Ann Oncol*, 13 (2002) 1173-1184.
- [73] A.v. Vorst, A. Rosen, Y. Kotsuka, *RF/microwave interaction with biological tissues*, Wiley :, Hoboken, N.J., 2006.
- [74] E.D.P. De Robertis, E.M.F. De Robertis, *Cell and molecular biology*, 8th ed., Lea & Febiger, Philadelphia, 1987.
- [75] J.L.R. Roti, Cellular responses to hyperthermia (40-46 degrees C): Cell killing and molecular events, *Int J Hyperther*, 24 (2008) 3-15.
- [76] G.F. Barozio, E.D. Hager, *Hyperthermia in cancer treatment: A primer*, Springer Science + Business Media, New York, 2011.
- [77] P. Moroz, S.K. Jones, B.N. Gray, Status of hyperthermia in the treatment of advanced liver cancer, *J Surg Oncol*, 77 (2001) 259-269.
- [78] S. Hammerschmidt, H. Wahn, P. Langmann, W. Scheppach, Acute liver failure after whole body hyperthermia treatment, *Deut Med Wochenschr*, 124 (1999) 1379-1382.
- [79] D. Haemmerich, S.T. Staelin, J.Z. Tsai, S. Tungjitkusolmun, D.M. Mahvi, J.G. Webster, In vivo electrical conductivity of hepatic tumours, *Physiol Meas*, 24 (2003) 251-260.

- [80] A. Jordan, R. Scholz, K. Maier-Hauff, M. Johannsen, P. Wust, J. Nadobny, H. Schirra, H. Schmidt, S. Deger, S. Loening, W. Lanksch, R. Felix, Presentation of a new magnetic field therapy system for the treatment of human solid tumors with magnetic fluid hyperthermia, *J Magn Magn Mater*, 225 (2001) 118-126.
- [81] R.K. Gilchrist, R. Medal, W.D. Shorey, R.C. Hanselman, J.C. Parrott, C.B. Taylor, Selective inductive heating of lymph nodes, *Ann Surg*, 146 (1957) 596-606.
- [82] A. Brezovich, Low frequency hyperthermia. Medical Physics Monograph, American Institute of Physics, New York, 1988.
- [83] S. Laurent, S. Dutz, U.O. Hafeli, M. Mahmoudi, Magnetic fluid hyperthermia: Focus on superparamagnetic iron oxide nanoparticles, *Adv Colloid Interfac*, 166 (2011) 8-23.
- [84] P.E. Le Renard, O. Jordan, A. Faes, A. Petri-Fink, H. Hofmann, D. Rufenacht, F. Bosman, F. Buchegger, E. Doelker, The in vivo performance of magnetic particle-loaded injectable, in situ gelling, carriers for the delivery of local hyperthermia, *Biomaterials*, 31 (2010) 691-705.
- [85] T. Kobayashi, Y. Kida, T. Tanaka, K. Hattori, M. Matsui, Y. Amemiya, Interstitial Hyperthermia of Malignant Brain-Tumors by Implant Heating-System - Clinical-Experience, *J Neuro-Oncol*, 10 (1991) 153-163.
- [86] A. Ito, M. Shinkai, H. Honda, T. Kobayashi, Medical application of functionalized magnetic nanoparticles, *J Biosci Bioeng*, 100 (2005) 1-11.
- [87] A. Jordan, P. Wust, H. Fahling, W. John, A. Hinz, R. Felix, Inductive heating of ferrimagnetic particles and magnetic fluids: Physical evaluation of their potential for hyperthermia, *Int J Hyperther*, 25 (2009) 499-511.
- [88] R.E. Rosensweig, Heating magnetic fluid with alternating magnetic field, *J Magn Magn Mater*, 252 (2002) 370-374.
- [89] D.E. Bordelon, C. Cornejo, C. Gruttner, F. Westphal, T.L. DeWeese, R. Ivkov, Magnetic nanoparticle heating efficiency reveals magneto-structural differences when characterized with wide ranging and high amplitude alternating magnetic fields, *J Appl Phys*, 109 (2011).
- [90] M.T. Thompson, Simple models and measurements of magnetically induced heating effects in ferromagnetic fluids, *Ieee T Magn*, 34 (1998) 3755-3764.
- [91] G. Margaris, K. Trohidou, H. Kachkachi, Surface effects on the magnetic behavior of nanoparticle assemblies, *Phys Rev B*, 85 (2012).
- [92] S.H. Noh, W. Na, J.T. Jang, J.H. Lee, E.J. Lee, S.H. Moon, Y. Lim, J.S. Shin, J. Cheon, Nanoscale Magnetism Control via Surface and Exchange Anisotropy for Optimized Ferrimagnetic Hysteresis, *Nano Lett*, 12 (2012) 3716-3721.
- [93] F. Heider, D.J. Dunlop, N. Sugiura, Magnetic-Properties of Hydrothermally Recrystallized Magnetite Crystals, *Science*, 236 (1987) 1287-1290.
- [94] A.S. Eggeman, S.A. Majetich, D. Farrell, Q.A. Pankhurst, Size and concentration effects on high frequency hysteresis of iron oxide nanoparticles, *Ieee T Magn*, 43 (2007) 2451-2453.

- [95] A. Urtizberea, E. Natividad, A. Arizaga, M. Castro, A. Mediano, Specific Absorption Rates and Magnetic Properties of Ferrofluids with Interaction Effects at Low Concentrations, *J Phys Chem C*, 114 (2010) 4916-4922.
- [96] R. Hergt, S. Dutz, Magnetic particle hyperthermia-biophysical limitations of a visionary tumour therapy, *J Magn Magn Mater*, 311 (2007) 187-192.
- [97] E. Pollert, P. Veverka, M. Veverka, O. Kaman, K. Zaveta, S. Vasseur, R. Epherre, G. Goglio, E. Duguet, Search of new core materials for magnetic fluid hyperthermia: Preliminary chemical and physical issues, *Prog Solid State Ch*, 37 (2009) 1-14.
- [98] E. Auzans, D. Zins, E. Blums, R. Massart, Synthesis and properties of Mn-Zn ferrite ferrofluids, *J Mater Sci*, 34 (1999) 1253-1260.
- [99] O. Bretcanu, E. Verne, M. Coisson, P. Tiberto, P. Allia, Magnetic properties of the ferrimagnetic glass-ceramics for hyperthermia, *J Magn Magn Mater*, 305 (2006) 529-533.
- [100] R. Sharma, C.J. Chen, Newer nanoparticles in hyperthermia treatment and thermometry, *J Nanopart Res*, 11 (2009) 671-689.
- [101] M.S. Seehra, V. Singh, P. Dutta, S. Neeleshwar, Y.Y. Chen, C.L. Chen, S.W. Chou, C.C. Chen, Size-dependent magnetic parameters of fcc FePt nanoparticles: applications to magnetic hyperthermia, *J Phys D Appl Phys*, 43 (2010).
- [102] T.N. Brusentsova, N.A. Brusentsov, V.D. Kuznetsov, V.N. Nikiforov, Synthesis and investigation of magnetic properties of Gd-substituted Mn-Zn ferrite nanoparticles as a potential low-T-C agent for magnetic fluid hyperthermia, *J Magn Magn Mater*, 293 (2005) 298-302.
- [103] O.A. Kuznetsov, O.N. Sorokina, V.G. Leontiev, O.A. Shlyakhtin, A.L. Kovarski, A.A. Kuznetsov, ESR study of thermal demagnetization processes in ferromagnetic nanoparticles with Curie temperatures between 40 and 60 degrees C, *J Magn Magn Mater*, 311 (2007) 204-207.
- [104] S.E. Barry, Challenges in the development of magnetic particles for therapeutic applications, *Int J Hyperther*, 24 (2008) 451-466.
- [105] M. Mahmoudi, S. Sant, B. Wang, S. Laurent, T. Sen, Superparamagnetic iron oxide nanoparticles (SPIONs): Development, surface modification and applications in chemotherapy, *Adv Drug Deliver Rev*, 63 (2011) 24-46.
- [106] H.L. Karlsson, P. Cronholm, J. Gustafsson, L. Moller, Copper oxide nanoparticles are highly toxic: A comparison between metal oxide nanoparticles and carbon nanotubes, *Chem Res Toxicol*, 21 (2008) 1726-1732.
- [107] M.A. Maurer-Jones, K.C. Bantz, S.A. Love, B.J. Marquis, C.L. Haynes, Toxicity of therapeutic nanoparticles, *Nanomedicine-Uk*, 4 (2009) 219-241.
- [108] V.I. Shubayev, T.R. Pisanic, S.H. Jin, Magnetic nanoparticles for theragnostics, *Adv Drug Deliver Rev*, 61 (2009) 467-477.
- [109] P. Guardia, R. Di Corato, L. Lartigue, C. Wilhelm, A. Espinosa, M. Garcia-Hernandez, F. Gazeau, L. Manna, T. Pellegrino, Water-Soluble Iron Oxide Nanocubes with High Values of Specific Absorption Rate for Cancer Cell Hyperthermia Treatment, *Acs Nano*, 6 (2012) 3080-3091.

- [110] M. Kallumadil, M. Tada, T. Nakagawa, M. Abe, P. Southern, Q.A. Pankhurst, Suitability of commercial colloids for magnetic hyperthermia, *J Magn Magn Mater*, 321 (2009) 1509-1513.
- [111] P.C. Fannin, Characterisation of magnetic fluids, *J Alloy Compd*, 369 (2004) 43-51.
- [112] A.T. Giannitsis, P.C. Fannin, S.W. Charles, Nonlinear effects in magnetic fluids, *J Magn Magn Mater*, 289 (2005) 165-167.
- [113] G. Glockl, R. Hergt, M. Zeisberger, S. Dutz, S. Nagel, W. Weitschies, The effect of field parameters, nanoparticle properties and immobilization on the specific heating power in magnetic particle hyperthermia, *J Phys-Condens Mat*, 18 (2006) S2935-S2949.
- [114] R. Hergt, S. Dutz, R. Muller, M. Zeisberger, Magnetic particle hyperthermia: nanoparticle magnetism and materials development for cancer therapy, *J Phys-Condens Mat*, 18 (2006) S2919-S2934.
- [115] A.P. Khandhar, R.M. Ferguson, J.A. Simon, K.M. Krishnan, Tailored magnetic nanoparticles for optimizing magnetic fluid hyperthermia, *J Biomed Mater Res A*, 100A (2012) 728-737.
- [116] R.T. Gordon, J.R. Hines, D. Gordon, Intracellular Hyperthermia - Biophysical Approach to Cancer-Treatment Via Intracellular Temperature and Biophysical Alterations, *Medical Hypotheses*, 5 (1979) 83-102.
- [117] R. Hergt, W. Andra, C.G. d'Ambly, I. Hilger, W.A. Kaiser, U. Richter, H.G. Schmidt, Physical limits of hyperthermia using magnetite fine particles, *Ieee T Magn*, 34 (1998) 3745-3754.
- [118] F. Matsuoka, M. Shinkai, H. Honda, T. Kubo, T. Sugita, T. Kobayashi, Hyperthermia using magnetite cationic liposomes for hamster osteosarcoma, *Biomagn Res Technol*, 2 (2004) 3.
- [119] K. Maier-Hauff, R. Rothe, R. Scholz, U. Gneveckow, P. Wust, B. Thiesen, A. Feussner, A. von Deimling, N. Waldoefner, R. Felix, A. Jordan, Intracranial thermotherapy using magnetic nanoparticles combined with external beam radiotherapy: Results of a feasibility study on patients with glioblastoma multiforme, *J Neuro-Oncol*, 81 (2007) 53-60.
- [120] K. Maier-Hauff, F. Ulrich, D. Nestler, H. Niehoff, P. Wust, B. Thiesen, H. Orawa, V. Budach, A. Jordan, Efficacy and safety of intratumoral thermotherapy using magnetic iron-oxide nanoparticles combined with external beam radiotherapy on patients with recurrent glioblastoma multiforme, *J Neurooncol*, 103 (2011) 317-324.
- [121] M. Johannsen, U. Gneueckow, B. Thiesen, K. Taymoorian, C.H. Cho, N. Waldofner, R. Scholz, A. Jordan, S.A. Loening, P. Wust, Thermotherapy of prostate cancer using magnetic nanoparticles: Feasibility, imaging, and three-dimensional temperature distribution, *Eur Urol*, 52 (2007) 1653-1662.
- [122] M. Johannsen, U. Gneveckow, L. Eckelt, A. Feussner, N. Waldofner, R. Scholz, S. Deger, P. Wust, S.A. Loening, A. Jordan, Clinical hyperthermia of

prostate cancer using magnetic nanoparticles: Presentation of a new interstitial technique, *Int J Hyperther*, 21 (2005) 637-647.

[123] A. Matsumine, K. Takegami, K. Asanuma, T. Matsubara, T. Nakamura, A. Uchida, A. Sudo, A novel hyperthermia treatment for bone metastases using magnetic materials, *International Journal of Clinical Oncology*, 16 (2011) 101-108.

[124] H. Yu, G.Y. Zhu, R.Z. Xu, H.Z. Niu, Q. Lu, G.Z. Li, Z.Y. Wang, D.S. Zhang, N. Gu, G.J. Teng, Arterial Embolization Hyperthermia Using As₂O₃ Nanoparticles in VX2 Carcinoma-Induced Liver Tumors, *Plos One*, 6 (2011).

[125] H. Matsuki, T. Yanada, T. Sato, K. Murakami, S. Minakawa, Temperature-Sensitive Amorphous Magnetic Flakes for Intratissue Hyperthermia, *Mat Sci Eng a-Struct*, 182 (1994) 1366-1368.

[126] W. Daocheng, W. Mingxi, Preparation of the core-shell structure adriamycin lipiodol microemulsions and their synergistic anti-tumor effects with diethyldithiocarbamate in vivo, *Biomed Pharmacother*, 64 (2010) 615-623.

[127] M. Mitsumori, M. Hiraoka, T. Shibata, Y. Okuno, Y. Nagata, Y. Nishimura, M. Abe, M. Hasegawa, H. Nagae, Y. Ebisawa, Targeted hyperthermia using dextran magnetite complex: A new treatment modality for liver tumors, *Hepato-Gastroenterol*, 43 (1996) 1431-1437.

[128] P. Moroz, S.K. Jones, J. Winter, B.N. Gray, Targeting liver tumors with hyperthermia: Ferromagnetic embolization in a rabbit liver tumor model, *J Surg Oncol*, 78 (2001) 22-29.

[129] J.A. Mosso, R.W. Rand, Ferromagnetic silicone vascular occlusion: a technic for selective infarction of tumors and organs, *Ann Surg*, 178 (1973) 663-668.

[130] K.N. Makovetskaya, N.B. Sirotinkin, M.I. Karelin, A.M. Granov, Composition for vascular embolization, Patent RU 2073529, 1995.

[131] A.M. Granov, M.I. Karelin, D.A. Granov, P.G. Tarazov, K.N. Makoveckaya, Method for parenchymal organs tumor treating, Patent RU 2065734, 1996.

[132] A.M. Granov, K.N. Makovetskaya, N.E. Kazantseva, M.I. Karelin, V. Suvorova Iu, D.A. Granov, Magnetic soft siloxane material for arterial embolization and hyperthermia of malignant tumors, *Vestn Rentgenol Radiol*, (2000) 35-40.

[133] J. Baumgartner, A. Dey, P.H.H. Bomans, C. Le Coadou, P. Fratzl, N.A.J.M. Sommerdijk, D. Faivre, Nucleation and growth of magnetite from solution, *Nat Mater*, 12 (2013) 310-314.

[134] F. Kunstlinger, F. Brunelle, P. Chaumont, D. Doyon, Vascular Occlusive Agents, *Am J Roentgenol*, 136 (1981) 151-156.

[135] C.A. Harper, Handbook of plastics, elastomers and composites, third edition ed., McGraw-Hill, New York, 1996.

[136] A.M. Granov, O.V. Muratov, V.F. Frolov, Problems in the local hyperthermia of inductively heated embolized tissues, *Theor Found Chem Eng*, 36 (2002) 63-66.

[137] Y.A. Yuzhelevskiy, Y.N. Zubkov, G.A. Asaturyan, N.N. Fedoseyeva, Z.S. Lebedeva, Formulation for vascular embolization, in, Patent SU 1106509, 1984.

[138] A.M. Granov, M.I. Karelin, D.A. Granov, P.G. Tarazov, K.N. Makoveckaia, Method for treating of tumors of parenchymal organs, in, Patent RU 2065734, 1996.

- [139] R.W. Rand, M. Snyder, D. Elliott, H. Snow, Selective radiofrequency heating of ferrosilicone occluded tissue: a preliminary report, *Bull Los Angeles Neurol Soc*, 41 (1976) 154-159.
- [140] M. Snyder, R.W. Rand, Utilization of barium-impregnated ferromagnetic silicone in vascular occlusion, *Bull Los Angeles Neurol Soc*, 40 (1975) 145-152.
- [141] K.N. Makoveckaia, N.B. Sirotkin, M.I. Karelin, A.M. Granov, Composition for vascular embolization, in, Patent RU 2073529, 1997.
- [142] H.R. Kricheldorf, *Silicon in Polymer Synthesis*, Springer-Verlag Berlin Heidelberg, New York, 1996.
- [143] Z.L. Wang, *Characterization of nanophase materials*, Wiley-VCH, Weinheim ; Chichester, 2000.
- [144] G. Cao, *Nanostructures & nanomaterials : synthesis, properties & applications*, Imperial College Press, London, 2004.
- [145] B.D. Cullity, S.R. Stock, *Elements of X-Ray Diffraction*, 3 edition ed., Prentice Hall, Boston, 2001.
- [146] G.K. Wertheim, *Mössbauer effect : principles and applications*, Academic Press, New York ; London, 1964.
- [147] R.E. Vandenberghe, C.A. Barrero, G.M. da Costa, E. Van San, E. De Grave, Mossbauer characterization of iron oxides and (oxy)hydroxides: the present state of the art, *Hyperfine Interact*, 126 (2000) 247-259.
- [148] G.F. Goya, T.S. Berquo, F.C. Fonseca, M.P. Morales, Static and dynamic magnetic properties of spherical magnetite nanoparticles, *J Appl Phys*, 94 (2003) 3520-3528.
- [149] M.F. Hansen, S. Morup, Estimation of blocking temperatures from ZFC/FC curves, *J Magn Magn Mater*, 203 (1999) 214-216.
- [150] S.P. Gubin, Y.A. Koksharov, G.B. Khomutov, G.Y. Yurkov, Magnetic nanoparticles: Preparation methods, structure and properties, *Usp Khim+*, 74 (2005) 539-574.
- [151] Y.W. Tan, Z.B. Zhuang, Q. Peng, Y.D. Li, Room-temperature soft magnetic iron oxide nanocrystals: Synthesis, characterization, and size-dependent magnetic properties, *Chem Mater*, 20 (2008) 5029-5034.
- [152] G.T. Rado, R.W. Wright, W.H. Emerson, Ferromagnetism at Very High Frequencies .3. 2 Mechanisms of Dispersion in a Ferrite, *Phys Rev*, 80 (1950) 273-280.
- [153] Agilent, 16454A Magnetic material test fixture: Operation and service manual, Agilent Technologies, 2001.
- [154] T. Tsutaoka, Frequency dispersion of complex permeability in Mn-Zn and Ni-Zn spinel ferrites and their composite materials, *J Appl Phys*, 93 (2003) 2789-2796.
- [155] G.M. Kavanagh, S.B. Ross-Murphy, Rheological characterisation of polymer gels, *Prog Polym Sci*, 23 (1998) 533-562.
- [156] J.T. Bushberg, *The essential physics of medical imaging*, 2nd ed., Lippincott Williams & Wilkins, Philadelphia ; London, 2002.

- [157] J.P. Jolivet, P. Belleville, E. Tronc, J. Livage, Influence of Fe(II) on the Formation of the Spinel Iron-Oxide in Alkaline-Medium, *Clay Clay Miner*, 40 (1992) 531-539.
- [158] R.L. Rebodos, P.J. Vikesland, Effects of Oxidation on the Magnetization of Nanoparticulate Magnetite, *Langmuir*, 26 (2010) 16745-16753.
- [159] J.S. Salazar, L. Perez, O. de Abril, T.P. Lai, D. Ihiwakrim, M. Vazquez, J.M. Greneche, S. Begin-Colin, G. Pourroy, Magnetic Iron Oxide Nanoparticles in 10-40 nm Range: Composition in Terms of Magnetite/Maghemite Ratio and Effect on the Magnetic Properties, *Chem Mater*, 23 (2011) 1379-1386.
- [160] T. Ahn, J.H. Kim, H.M. Yang, J.W. Lee, J.D. Kim, Formation Pathways of Magnetite Nanoparticles by Coprecipitation Method, *J Phys Chem C*, 116 (2012) 6069-6076.
- [161] J.P. Jolivet, S. Cassaignon, C. Chaneac, D. Chiche, E. Tronc, Design of oxide nanoparticles by aqueous chemistry, *J Sol-Gel Sci Techn*, 46 (2008) 299-305.
- [162] R.S. Tebble, D.J. Craik, *Magnetic materials*, Wiley-Interscience, London, 1969.
- [163] V.P. Shilov, J.C. Bacri, F. Gazeau, F. Gendron, R. Perzynski, Y.L. Raikher, Ferromagnetic resonance in ferrite nanoparticles with uniaxial surface anisotropy, *J Appl Phys*, 85 (1999) 6642-6647.
- [164] E. Tronc, P. Belleville, J.P. Jolivet, J. Livage, Transformation of ferric hydroxide into spinel by Fe (II) adsorption, *Langmuir*, 8 (1992) 313-319.
- [165] A.P.A. Faiyas, E.M. Vinod, J. Joseph, R. Ganesan, R.K. Pandey, Dependence of pH and surfactant effect in the synthesis of magnetite (Fe₃O₄) nanoparticles and its properties, *J Magn Magn Mater*, 322 (2010) 400-404.
- [166] Y. Yuan, D.A. Borca-Tasciuc, Anomalously High Specific Absorption Rate in Bioaffine Ligand-Coated Iron Oxide Nanoparticle Suspensions, *Ieee T Magn*, 49 (2013) 263-268.
- [167] J.L. Speier, Homogeneous Catalysis of Hydrosilylation by Transition Metals, *Advances in Organometallic Chemistry*, 17 (1979) 407-447.
- [168] L.N. Lewis, On the Mechanism of Metal Colloid Catalyzed Hydrosilylation - Proposed Explanations for Electronic Effects and Oxygen Cocatalysis, *J Am Chem Soc*, 112 (1990) 5998-6004.
- [169] L.N. Lewis, N. Lewis, Platinum-Catalyzed Hydrosilylation - Colloid Formation as the Essential Step, *J Am Chem Soc*, 108 (1986) 7228-7231.
- [170] A. Berenstein, Flow-Controlled Silicone Fluid Embolization, *Am J Roentgenol*, 134 (1980) 1213-1218.
- [171] G. Vallejo-Fernandez, O. Whear, A.G. Roca, S. Hussain, J. Timmis, V. Patel, K. O'Grady, Mechanisms of hyperthermia in magnetic nanoparticles, *J Phys D Appl Phys*, 46 (2013).